Review
doi.org/10.1002/elsa.202100187

Chemistry Europe
European Chemical Societies Publishing

Received: 19 October 2021
Accepted: 30 October 2021

Nanoarchitectured transition metal oxides and their composites for supercapacitors

Ankit Kumar[1,†] | **Hem Kanwar Rathore**[2,†] | **Debasish Sarkar**[2] | **Ashok Shukla**[1]

[1] Solid State and Structural Chemistry Unit, Indian Institute of Science, Bengaluru, India

[2] Department of Physics, Malaviya National Institute of Technology Jaipur, Rajasthan, India

Correspondence
Debasish Sarkar, Department of Physics, Malaviya National Institute of Technology Jaipur, Rajasthan 302017, India.
Email: debasish.phy@mnit.ac.in; deb.sarkar1985@gmail.com
Ashok Shukla, Solid State and Structural Chemistry Unit, Indian Institute of Science, Bengaluru 560012, India.
Email: akshukla2006@gmail.com

[†]Authors contributed equally to this work.

Funding information
UKRI Global Challenge Research Fund, Grant/Award Number: EP/P032591/1; Science and Engineering Research Board, Government of India, Grant/Award Number: SRG/2019/001211

Abstract

Supercapacitors have acquired a considerable scientific and technological position in the energy storage field owing to their compelling power capability, good energy density, excellent cycling stability, and ideal safety. The supercapacitor is the burgeoning candidate to cope with the ever-growing need for green and renewable energy. High-performance supercapacitors are realized by nanostructured electrode designs, which provide ameliorated surface area for abundant electrode-electrolyte interaction, ease of electron transfer and movement, and short ion-diffusion pathways that lead to increased performance. In this regard, transition metal oxide (TMO)-based electroactive materials are of significant interest owing to the remarkable combination of structural, mechanical, electrical, and electrochemical properties. Besides their high specific capacitance and energy density due to rich redox chemistry, highly reversible and fast charge-discharge processes, low cost due to abundance, and environment-friendliness make them the most promising materials for next-generation supercapacitors. But poor electrical conductivity and rate capability, inferior cycling life, and low power density are some of the major challenges that need to be addressed. Therefore, various nanostructures of pristine TMOs and their composites with other materials with complementary characteristics have been fabricated and investigated to realize supercapacitors with improved performance. This review summarizes all such reported pristine TMOs with different nanostructured dimensions namely, 3D, 2D, 1D, and 0D, and their composite structures for their application as electrode materials in supercapacitors. Design of different pristine and composite nanostructures, synthesis strategies, comprehensive structure-dependent electrochemical properties, present challenges, and future perspectives are reviewed.

KEYWORDS
composites, nanostructured electrode design, supercapacitor, transition metal oxides

Review
doi.org/10.1002/elsa.202100187

1 | INTRODUCTION

Energy is indispensable to build and maintain almost everything around us. But energy production and consumption contribute to two-thirds of the world's total greenhouse gas emissions. Exorbitant use of fossil fuels by mankind has rapidly depleted fossil fuel reserves in addition to aggravating atmospheric pollution which has done long-lasting, and possibly irreversible damage to our climate. It is thus crucial to address the challenge of climate change for the sustainable development of the society. At the same time, it is also equally important to ensure access to energy for economic development and enhance the quality of life, especially in under-developed parts of the world. To achieve these goals, the world is now shifting toward renewable energy resources, such as solar energy, wind energy, and so on. However, the challenge, in moving away from fossil fuels, is to economically harvest and store the energy generated from renewables. Unfortunately, renewable energy resources are intermittent in nature and also not fully exploitable at the time of production. So, there is an urgent need for efficient energy storage devices to use green energy for future usage. Currently, there are varieties of efficient energy storage devices available in the market, namely batteries, regular capacitors, electrochemical capacitors, fuel cells, hydrogen storage systems, and so on,[1] each having different storage mechanisms and diverse fields of applications. Figure 1 illustrates various electrochemical energy storage devices and their charge storage mechanisms. The simplest form of an energy storage device is a regular capacitor that consists of two parallel plates separated by a dielectric medium. The charge is stored between the plates as electric potential energy, and capacitance values lie in the microfarad range. By contrast, electrolytic capacitors in which dielectric is replaced by electronic/ionic conductive medium can deliver capacitance in the millifarad range with exceptionally high-power delivery capabilities (>10 kW/kg).[2,3] Batteries are another category of energy storage devices dominating consumer electronics because of their high energy density but severely lack in power delivery capability. This is due to the fact that the charge storage mechanism of batteries involves ion intercalation/deintercalation in the bulk of the active materials followed by electrochemical redox reactions. Hence, batteries can at best withstand thousands of cycles because of repeated volume alterations of electroactive materials during cycling. Other limitations with batteries involve phase transformations as well as dendrite growth and heat generation when operated at high rates, which leads to serious safety issues.[1,4] Electrochemical capacitors, also known as ultracapacitors or supercapacitors, bridge the gap between high-energy batteries and high-power capacitors. The charge storage mechanism of electrochemical capacitors is similar to conventional capacitors, but they can store thousands of farads in a single device. Supercapacitors can deliver 10^5 times more energy density and specific capacitance as compared to regular capacitors in addition to the high-power density in kW range arising due to the high surface area of electroactive materials, electrode-ion separation in nanoscale regime, and additional contribution from surface/near-surface based faradaic redox reactions.[1] Taking advantage of their high-power density, excellent cycling stability, good rate capability, reliability, and safety, supercapacitors have been exploited in various applications, including heavy-duty machineries, load-leveling systems for renewable energy sources, hybrid energy storage platforms for commercial vehicles, and storing energy in electric/hybrid vehicles through regenerative braking.[1,4,5] Accordingly, supercapacitors have garnered niche research interest because of their potential to complement or even replace batteries where high power delivery is required for a very short duration.

1.1 | Basics of electrochemical capacitors

Electrochemical capacitors, also known as supercapacitors consist of two electrodes, an electrolyte, a separator, and current collectors. Electrodes are the main component of supercapacitors, which are fabricated from nanosized materials to ensure high specific surface area and high porosity.[6] Furthermore, electrode materials should be thermally and chemically stable and should possess good electrical conductivity to achieve better rate performance for supercapacitors. The electrolyte plays a vital role in determining the operating potential window of a supercapacitor. Mainly three different classes of electrolytes are used extensively namely, aqueous, organic, and ionic liquids allowing varying potential windows. The current commercial supercapacitor market is dominated by organic electrolytes and ionic liquids because of their wide operating potential window in the range of 2.5–2.8 V and 3.5–4 V, respectively.[1] Separators, used to isolate electrodes electrically, should have high ionic conductance, high electric resistance, and reduced thickness to achieve better performance.[7] As the role of current collectors is to transfer the charge from the device to the external circuit with minimal resistance, they should be electrically highly conductive, corrosion-resistant, lightweight, and mechanically robust.[8] Depending on the charge storage mechanism and electrode materials used, supercapacitors can be classified in the following categories: (I) electric double-layer capacitors (EDLCs), (II) pseudocapacitors, and (III) symmetric/asymmetric supercapacitors.[1,3,5]

Review
doi.org/10.1002/elsa.202100187
Chemistry Europe
European Chemical Societies Publishing

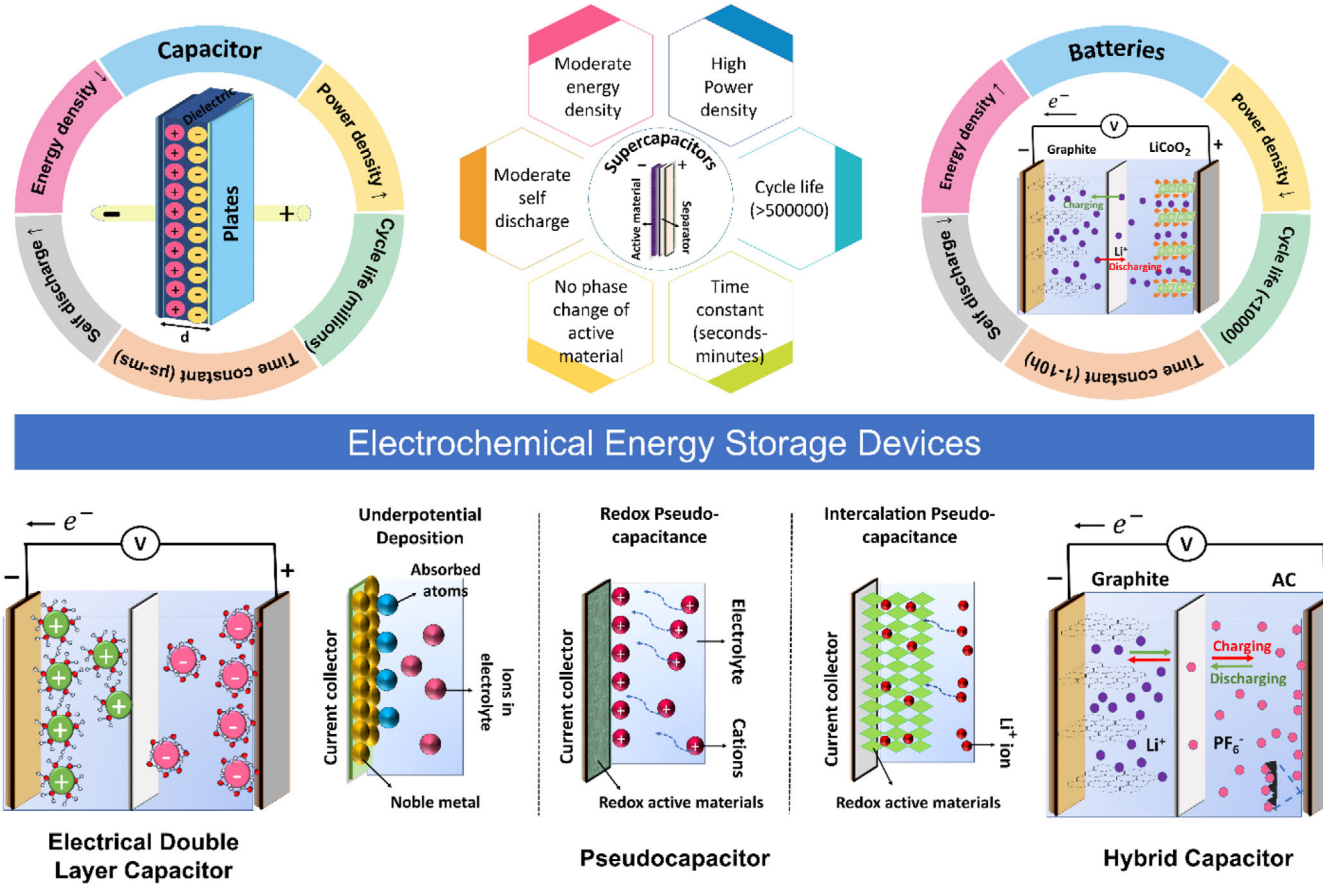

FIGURE 1 Classification of electrochemical energy storage devices and conceptual representation of their charge storage mechanisms

1.1.1 | Electric double-layer capacitors (EDLCs)

The charge storage mechanism in EDLCs is electrostatic in nature which involves reversible adsorption of electrolyte ions on the electrode surface, as shown in Figure 1. Spontaneous charge separation occurs when an electronically conductive electrode is dipped in an electrolyte and subjected to the polarization of the electrode-electrolyte interface. This results in the formation of Helmholtz double layer on the electrode surface. Therefore, the electrode-electrolyte interface can be thought of as a capacitor, whose capacitance can be calculated using the following equation:

$$C = \frac{\epsilon_0 \epsilon_r}{d} A \quad (1)$$

where, ϵ_0 is the permittivity of vacuum, ϵ_r is the dielectric constant of the electrolyte, A is the surface area of the electrode, and d is the thickness of the double layer. EDLCs are characterized by rectangular-shaped cyclic voltammetry (CV) curves along with triangular-shaped galvanostatic charge/discharge (GCD) profiles.

Due to the absence of any surface redox reactions, charge separation at electrode–electrolyte interface is instantaneous, which leads to high power performance, and for the same reason, EDLCs can withstand millions of cycles without any significant fading in device performance.[1,3,5] Although EDLCs are simple in design and most popular among supercapacitors, they severely suffer from poor capacitance and hence energy density.[5] Therefore, current research is directed on enhancing the energy density of EDLCs to ensure their widespread applications.

1.1.2 | Pseudocapacitors

To address the challenge of the limited energy density of EDLCs, efforts have been focused on designing pseudocapacitive materials, which involve fast redox reactions at the surface and/or near-surface regions of the electrode material. This mechanism allows change in the valence state of electroactive elements due to electron transfer at the electrode-electrolyte interface.[1] Additional pseudocapacitance, other than double-layer capacitance, is the reason for enhanced energy density with these materials.

doi.org/10.1002/elsa.202100187

Pseudocapacitive charge storage mechanism is different from batteries that involve faradaic redox reactions in the bulk of the electrode material. Another key feature of the pseudocapacitive charge storage mechanism is that there is no phase transformation of electrode material due to polarization that is reflected by the absence of sharp and well-defined redox peaks in the CV curve unlike batteries where sharp redox peaks appear due to the diffusion-controlled charge storage processes.[4] Here, the term "pseudo" reflects a different kind of charge storage mechanism whose electrochemical characteristics are similar to EDLCs. Different pseudocapacitive charge storage mechanisms involve (1) underpotential deposition, (II) redox pseudocapacitance, (III) intercalation pseudocapacitance, and (IV) doping pseudocapacitance.[3] Underpotential deposition involves the adsorption of metal ions or hydrogen atoms at the surface of noble metals, like Pt, Ru, Rh, and Ir, well above their reversible redox potentials (e.g., H^+ or Pd^{2+} on Pt or Au). This mechanism can be represented by the following equation.

$$M + yA^{z+} + yze^- \leftrightarrow MA \tag{2}$$

where M and A are noble metal and adsorbed atoms, respectively; y and z are the numbers of adsorbed atoms and the valence state of the adsorbed ion, respectively. So, yz represents the number of electrons transferred during the reaction.[1] In the redox pseudocapacitance, cations are electrochemically adsorbed on the surface of oxidized species followed by the fast and reversible faradaic charge transfer reactions across the electrode/electrolyte interface. This mechanism is demonstrated by the following equation:

$$Ox + yC^+ + ye^- \leftrightarrow RedC_z \tag{3}$$

where C^+ is the electrolytic cation adsorbed on the surface (like H^+, K^+, Na^+, etc.) and y is the number of electrons transferred.[1] Doping pseudocapacitance occurs due to the reversible doping and de-doping in the conductive polymers.[3] Intercalation pseudocapacitance involves insertion/extraction of electrolytic ions into the layered host materials, accompanied by a change in the valence state of the electroactive material to ensure charge neutrality, as illustrated in Equation (4).

$$MA_x + yLi^+ + ye^- \leftrightarrow Li_yMA_x \tag{4}$$

where MA_x is the layered host material and y is the number of electrons transferred during the reaction.[1] Interestingly, the electrochemical performance of intercalation pseudocapacitance lies between supercapacitors and batteries, having capacitive electrochemical characteristics such as reduced charging time, fast transportation of ions, good rate capability, and superior cycling stability.[1] In summary, the total charge stored by different charge storage mechanisms can be segregated into three parts: (I) faradaic contribution from the diffusion-controlled ion intercalation process, (II) faradaic contribution arising from pseudocapacitive charge transfer reactions at the surface/near-surface regions of the electrode material, and (III) non-faradaic capacitive contribution due to the adsorption of ions at electrode/electrolyte interface. To segregate contributions from these capacitive and diffusive processes in an electrode material, the following relation between current obtained in CV analysis and scan rate can be used:

$$i = av^b \tag{5}$$

where v is the scan rate, a and b are adjustable parameters. The value of b indicates the type of charge storage mechanism. Linear response of current with scan rate ($b = 1$) indicates the capacitive behavior, whereas $b = 1/2$ represents diffusion-controlled charge storage mechanism satisfying Cotrell's equation $i = av^{1/2}$.[1,3,9]

Therefore, the total current obtained in a CV can be written as a sum of the capacitive current ($a_1 v$) and diffusion controlled faradaic current ($a_2 v^{\frac{1}{2}}$) as per the following equation:

$$i\,(V) = a_1\, v + a_2 v^{\frac{1}{2}} \tag{6}$$

$$\text{or, } i\,(V) \,/\, v^{\frac{1}{2}} = a_1\, v^{\frac{1}{2}} + a_2 \tag{7}$$

Now, the value of current at a given potential and at different scan rates are obtained from the CV data. Therefore, the parameters a_1 and a_2 can be obtained from the intercept and slope of the straight-line plot of $i(V)$ and $v^{\frac{1}{2}}$, which can be further used to distinguish the capacitive and diffusive contributions quantitatively. Researchers have concentrated more on pseudocapacitive materials because of their high energy density in comparison to EDLCs but the former lack in power performance and cycling stability.

1.1.3 | Symmetric/Asymmetric supercapacitors

Symmetric capacitors are those in which both the positive and negative electrodes are made of the same material. It is just a parallel combination of two similar electrodes in which the overall potential of the cell is limited by

the operating potential of the individual electrode, and hence limited energy-power densities. Asymmetric supercapacitors were developed to achieve high energy density in supercapacitors and consist of electrodes made of different materials. Device configurations of asymmetric supercapacitors are wide, mainly classified as capacitive asymmetric and hybrid asymmetric supercapacitors. Capacitive asymmetric involves a broad range of electrode combinations including, two EDLC electrodes of different materials, two pseudocapacitive electrodes of different materials, and EDLC type electrode combined with a pseudocapacitive electrode. The latter one can also be termed as a hybrid capacitor in which one electrode stores charge through purely capacitive processes while the pseudocapacitive electrode stores charge through faradaic processes.[1,3]

Here, the important parameter for evaluating the performance of a supercapacitor is the energy density, which can be calculated using the following formula:

$$E = \frac{1}{2} CV^2 \quad (8)$$

where C is the capacitance and V is the operating potential window of the cell. Therefore, a twofold increase in the potential window could lead to a fourfold increase in the energy density. Thus, enhancing the operating potential window plays a vital role in improving the energy density and hence the overall performance of the supercapacitor. Asymmetric supercapacitors, by taking the advantage of operating potential windows of two different electrode materials, can lead to the maximum potential of the full device.[1] Hence, designing asymmetric supercapacitors with suitable electrode materials could result in a high energy density without sacrificing high power density and cycling stability traits.

1.2 | Materials for supercapacitors

The key to improving the performance of supercapacitors is in designing new electrode materials for asymmetric supercapacitors. Generally, electrode materials for supercapacitors are classified into high surface area active materials that store charge in both electrostatic and pseudocapacitive modes.[5,6] The key requirements of electrode materials that store charge electrostatically through the formation of double-layer are high specific surface area, high electronic conductivity, porosity, and electrochemical stability. Carbon-based materials like activated carbon,[10–12] carbon nanotubes,[13,14] graphene,[15–17] carbon onions,[18–20] and so on, satisfy all the above-said requirements. These materials have widely distributed pore sizes that can be classified into three different categories, namely micropores (pore size <2 nm), mesopores (2–50 nm), and macropores (pore size >50 nm).[5] To find the optimum pore size for achieving the highest capacitance for double-layer capacitors, Largeot et al. studied the behavior of carbide-derived carbons in an ionic liquid electrolyte.[21] They concluded that the most efficient adsorption of ions and hence, the highest double layer capacitance is obtained when ion size is close to pore size as smaller or larger pore size than ion size leads to decreased capacitance.[21] Generally, specific capacitance obtained from EDLCs is limited to 100–250 F/g and the supercapacitor devices based on carbon materials can achieve an energy density in between 3 and 10 Wh/kg.[1] Pseudocapacitive materials, on the other hand, involve additional surface redox reactions that lead to 10–100 times more capacitance than carbon-based materials making pseudocapacitive materials more attractive for supercapacitors.[1,4] Conducting polymers and transition metal compounds are an important class of pseudocapacitive materials that have been explored widely as supercapacitor electrodes.[22,23] Conductive polymers, like polypyrrole and polyaniline, have been widely studied for supercapacitor applications due to their good charge storage capacity, intrinsic elasticity for flexible electronic devices, a wide potential window between −1 to +1 V, easy synthesis approach, and low cost.[24,25] However, conducting polymers undergo swelling as well as shrinking during the insertion/extraction process, which degrades the mechanical stability of the electrodes and hence deteriorates the cycling stability of supercapacitors.[24] Apart from conducting polymers, various transition metal compounds have been investigated for supercapacitor applications with better electrochemical stability than polymer-based materials and improved capacitance than carbon-based materials. RuO_2 was the first discovered pseudocapacitive material that exhibited a wide potential window of 0–1.2 V and a specific capacitance of 1450 F/g. Irrespective of its high proton conductivity and cycling stability,[23] scarcity, toxicity, and the high cost of ruthenium have limited its widespread commercial applications.[3] To cope with this issue, the quest for alternative low-cost transition metal compounds with enhanced performance has been intensified. Further, researchers focused on earth-abundant transition metal elements that exhibited multivalent states. These transition metal elements are coordinated with various elements including O, S, Se, and functional groups of OH to form a series of oxides, sulfides, selenides, and hydroxides.[26] The transition metal sulfides and selenides are promising materials for the supercapacitors due to their inherent high electrical conductivity, but practical capacitance and energy density are still low. Also, the transition metal hydroxides exhibit high theoretical specific capacitance, but low specific capacitance

is hindering their widespread application.[26] The process of preparation, control of morphology and structure, cost, and performance are some of the important parameters that need to be considered before widespread commercial exploitation.

2 | MOTIVATION FOR TMOs AS SUPERCAPACITIVE ELECTRODES

Transition metal oxides (TMOs) are an important class of pseudocapacitive electrode materials for supercapacitors in which transition metals (group IV to VII B elements) are bound to oxygen atoms. The major attraction of TMOs is their variable oxidation states due to the incomplete *d* sub-shell that allows them to show a remarkable combination of structural, electrical, electrochemical, and mechanical properties. Electronic properties of TMOs depend on the type of transition metal and the formation of oxide compounds. By scaling down TMOs to the nanoscale, outstanding properties can be achieved that is not possible with their bulk counterparts. Nanoscale morphology increases surface area, and high surface-to-volume ratio promotes efficient utilization of TMOs as electrode materials in energy storage systems. High specific capacitance, improved energy density, reversible and fast charge-discharge process, low cost, and environment-friendliness make them attractive materials for supercapacitors. However, poor electrical conductivity, inferior cycling capability, low surface area, and power density are the major challenges that need to be addressed.[27] In short, the basic characteristics that transition metal oxide should have to be used as supercapacitor electrodes are: (1) high electronic conductivity, (2) two or more oxidation states which can coexist over a range of potential window without phase change, and (3) fast intercalation/deintercalation of protons or other cations within three-dimensional lattice during redox process.[28]

In 1971, RuO_2 was the first discovered pseudocapacitive material,[29] which was thoroughly explored by researchers owing to the wide potential window of 1.2 V, variable oxidation states, and reversible redox reactions. Other characteristics of RuO_2 include high proton conductivity, good thermal stability, and a high specific capacitance ranging between 1400–2000 F/g.[30–34] Crystalline RuO_2 is a metallic conductor that has a low capacitance value as compared to amorphous RuO_2[35] as protons diffuse to a larger extent in the amorphous phase in relation to the crystalline phase.[36] Pristine RuO_2 has poor chemical stability in acidic medium and shows a tendency to self-aggregate. Electrochemical studies of RuO_2 single-crystal in sulfuric acid reveal that crystal faces (101) and (110) are less reversible as compared to (002) face.[37,38]

Charge storage in RuO_2 involves surface-based redox reactions where the non-faradaic contribution is lower than the faradaic contribution. Pseudocapacitive behavior of RuO_2 depends on the reaction environments, which in turn show varying sensitivities toward crystallinity in acidic and basic mediums. Charge storage mechanism in the acidic electrolyte can be illustrated through Equation (9), where rapid and reversible electron transfer is accompanied by electro-adsorption of protons (H^+ ions) on the surface of RuO_2 particles that leads to a change in oxidation state of Ru to Ru(II) and Ru(II) to Ru(IV).[28]

$$RuO_2 + xH^+ + xe^- \leftrightarrow RuO_{2-x}(OH)_x \quad (9)$$

It has been found that in anhydrous RuO_2, cation has low ionic conductivity as compared to $RuO_2.xH_2O$ because H^+/cation can diffuse between H_2O and OH^- sites.[39] It is reported that $RuO_2.0.5H_2O$ has a capacitance of 900 F/g and $RuO_2.0.03H_2O$ shows a capacitance of 29 F/g, whereas, RuO_2 shows a capacitance of 0.5 F/g.[40] The pseudocapacitive property of RuO_2 is affected by various factors such as particle dimension, morphology, porosity, and surface area. The surface area of active materials plays an important role in the amount of charge stored because the better surface area leads to more active sites available for redox reactions. An efficient way of increasing the surface area is making nanosized RuO_2, by generating pores large enough to accommodate electrolyte ions easily during charge and discharge. Thus, the maximum utilization of active materials in small-sized particles leads to high capacitance values.[41,42] The discovery of RuO_2 led to the exploration of other TMOs as pseudocapacitive electrode materials. TMOs can be divided into two categories: (I) noble metal oxides and (II) base metal oxides. Noble metal oxides such as RuO_2, IrO_2, and so on exhibit good electrochemical performance but their major shortcoming is extremely high cost. Low cost and environment-friendly base metal oxides like MnO_2, NiO, Fe_3O_4, and so on with reasonable electrochemical performance are thus alternatives to noble metal oxides.[43] However, RuO_2 is often blended with less expensive transition metal oxides to realize synergistic pseudocapacitive effects from the two components with superior electrochemical performance. Also, various activated porous nano-carbons have been intimately blended with different TMOs to form nanocomposites that exhibited improved conductivity and charge storage efficiencies.[44–51] As discussed earlier, porous nano-carbons are chemically stable, inexpensive with good EDLC features along with a good capability of maintaining high discharge rates. But to supplement their small intrinsic capacitance, they must be blended with highly pseudocapacitive TMOs for achieving better electrochemical efficiency. Motivation for using TMOs

doi.org/10.1002/elsa.202100187

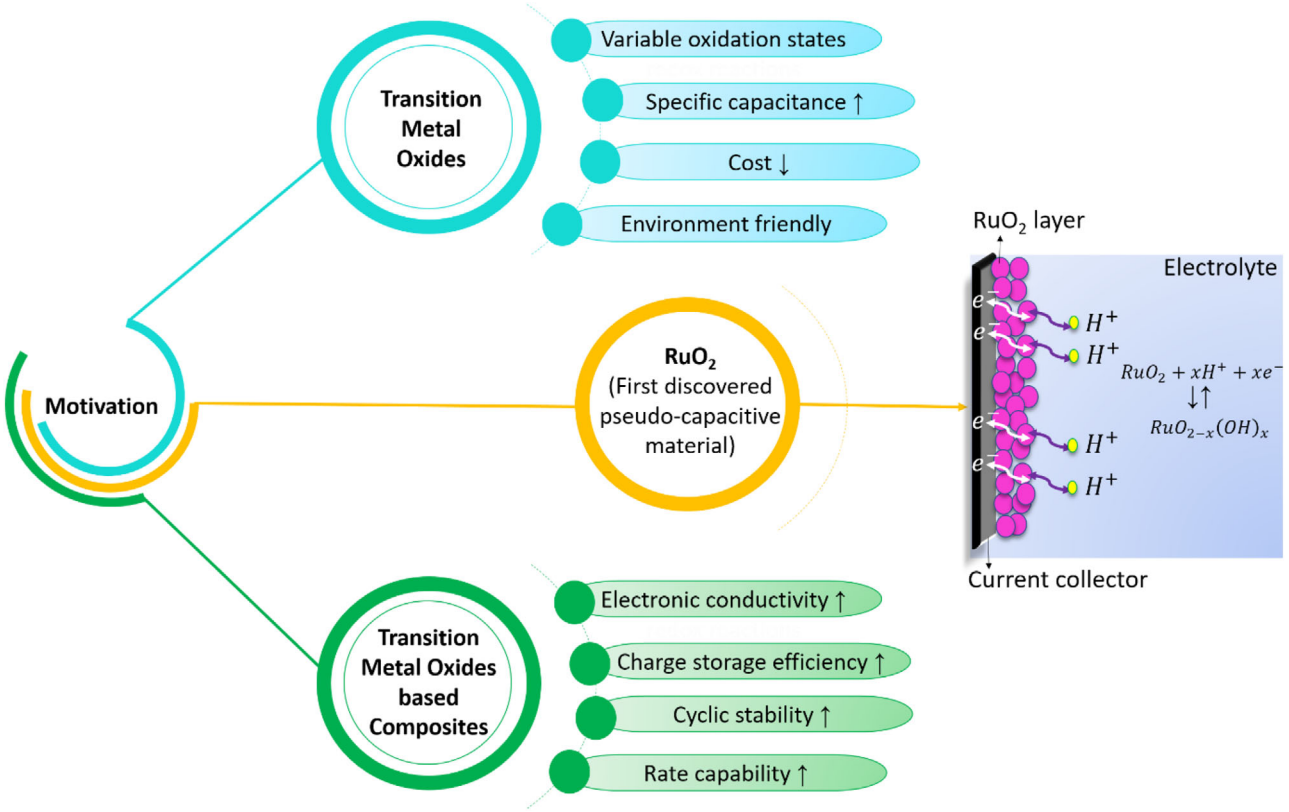

FIGURE 2 Advantages of TMOs and their composites for supercapacitors

and their composites as supercapacitive electrodes is summarized in Figure 2. To date, researchers have studied various nanostructured morphologies of TMOs including RuO_2, MnO_2, Co_3O_4, Mn_3O_4, Fe_2O_3, Fe_3O_4, V_2O_5, NiO, and so on,[52–55] and also their composites for supercapacitor applications with widely varying electrochemical performance. In the following sections, we summarize different synthesis methods, characteristics, charge storage mechanisms, and properties of various nanostructured TMOs and their composites as pseudocapacitive electrode materials.

3 | SYNTHESIS OF PRISTINE TMOs AND THEIR COMPOSITES

The structure and morphology of electrode materials play a significant role in enhancing the performance of energy storage devices. Thus, it is seminal to design and fabricate optimized nanostructured materials that are desirable for high-performance supercapacitors. Various nanostructures of different dimensions as well as nanostructured composites have been synthesized by researchers via several routes including hydrothermal method, solvothermal method, chemical bath deposition, electrodeposition, and so on. The overview of such synthesis methods for TMOs and their composites is depicted in Figure 3 and described in this section.

3.1 | Hydrothermal method

The hydrothermal method is used to synthesize TMO-based materials in an aqueous system at temperature and pressure above ambient. The aqueous solution of precursors is placed in a closed Teflon-lined stainless-steel (SS) autoclave which is usually heated around 100°C. Accordingly, the pressure within the autoclave increases dramatically. This one-step process to synthesize crystalline material is possible due to the synergistic effect of high temperature and high pressure.[56] The structure and morphology of materials can be altered by changing the precursors, their ratios, and heating temperature. This method is popular owing to its advantages such as ease in manipulating morphology and changing particles size, simplicity, environment friendliness, low cost, and the possibility of scaling up for large-scale production.[57] Various nanostructured morphologies of TMOs such as MnO_2,[58] Fe_2O_3,[59] NiO,[60] Co_3O_4,[61] $CuCo_2O_4$,[62] and so on, have been synthesized by the hydrothermal

doi.org/10.1002/elsa.202100187

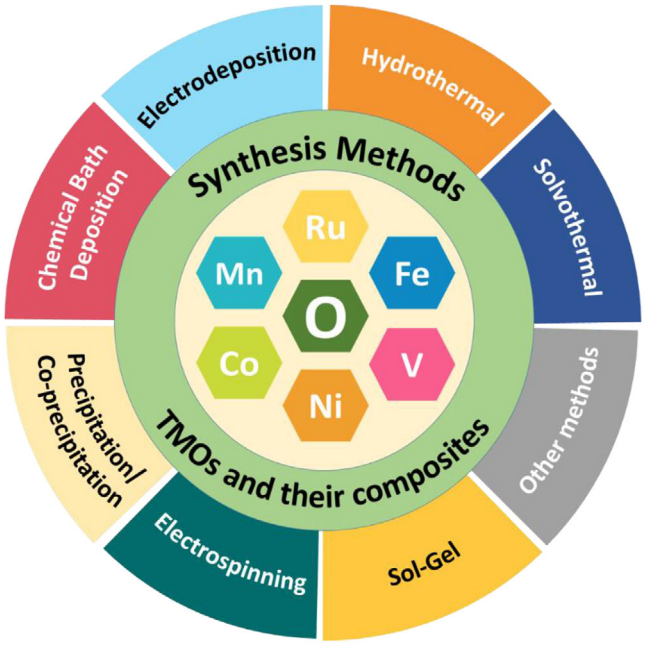

FIGURE 3 Summary of various methods used for synthesizing TMOs and their composites for supercapacitors

method. For instance, Paravannoor et al. synthesized NiO nanowires using this method.[60] First, the 0.7 M aqueous solution of nickel chloride and ammonium oxalate were mixed followed by the addition of triethanol amine. The solution was transferred to Teflon lined autoclave and placed at 120°C temperature for 10 h. The green-colored precipitate was washed thoroughly and annealed at 300°C for 1 h to obtain NiO nanowires. Recently, α-MnO_2 nanorods were prepared by Jayachandran et al. using the hydrothermal method.[63] In brief, $KMnO_4$ was dissolved in DI water and stirred for 30 min at 50°C. SiO_2 dissolved in HNO_3 was added dropwise to the solution with continuous stirring. The obtained purple-colored solution was transferred to Teflon lined autoclave and placed in an oven at 160°C for 12 h. The product was centrifuged and dried in a hot air oven at 120°C for 8 h to get α-MnO_2 nanorods. Wang et al. prepared NiO/ZnO electrodes using a soft template and hydrothermal route.[64] First, ordered mesoporous ZnO was prepared by soft template route, followed by hydrothermal treatment for the synthesis of composite. The precursors, namely $C_7H_5NaO_6S.2H_2O$ and $NiCl_2.6H_2O$, and ordered mesoporous ZnO were taken in desired amounts and dissolved in DI water, followed by ultrasonication for 30 min and continuous stirring for 12 h. The suspension was transferred to Teflon lined autoclave that was placed in an air oven at 180°C for 12 h. The obtained green-colored product was centrifuged and dried, followed by annealing at 500°C for 4 h to obtain the desired grey-colored composite.

3.2 | Solvothermal method

The solvothermal method is similar to the hydrothermal method, but instead of an aqueous solution, a non-aqueous solution is used. In comparison to the aqueous medium, organic solvents are explored as reaction mediums in a broad range of temperatures, which averts agglomeration, regulates morphology, and phase structure of the reaction products. Morphological variations in the nanostructured materials shorten ion diffusion lengths, which promote facile movements of electrolyte ions and electrons and hence, enhance the electrochemical performance.[57] Solvents may form several complexes with the ions which in turn affects the nucleation and growth mechanism and leads to the formation of different nanostructured TMOs.[56] A series of oxides including NiO,[65] CoO,[66] $MnFe_2O_4$,[67] and so on, with different structures such as nanoflakes, nanorods, quantum dots, etc., have been prepared via this method. As an example, Su et al. prepared $MnFe_2O_4$ QDs/N-doped graphene composite material via a solvothermal synthesis route.[67] In detail, GO suspension was obtained by dispersing GO powder in DMF, followed by sonication for 6h. $Mn_2(CO)_{10}$ and $Fe(CO)_5$ were dispersed in DMF separately under sonication. Subsequently, the two solutions were mixed together followed by dripping of octylamine. This mixture was added to GO suspension and sonicated for some time. Finally, the suspension was transferred to Teflon-lined SS autoclave and heated at 170°C for 2 h. The product was then washed, freeze-dried, and annealed at 400°C for 2 h in Ar atmosphere to remove residual octylamine and obtain the $MnFe_2O_4$ QDs/N-doped graphene composite. Likewise, Wang et al. fabricated 3D CoO QDs/Graphene hydrogels using the solvothermal method.[66] The CoO_x QDs were prepared by single-step oil bath-assisted heat treatment method. The CoO_x QDs were dispersed in GO suspension with continuous stirring for 30 min, followed by centrifugation to remove free QDs. Finally, the precipitate was dispersed again in ethanol and transferred to a Teflon-lined autoclave that was placed at 180°C for 12 h to form CoO/GS hydrogel. Sethi et al. also synthesized NiO nanoflakes using the solvothermal method using $NiCl_2$, $6H_2O$, and NaOH as precursors in a mixed solvent of ethylene glycol and water (1:1).[65]

3.3 | Electrodeposition method

Electrodeposition technique is used to deposit a metallic coating on the substrate by cathodic reduction reaction from an aqueous or organic precursor solution. It is broadly used for the preparation of TMOs-based nanostructured electrode materials for uniform deposition over

varied substrates.[57] It is usually carried out at room temperature, which favors the fabrication of nanostructure electrodes with precise control over film thickness. Film thickness can be controlled by tuning the deposition time and current, and the morphology, as well as the structure, are controlled by varying the precursor solution. Low cost and easy synthesis method using simple apparatus, excellent quality of the product, and the possibility of deposition over a large electrode area make the electrodeposition method promising for fabricating electrode materials for supercapacitors.[56] Various TMO materials including α-Fe_2O_3,[68] MnO_2,[69] NiO,[70] $NiCo_2O_4$,[71] and so on, have been fabricated by this technique. For instance, Yang et al. deposited porous MnO_2 on Ni foam using CV electrodeposition.[69] The electrodeposition was performed by a three-electrode system with Ni foam as working electrode, Pt wire as a counter electrode, and saturated calomel electrode (SCE) as a reference electrode in an electrolyte containing 0.1 M $Mn(CH_3COO)_2$ and 0.1 M Na_2SO_4 maintained at pH 7. For the deposition, CV was performed within the potential range 0.5–1.2 V (vs. SCE) at a scan rate of 200 mV/s. The deposition time was varied to obtain electrodes with varying mass loadings. Finally, the electrodes were washed with DI water and ethanol, dried at room temperature, and annealed at 200°C for 2 h to get the desired material. Also, Yin et al. synthesized $NiCo_2O_4$ nanosheets (NSs)@HfC nanowires.[72] First, HfC nanowires were grown on carbon fiber by catalyst-assisted low-pressure CVD technique. The HfC nanowire coated carbon fiber was taken as a working electrode for the electrodeposition of $NiCo_2O_4$ NSs from a solution containing 0.5 mM $Ni(NO_3)_2$ and 1 mM $Co(NO_3)_2$ using CV technique performed for 20 Cycles at 20 mV/s within −1.1 to −0.5 V potential window. The sample was then heated at 350°C for 3 h to achieve the desired product. Singh et al. fabricated Ni/NiO core-shell nanowires by electrodepositing Ni nanowires within the pores of AAO template followed by template removal to get freestanding Ni nanowires, and then controlled oxidation of nanowires in air to get the core-shell structure.[70] Recently, Wang et al. fabricated Fe_2O_3 NTs@PPy/CC using a sacrificial template and electrodeposition route.[73]

3.4 | Chemical bath deposition method

Chemical bath deposition (CBD) process involves a direct reaction between the precursors in the solution that results in the formation of products. To synthesize nanocrystalline structures with controlled morphologies, reaction rate should be slow that favors gradual diffusion of ions over substrates to form thin films of desired morphologies. On the contrary, fast reaction rates lead to the formation of large particles and precipitations. Thin films of TMOs have been efficiently fabricated by this method. Non-requirement of any intricate instrument, the possibility of deposition over a large area, good control over the crystallites size in the film, low-temperature method, and low-cost make this technique promising for the synthesis of TMOs. Patil et al. obtained 3D nanospheres of β-MnO_2 on SS substrate using this method.[74] They used $KMnO_4$ as a precursor and dissolved it in distilled water to obtain a matrix solution, followed by the addition of methanol which acts as a reducing agent. The solution was transferred to a beaker containing SS substrate and left for 12 h at room temperature. β-MnO_2 deposited on SS substrate was taken out, washed, and dried at room temperature. Similarly, Tian et al. have grown 3D MnO_2 film on nickel foam using CBD method,[75] in which nickel foam substrate was dipped vertically in an aqueous solution of 0.04 M $MnCl_2$ and 4 M $NaBrO_3$ and kept at 60°C for 12 h. After the growth, an electrode was washed with DI water and dried. Likewise, Sarkar et al. deposited NiO nanoflakes on SS substrate,[76] and Tian and co-workers prepared 3D hierarchical Co_3O_4 thin films on nickel foam substrate using the CBD method.[77]

3.5 | Sol-gel method

Sol-gel method involves the formation of sols (solid particles dispersed in liquid) and then connecting the sol particles to form a network (gel) through hydrolysis and condensation reactions.[78] The condensation reactions are affected by various parameters including precursors, ratio of alkoxide and water, pH, temperature, solvent, and catalyst used. The advantages of using this method are low temperature and cost-effectivity, the possibility of coating on larger substrates due to liquid phase deposition, and versatility in controlling morphology. This method is also used for the preparation of TMOs. For instance, Ray et al. synthesized porous spinel structured $NiMn_2O_4$ via the sol-gel method.[79] In brief, the precursors were taken in desired amounts and dissolved in ethylene glycol. Subsequently, PVP was added and the mixture was stirred to get a transparent solution, which was then heated in a hot oil bath under magnetic stirring. The precipitate was washed copiously, dried and the resultant material was annealed in an air atmosphere to get $NiMn_2O_4$ nanoparticles. Likewise, Maitra et al. synthesized $MgCr_2O_4$ nanoparticles using the sol-gel method.[80] First, MgO was dissolved in HNO_3, and $Cr(NO_3)_3.9H_2O$ was added to DI water under continuous stirring till a greenish color solution appeared. This was followed by mixing two solutions and dropwise addition of Triethanolamine (chelating agent) and overnight stirring at 150°C. A gel-like substance was formed that was dried, grounded in pestle and mortar, and calcined at 600°C for 5 h to obtain the desired material.

Also, Bhagwan et al. have prepared $CoMn_2O_4$ nanofibers via sol-gel route and obtained a nanofabric morphology by using tissue paper pieces as a template.[81]

3.6 | Chemical precipitation/co-precipitation method

In the precipitation/co-precipitation process, nucleation, growth, coarsening, and agglomeration processes occur simultaneously, and the products are formed as a result of high supersaturation condition. The key step is nucleation that leads to the formation of small particles, and the second step, namely Ostwald ripening, affects the morphology, size, and properties. It is a simple, rapid, low-temperature, and energy efficient process, but the traces of impurities get precipitated along with the product.[82] Recently, Zhang et al. synthesized MnO_2 and oxygen-deficient MnO_2 by precipitation method using $Mn(NO_3)_2$ as a precursor.[83] The aqueous solution was maintained at pH 9 by adding aqueous NaOH solution followed by the addition of hydrogen peroxide. The solution was ultrasonicated for 1 h. The resulting precipitate was copiously washed with DI water and ethanol, and dried. A similar procedure was followed for the synthesis of oxygen-deficient MnO_2, except the addition of sodium citrate dihydrate before adding NaOH and H_2O_2. Likewise, Elanthamilan et al. used the chemical co-precipitation method for the fabrication of $CoFe_2O_4$ decorated on activated carbon (AC) derived from pistachio shell.[84] They used an aqueous solution of $CoCl_2.6H_2O$ and FAS solution for the synthesis of $CoFe_2O_4$ nanoparticles. These solutions were mixed with CTAB with continuous stirring and subsequent sonication. Dropwise addition of NaOH with constant stirring at 90°C results in precipitation, which was collected, washed, and dried. For the synthesis of $CoFe_2O_4$@AC composite, same procedure was followed except the addition of AC in the solution before adding NaOH. Also, Huang et al. have grown Mn_3O_4 nanoflakes on rGO using a chemical precipitation method.[85] The solution of precursors $MnSO_4.H_2O$ and $KMnO_4$ were dripped in an aqueous suspension of GO by a peristaltic pump and the suspension was sonicated for 20 min. The products were collected, washed, and freeze-dried. The obtained powder was annealed in Ar/H_2 atmosphere for 2 h at 250°C to obtain Mn_3O_4/rGO composite.

3.7 | Electrospinning method

In this technique, the spinning force and electric field are used to eject the liquid precursors for the formation of fibrous nanostructures. This method is useful for the preparation of nanowires or nanotubes of different inorganic nanomaterials irrespective of their crystal orientation.[82] The diameter and length of the nanofibers depend on the liquid flow rate and applied voltage. Thus, it is a promising method to obtain nanofibers or nanotubes of TMOs without any restriction on the crystal growth orientation of different materials.[82] Recently, Lu et al. prepared a composite using 3D hierarchical Co_3O_4 derived from MOF distributed on electrospun derived polyacrylonitrile nanofiber.[86] First, the ZIF-67 nanocubes were prepared and added to DMF. This was followed by ultrasonication for 1 h and stirring at room temperature for 2 h. PAN was added to the solution with a mass ratio 1:1 followed by constant stirring of 24 h. Subsequently, the solution was filled in a syringe with a needle and it was driven by a syringe pump. The obtained PAN/ZIF-67 nanofibers were dried at room temperature under vacuum and calcined in air for 2 h to get the desired material.

3.8 | Other methods

Besides the above-mentioned synthesis routes, pulsed laser ablation,[87] microwave irradiation,[88] successive ionic layer adsorption and reaction (SILAR),[89] combustion driven synthesis route,[90] carbon micro electromechanical systems in fabricating 3D microelectrode array (C-MEMS),[91] and so on, have been explored by the researchers to fabricate TMOs and their composites. The structure and morphology of the products can be altered by varying different parameters associated with these synthesis methods to obtain the optimized electrode materials essential for realizing high-performance electrochemical energy storage devices.

4 | APPLICATION OF TMOs AND THEIR COMPOSITES IN SUPERCAPACITORS

As discussed earlier, the variable oxidation state of TMOs allows multiple electron transfer that leads to prolonged discharge profile through fast faradaic redox reactions and enhanced energy density, which makes them the most promising electrode materials for supercapacitors. However, poor electronic conductivity, poor rate capability, and inferior cycling capability are some of the issues that need to be considered and overcome. To resolve these challenges various attempts have been made by the researchers by fabricating nanostructures of different dimensions and forming composites of TMOs with other materials having complementary traits for comprehensively enhancing their electrochemical performance. To date, a series of TMOs of different dimensions as well as their composites have

Review
doi.org/10.1002/elsa.202100187
Chemistry Europe
European Chemical Societies Publishing

been synthesized and explored widely for supercapacitor applications. Recent advances in 3D, 2D, 1D, and 0D TMOs and their composites for supercapacitor applications are summarized in the following sections. Also, advantageous properties associated with the electrode structures of different dimensions and the impact of dimension on the performance of supercapacitor electrodes are described.

4.1 | 3D TMO-based nanostructures for supercapacitors

It is known that the capacitive performance of electrode material can be enhanced by increasing the specific surface area and adjusting the porosity. The active surface area can be improved by manipulating the dimensionality of electrode materials that enhance the percentage of exposed facets in the electrolyte. Hence, the unique 3D microstructures with interconnected pores provide a more accessible area for electrolyte diffusion as well as facile pathways for fast charge movement that leads to better electrical contact. Nevertheless, shortened diffusion pathways due to interconnected pores result in the acceleration of ion transfer during redox reactions, which is crucial for the electrode materials exhibiting high performance.[24] In this regard, the design and synthesis of 3D nano/micro-structures play a vital role in improving electrochemical performance of electrode materials for supercapacitors.

4.1.1 | Pristine 3D TMOs

The 3D TMOs are promising electrode materials for supercapacitors due to their interconnected porous structure and larger accessible surface area for the electrolyte. Among various TMOs, MnO_2 has been widely used for energy storage applications because of its very high theoretical capacitance (1380 F/g), low cost due to natural abundance, and non-toxicity.[92–94] The common crystal structures of MnO_2 are α, β, γ, δ, λ, and R as shown in Figure 4 with each phase having a different basic [MnO_6] octahedra unit.[95] Only a few of MnO_2 are electrochemically active, among these α (hollandite) and δ (birnessite) are suitable for supercapacitor applications. δ -MnO_2 has MnO_6 octahedral structure due to its crystal sharing double bonds with the neighboring crystal lattice, and its pore size is suitable enough to allow the insertion/de-insertion of ions.[96] α-MnO_2 is built from double chains of edge-sharing [MnO_6] octahedra that are linked at corners to form (2 × 2) + (1 × 1) tunnel structures, the size of (2 × 2) tunnel is 0.46 nm that is suitable for accommodation of alkali metal ions.[97]

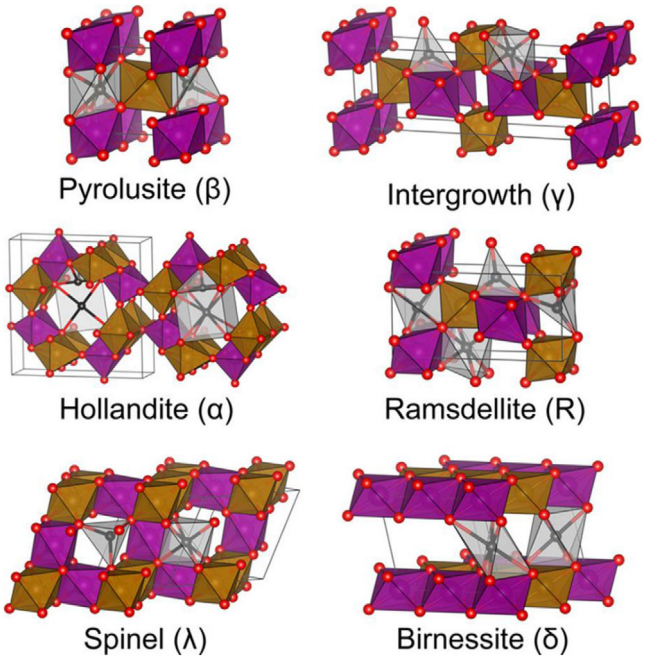

FIGURE 4 Common crystal structures of MnO_2 (Reproduced with permission from Ref. [95], 2017, ACS)

Different phases of MnO_2 can be obtained by using different synthesis routes. Synthesis route involving alkaline medium gives the layered δ -MnO_2 whereas medium to lower pH values favor denser phases of MnO_2 like α and β. Each structure of MnO_2 has different ionic and electronic conductivity so does the amount of charge stored by them. Lee and Goodenough used manganese oxide as a supercapacitor electrode for the first time in 1999.[98] Charge storage in MnO_2 involves both faradaic and non-faradaic contributions. Faradaic contribution comes from near surface-based fast reversible redox reactions involving the exchange of protons/cations with electrolyte as well as the transitions between Mn(IV)/Mn(III) within the electrode potential window. Capacitance of MnO_x is governed by the available valence state and hydrous state but the lifetime of MnO_x based supercapacitors depends on the microstructure and surface morphology of active material. Many factors affect the charge storage mechanism of manganese oxide such as morphology, crystallinity, the thickness of the electrode layer, and so on. Morphology of MnO_2 decides the active surface area, larger surface area leads to more active sites for charge storage. Researchers have reported various morphologies of MnO_x, namely nanoflowers, nanorods, nanowires, nanoneedles, nanobundles, and so on, which can be obtained by varying the reaction conditions during the synthesis process. Also, there is a trade-off between electronic conductivity of oxide and porous structure, as increasing crystallinity of MnO_x increases electronic conductivity, but with a decrease in

surface area. The thickness of the electrode layer also plays an important role; higher thickness limits the capacitance of electrode material as MnO_x has low electronic conductivity and requires a larger distance to be traveled by electron before reaching to the current collector. However, MnO_x performance is limited due to its low electronic conductivity (10^{-6}-10^{-3} S/cm), poor stability, and dissolution of MnO_x electrode upon cycling. The dissolution reactions can be understood through Equations (10) and (11), respectively.[99]

$$Mn_2O_3\,(s) + 2H^+ \rightarrow Mn^{2+}_{(aq)} + MnO_2\,(s) + H_2O \quad (10)$$

$$Or,\ 2\,MnO(OH) \rightarrow Mn^{2+}_{(aq)} + MnO_2(s) + 2OH^- \quad (11)$$

Several approaches have been carried out to prevent Mn oxides from dissolution during cycling, including the development of new electrolyte salts to avoid the formation of acidic species in solution and applying a protective shell to the Mn oxide surface. Other issues such as poor electronic conductivity and low surface areas of MnO_x materials can be addressed by making MnO_x nanostructures. Recently, 3D structures are leading because of their higher active surface area and short ion diffusion pathways than 2D structures. Yan et al. synthesized MnO_2 film with 3D and porous structure by hydrothermal method on 3D nickel foam substrate.[58] 3D MnO_2 films contain nanosheets and nanofibres and have amorphous as well as hydrous nature. The specific capacitance value obtained in half-cell at 1 A/g is 241 F/g within 0-1 V potential window in 1 M Na_2SO_4 electrolyte. The capacitive behavior, superior power characteristics, and cycling stability of MnO_2 electrodes are illustrated from the rectangular-shaped CV profiles, as well as preservation of rectangular shapes even at higher scan rates and less than 10% loss in discharge capacity after 1000 cycles. The excellent supercapacitive performance is due to the dispersion of MnO_2 on Ni foam that leads to direct electrical contact with the current collector, thus shortens the ion diffusion distance on exposing itself to electrolyte. Likewise, Shah et al. synthesized hierarchical porous 3D MnO_2 nanorod forest on carbon textile via hydrothermal method as shown in Figure 5.[100] In the three-electrode system, it displayed 961 F/g at 1 mA/cm^2 current density with 92% capacitance retention after 5000 cycles. The binder-free MnO_2 nanorod forest on carbon textile is promising for flexible supercapacitors, light-weight carbon textiles may lower the overall weight of the device as well as allow the high mass loading due to mesoporous structure. 3D porous MnO_2 film on nickel foam substrate was also synthesized by Yang et al. by CV electrodeposition method.[69] The thickness of the film and pore size was increased with an increase in deposition time. The electrochemical measurements were performed on a half-cell system with an electrolyte composed of 0.1 M $Mn(CH_3COO)_2$ and 0.1 M Na_2SO_4 maintained at a pH value 7. The CV curve with redox peaks confirms the pseudocapacitive behavior that involves charge storage through surface redox reactions as shown in Equation (12).

$$MnO_2 + xNa^+ + yH^+ + (x+y)\,e^- \leftrightarrow MnOONa_xH_y \quad (12)$$

The specific capacitance value obtained at 2 mA/cm^2 is 2790 mF/cm^2 and the retention was above 90% after 5000 GCD cycles at 5 mA/cm^2. Further, asymmetric supercapacitor assembled using MnO_2 film as a positive electrode and AC as a negative electrode exhibited a specific capacitance of 67 F/g, energy density of 37.22 Wh/kg, and 80% retention of capacitance at 2.5 mA/cm^2 after 1000 cycles. The 3D network of nanosheets, porous structure, high mass-loading, and direct deposition of electroactive material on current collectors lead to enhanced supercapacitive performance.

Similarly, Patil and his co-workers synthesized β-MnO_2 nanospheres using the chemical bath deposition method shown in Figure 6.[74] The electrochemical measurements in a half-cell system revealed the pseudo-capacitive behavior of the electrode. The value of specific capacitance obtained in 1 M Na_2SO_4 electrolyte was 994 F/g and 750 F/g at a scan rate of 5 mV/s, and at a current density of 2 mA/cm^2, respectively. The cycling stability was estimated during 3000 cycles within 0 to 0.8 V potential window at 5 mA/cm^2. The increase in capacitance up to 110.78% between 50 to 250 cycles is due to the activation of electrode material and finally, it decreased to 94.3% of the first cycle capacitance after 3000 cycles. Enhancement in the charge storing capacity is due to interconnected nanospheres leading to a uniform porous network which facilitates rapid ion diffusion and charge movement within the electroactive material. Further, β-MnO_2 positive electrode was combined with the O-SnS negative electrode to design all solid-state ASC using PVA-$LiClO_4$ gel electrolyte. The assembled ASC has a specific capacitance of 122 F/g at 5 mV/s, capacity retention up to 95.3% after 5000 cycles, an energy density of 29.8 Wh/kg, and power density of 1.25 kW/kg.

3D MnO_2 film on nickel foam was also synthesized by Tian et al. using CBD method.[75] The 3D porous microstructure with an average pore diameter of 3.8 nm was obtained as a result of interlinked round-shaped nanoplatelets of β-MnO_2. Electrochemical measurements were performed within the potential window of −1.2 to −0.2 V in 3 M KOH. The redox peaks observed in the CV curve at −0.8 to −0.2 V confirm the pseudocapacitive behavior of MnO_2 film, while other peaks are attributed to the

Review
doi.org/10.1002/elsa.202100187
Chemistry Europe
European Chemical Societies Publishing

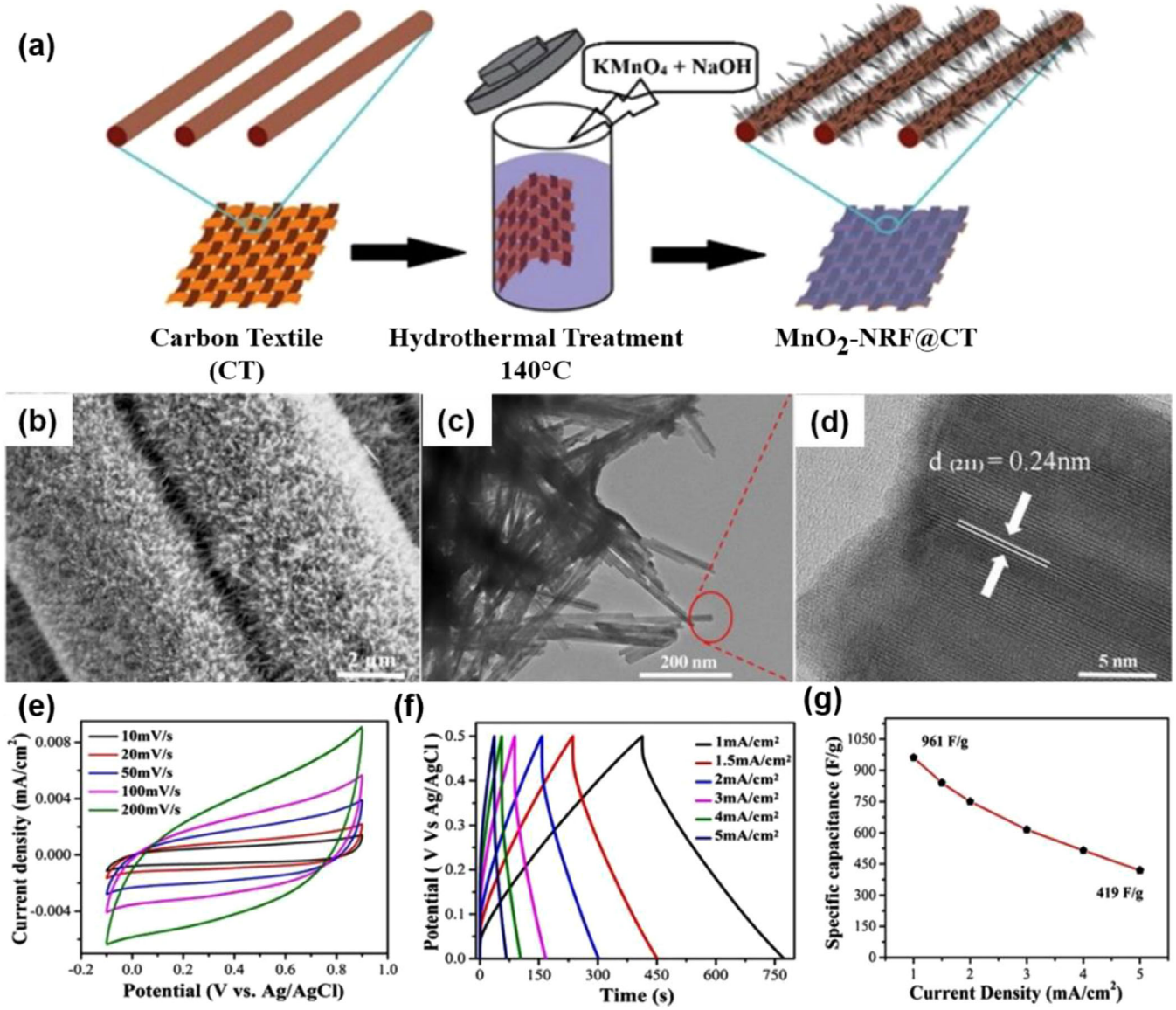

FIGURE 5 (a) Schematic diagram of the synthesis of α-MnO_2 nanorods forest; (b) SEM, (c) TEM, and (d) HRTEM images of α-MnO_2 nanorods forest; (e) CV at different scan rates, (f) GCD and (g) specific capacitances at different current densities of α-MnO_2 nanorods forest in three-electrode setup with 1 M Na_2SO_4 electrolyte (Reproduced with permission from Ref. [100], 2018, Elsevier)

oxidation/reduction process of Mn(II), Mn(III), and Mn(IV) as proposed in Equations 13 and (14).

$$MnO + OH^- - e^- \leftrightarrow MnOOH \quad (13)$$

$$MnOOH - e^- \leftrightarrow MnO_2 + H^+ \quad (14)$$

Electrochemical measurements performed in 3 M KNO_3 within the potential window of 0–1 V demonstrated symmetric and rectangular cyclic voltammograms that indicate double-layer capacitive behavior in a neutral medium. A specific capacitance of 1517 F/g was obtained at 1 A/g in 3 M KOH which is significantly higher than 546 F/g in 3 M KNO_3 at similar currents. Miao synthesized cost-effective marshmallow-like MnO_2 by simple one-step hydrothermal synthesis on carbon cloth.[101] The electrochemical performance of MnO_2/CC is evaluated in 1 M Na_2SO_4 as well as in 1 M KOH electrolyte. In 1 M Na_2SO_4, MnO_2/CC exhibited a capacitance of 624 mF/cm^2 (249.6 F/g) with 97.7% capacitance retention after 2000 cycles but in 1 M KOH MnO_2/CC showed a capacitance of 1092 mF/cm^2 (436.8 F/g) with 49.5% capacitance retention after 2000 cycles. The charge storage of MnO_2/CC is better in KOH because K^+ ion has more ionic conductivity than Na^+ ion and as K^+ is smaller in size, so it can intercalate easily, hence in KOH capacitance is contributed from the surface as well as bulk intercalation whereas in NaOH charge is stored mainly at the surface of active material. The cycling

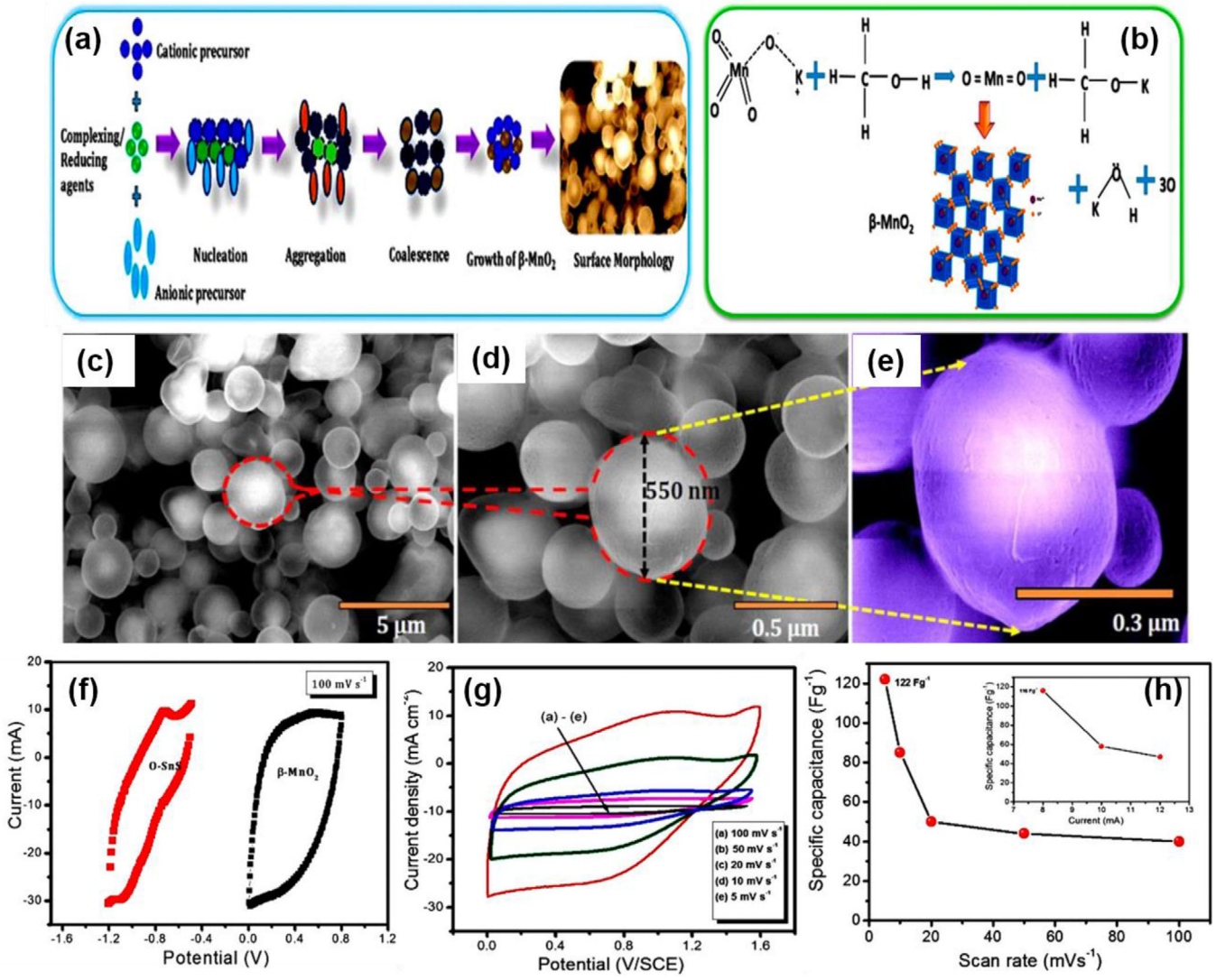

FIGURE 6 Schematic illustration of (a) synthesis procedure and (b) corresponding bond structure alterations of β-MnO_2 nanospheres; (c-e) FESEM images of β-MnO_2 at different magnifications; (f) CV of β-MnO_2 and O-SnS at 100 mV/s and (g) CV and (h) specific capacitance at different scan rates of β-MnO_2//O-SnS asymmetric cell. (Reproduced with permission from Ref. [74], 2018, RSC)

stability is better in NaOH because the charge is stored at the surface that leads to the stability of active material, whereas in KOH continuous intercalation/deintercalation deforms the crystal structure. Asymmetric coin cell supercapacitor (ACC) assembled with activated carbon anode delivered 18.46 Wh/kg energy density at 699.5 W/kg power density with 97.3 % cycling stability after 2000 cycles. Apart from MnO_x, iron oxides, especially Fe_2O_3 and Fe_3O_4 have been widely used in supercapacitors due to their abundant nature, easy accessibility, low-cost, and non-toxicity. However, to overcome the limitation of poor electronic conductivity to some extent, iron oxide can be grown over conducting substrate or nanostructures by altering the reaction conditions, which reduces the path length traveled by electrons. Li et al. have grown Fe_2O_3 nanoparticles on activated carbon cloth (CC) by simple hydrothermal synthesis.[59] Fe_2O_3@CC showed 570 F/g (1472 mF/cm^2) capacitance at 2 mA/cm^2 current density in the potential window of −1.0–0.0 V. Better performance of active material is due to the large surface area, porous network, and high conductivity of CC. Capacitive contribution is estimated to be 61% of the total charge stored by Fe_2O_3@CC at 4 mV/s. Moreover, when coupled with $Mn(OH)_2$ positive electrode, the $Mn(OH)_2$//Fe_2O_3@CC ASC delivered a volumetric energy density of 5.12 mWh/cm^3 at a volumetric power density of 14.24 mW/cm^3 and retained 3.57 mWh/cm^3 energy density even at a very high power density of 123.57 mW/cm^3 in 1 M $LiNO_3$ electrolyte. The ASC was also able to retain almost 97.1% of its initial capacitance after 8000 cycles within a wide potential window of 0–2.0 V. 3D NiO is explored for supercapacitors because of its highly reversible charge storage process, very high

theoretical capacitance (>3700 F/g), low toxicity, and low cost.[102–105] However, low electronic conductivity[106–108] and poor cycling stability due to volume alterations during repetitive charge/discharge processes as well as active material degradation during cycling limits their electrochemical performance.[109–111] Zhang et al. fabricated 3D hierarchical NiO nanosheets through a hydrothermal method that demonstrated very high areal capacitance of 1.3 F/cm^2 at 4 mA/cm^2 and superior cycling stability.[112] The assembled ASC with NiO nanosheets as cathode and Fe_2O_3 nanorods as anode has exhibited an energy density of 12.4 Wh/kg and a maximum power density of 951 W/kg. Meng et al. reported that NiO, synthesized through perchlorate ion explosion, can deliver a capacitance of 1863 F/g at 0.5 A/g current density.[113] Panigrahi et al. fabricated V_2O_5 3D array on carbon fabric that has exhibited a specific capacitance of 1098 F/g at 5 mV/s scan rate in 0.5 M K_2SO_4. Assembled SSC delivered 48.32 Wh/kg energy density at 0.49 kW/kg power density with 92% capacitance retention after 10,000 cycles at 15 A/g current density.[114] Similarly, several other 3D nanostructured TMOs such as Mn_2O_3 nanosphere/nanocube,[115] 3D hierarchical Co_3O_4,[77,86] 3D hierarchical architectures of hydrous RuO_2,[116] plate-like MnO_2[117] have shown remarkable specific capacitances of 345 F/g, 321 F/g at 0.2 A/g, 970 F/g at 1 A/g, 743.8 F/g, 628 F/g at 20 A/g, and 680.6 F/g at a scan rate of 1 mV/s, respectively. Currently, ternary TMOs have gained significant attention due to their improved conductivity and richer faradaic reactions than corresponding individual components. $CuCo_2O_4$,[118] $NiMn_2O_4$,[79] $ZnCo_2O_4$,[119] $MgCr_2O_4$,[80] and so on, have been widely explored for high-performance supercapacitor electrodes; among these $CuCo_2O_4$ is most prominent because of its intrinsic advantages such as superior electrochemical activity, excellent conductivity, light weight, and abundant resource.

Liu et al. fabricated $CuCo_2O_4$ nano-urchin on nickel foam substrate by using hydrothermal synthesis route and subsequent thermal treatment as shown in Figure 7.[62] The 3D nano-urchin microstructure that consists of numerous 1D porous nanowires of $CuCo_2O_4$ has several advantages such as (a) vacant spaces between nanowires leads to easy penetration of electrolyte, (b) 1D structure facilitates fast ion transportation due to reduced ion diffusion path, (c) porous structure results in large surface area, and (d) enhanced structural stability that improves the cycling stability. The electrochemical studies revealed a high specific capacitance of 1569.9 F/g at a current density of 0.6 A/g, and 98% capacitance retention after 4000 cycles. Further, ASC assembled with $CuCo_2O_4$ as a positive and AC as a negative electrode in 3 M KOH displayed an energy density of 23.9 Wh/kg at a power density of 593.2 W/kg and exhibited excellent cycling stability with 91.5 % capacitance retention after 2000 cycles. Spinel structured $NiMn_2O_4$ nanoparticles were also synthesized by Ray et al. using a sol-gel method.[79] It exhibited a capacitance of 875 F/g at 2 mV/s scan rate in 1 M Na_2SO_4 electrolyte. The assembled ASC with a potential window of 1.8 V demonstrated an energy density of 75.01 Wh/kg at a power density of 2250.91 W/kg. Similarly, $MgCr_2O_4$ nanoparticles,[80] $Zn_{0.6}Mn_{2.4}O_4$ nanoparticles,[120] $CuCo_2O_4$ composite octahedrons[118] have also delivered excellent specific capacitances. This infers that spinel are promising materials for high-performance supercapacitors.

4.1.2 | 3D TMO-based composites

Pristine TMOs suffer from intrinsically low electronic conductivity that results in poor rate performance and hence, has hindered their widespread use in practical supercapacitors. Making composites with other electronically conducting materials like conducting carbon, CNTs, graphene, polymer, Mxenes, and so on, can overcome the limitation of low electronic conductivity to some extent. Recently, carbon microelectromechanical systems (C-MEMS) technology is used to fabricate conducting carbon fibers on graphite substrate.[91] Performance has been improved by making a composite of highly porous 3D carbon fiber structure with highly electroactive RuO_2.[91] Maximum specific capacitance of 219.2 F/g is obtained for RuO_2 30 wt.%/CF composite at 0.5 A/g current density, that is nearly 2.27 times of pristine carbon fiber (CF). When the current density is increased to 3 A/g, the composite electrode still retained 54.8 % capacitance. An SSC was fabricated using RuO_2 30 wt.%/CF as electrodes material that exhibited a gravimetric energy density 74.2 Wh/kg with gravimetric power density 4333 W/kg. During the stability test performed at a current density of 2 A/g, the SSC retained 80.2% of the initial capacitance value after 3000 cycles.[91] Binder-free RuO_2/CF composite was synthesized by Chung et al. using the incipient impregnation method.[121] The amount of RuO_2 in the composite was increased with the number of impregnation cycles. On annealing the composite at 300°C, RuO_2 particles were converted into wrinkle-like shapes and some amount of hydrous RuO_2 was also converted into crystalline RuO_2. The specific capacitance of the composite was found to depend on the amount of RuO_2 present in the composite; it first increased then decreased with RuO_2 content. The maximum specific capacitance obtained for 12.23% RuO_2 loading, was 544 F/g at 2 mV/s in 2 M H_2SO_4. Cycling stability decreased with an increased amount of RuO_2 in the composite due to the fracture of carbon fiber during the electrochemical reaction. At low loading, RuO_2 particles are evenly distributed at the carbon fiber surface,

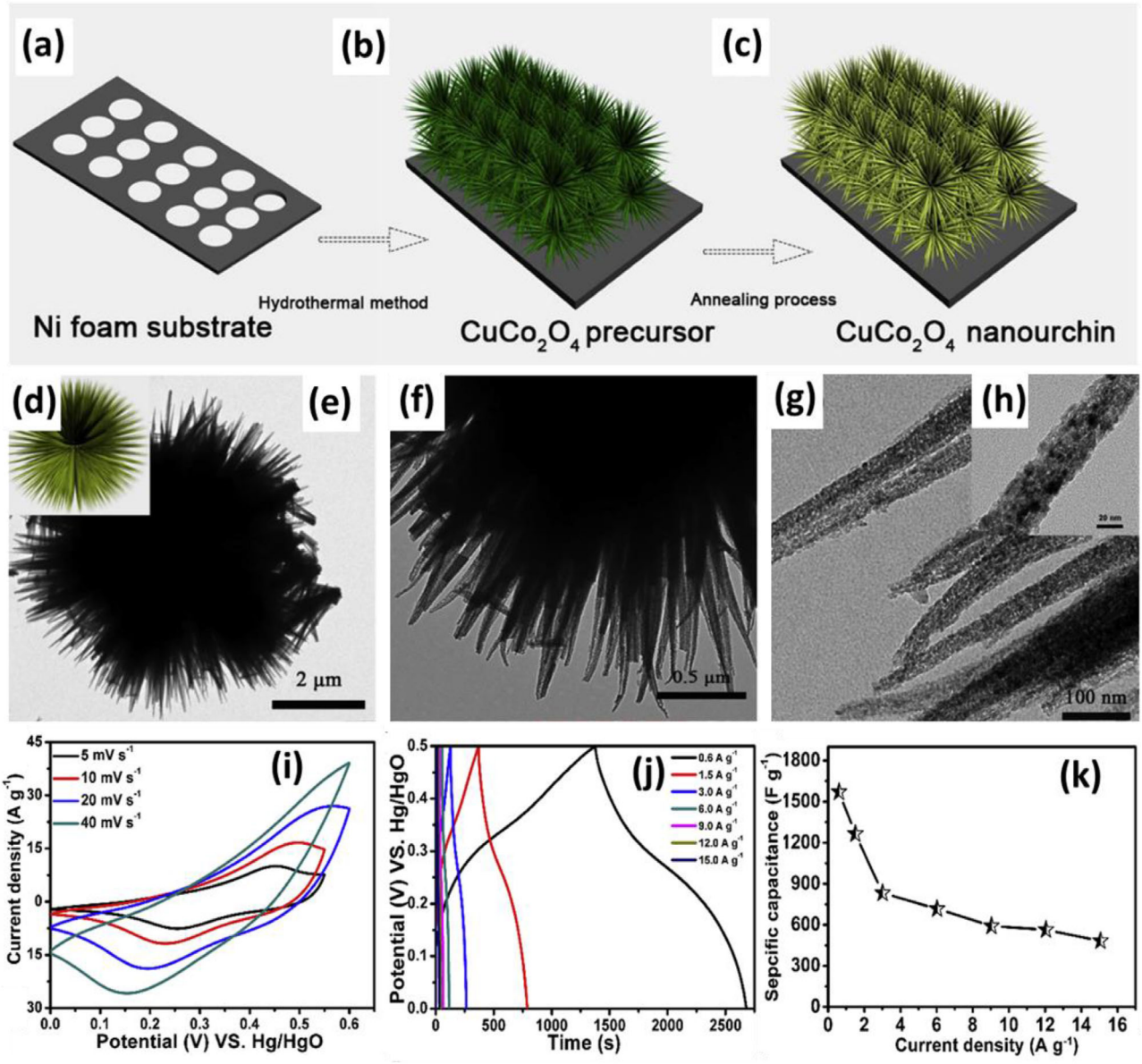

FIGURE 7 (a-c) Schematic representation of $CuCo_2O_4$ nano-urchin formation; (d) sketch and (e-h) TEM images of $CuCo_2O_4$ nano-urchin; (i) CV at different scan rates, (j) GCD at different current densities, and (k) specific capacitance at different current densities of $CuCo_2O_4$ nano-urchin in 3 M KOH aqueous electrolyte system. (Reproduced with permission from Ref. [62], 2018, Elsevier)

but, when loading is high, then RuO_2 particles start aggregating and form bigger isolating particles and lose coordination with the fiber surface. Also, with increasing RuO_2 loading in composites, crystalline RuO_2 content increases but hydrous RuO_2 decreases. Crystalline RuO_2 provides electron conductivity whereas hydrous RuO_2 hosts proton in acidic medium, but overall capacitance decreases with an increase in the RuO_2 loading in the composite. To augment the performance further, hybrid composite of TiO_2/RuO_2 was synthesized by Park et al. using combustion driven synthesis method in which self-propagating combustion waves pass through the precursor material TiO_2 and nitrocellulose provide the sacrificial layer of carbon on TiO_2,[90] as shown in Figure 8. The sacrificial layer was later replaced with RuO_2 nanoparticles by immersing hybrid composite in a solution of $KRuO_4$. This synthesis method gives two morphologies namely, core-shell TiO_2@RuO_2 (CSTR) nanostructures or RuO_2 clusters embedded with TiO_2 nanoparticles (RCET) depending on the reaction parameters. CSTR showed excellent gravimetric capacitance of 1200 F/g at 0.5 A/g current density while RCET only gave 760 F/g. CSTR also exhibited outstanding cycling stability of 95.2% after 10,000 cycles which is far better than the commercial RuO_2 capacitor (600 F/g capacitance and cycling stability 72%). This outstanding performance is due to the fast diffusion

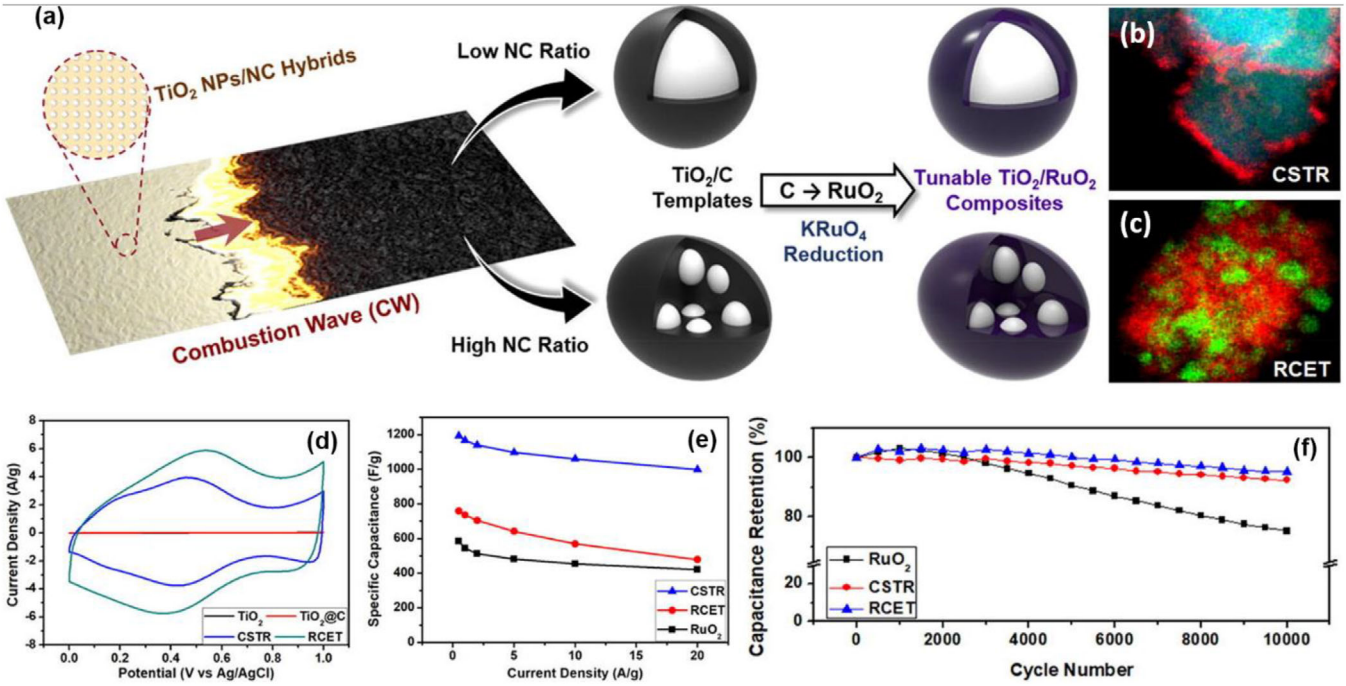

FIGURE 8 (a) Schematic illustration of combustion synthesis of TiO_2/RuO_2 hybrid composites; EDX mapping of (b) CSTR and (c) RCET; comparison of (d) CV curves (at 10 mV/s), (e) specific capacitance (at different current densities) and (f) cyclic stability (at 100 mV/s) (Reproduced with permission from Ref. [90], 2020, Elsevier)

of protons which is facilitated by an amorphous RuO_2 shell and physiochemically stable TiO_2 core. Oxygen-deficient binary hybrid material $W_{18}O_{49}$-RuO_2 synthesized by Lichchhavi et al. by simple hydrothermal method[122] has shown a superior specific capacitance value of 1126 F/g at a scan rate of 1 mV/s and 1050 F/g at 1 mA, which is better than the capacitance of 812 F/g at 1 mV/s reported for pristine RuO_2 nanoparticles in 1 M H_2SO_4. Excellent performance of hybrid material can be attributed to the synergies between $W_{18}O_{49}$, with high conductivity due to oxygen vacant sites and high surface area, and RuO_2, providing paths for fast ion movement and availability of abundant active sites for electrochemical reactions.

Kuo et al. synthesized RuO_2-Ta_2O_5/Polyaniline (RuO_2-Ta_2O_5/PANI) ternary hybrid composite by sintering and electrodeposition.[123] Hybrid composite exhibited a capacitance of 428 F/g at 0.5 mA/cm^2 current density. It also showed a maximum energy density of 26.7 Wh/kg at a current density of 0.5 mA/cm^2 and a maximum power density of 2.4 kW/kg at a current density of 4.0 mA/cm^2. The synergistic effect of RuO_2-Ta_2O_5 porous structure and PANI nano-fibrous structure with high conductivity of PANI gives an improved performance as compared to single active material. Zhang et al. synthesized the rich oxygen-deficient bulk δ-MnO_2-Carbon composite (MnO_2-C) by complex induced chemical precipitation method.[83] The overall electrochemical performance is enhanced as compared to oxygen-rich MnO_2 due to the combined effect of improved electronic conductivity, enhanced charge transfers due to local electric field around oxygen vacancies, and low diffusion energy barrier for reaction in MnO_2-C. MnO_2-C when electrochemically characterized exhibited a capacitance of 287 F/g at 1 A/g and could retain a capacitance of 225 F/g at a current density of 20 A/g. When MnO_2-C was combined with MoO_{3-x} anode, the assembled ASC could provide an energy density of 54.2 Wh/kg and a power density of 3.3 kW/kg. A cycling durability test was also performed over 10,000 cycles, which showed 83.9% capacitance retention. Vanadium doped α-MnO_2 (V-MnO_2) was synthesized by Wu et al. using the hydrothermal method.[124] Vanadium doping gave enhanced electronic conductivity to V-MnO_2. Within the potential window of −0.1 to 0.9 V (vs Ag/AgCl in 1 M Li_2SO_4), V-MnO_2 showed a capacitance of 414 F/g at 5 mV/s scan rate and could retain 136 F/g at 500 mV/s scan rate. The assembled V-MnO_2(+)//Ti_3C_{2x}(−) ASC delivered a capacitance of 76 F/g at 5 mV/s, and retained 53% of capacitance at 200 mV/s. The ASC delivered an energy density of 46 Wh/kg, and even at a high power density of 3.2 kW/kg, it could deliver an energy density of 36 Wh/kg.

Kumar et al. reported supercapacitive performance of Mn_3O_4 anchored over CNT prepared by direct decomposition of Mn-hexacyanoferrate complex on CNT, as shown in Figure 9.[125] The as-fabricated CNT- Mn_3O_4 composite electrode showed electrochemical activity within the potential window of 0–0.8 V versus Ag/AgCl in

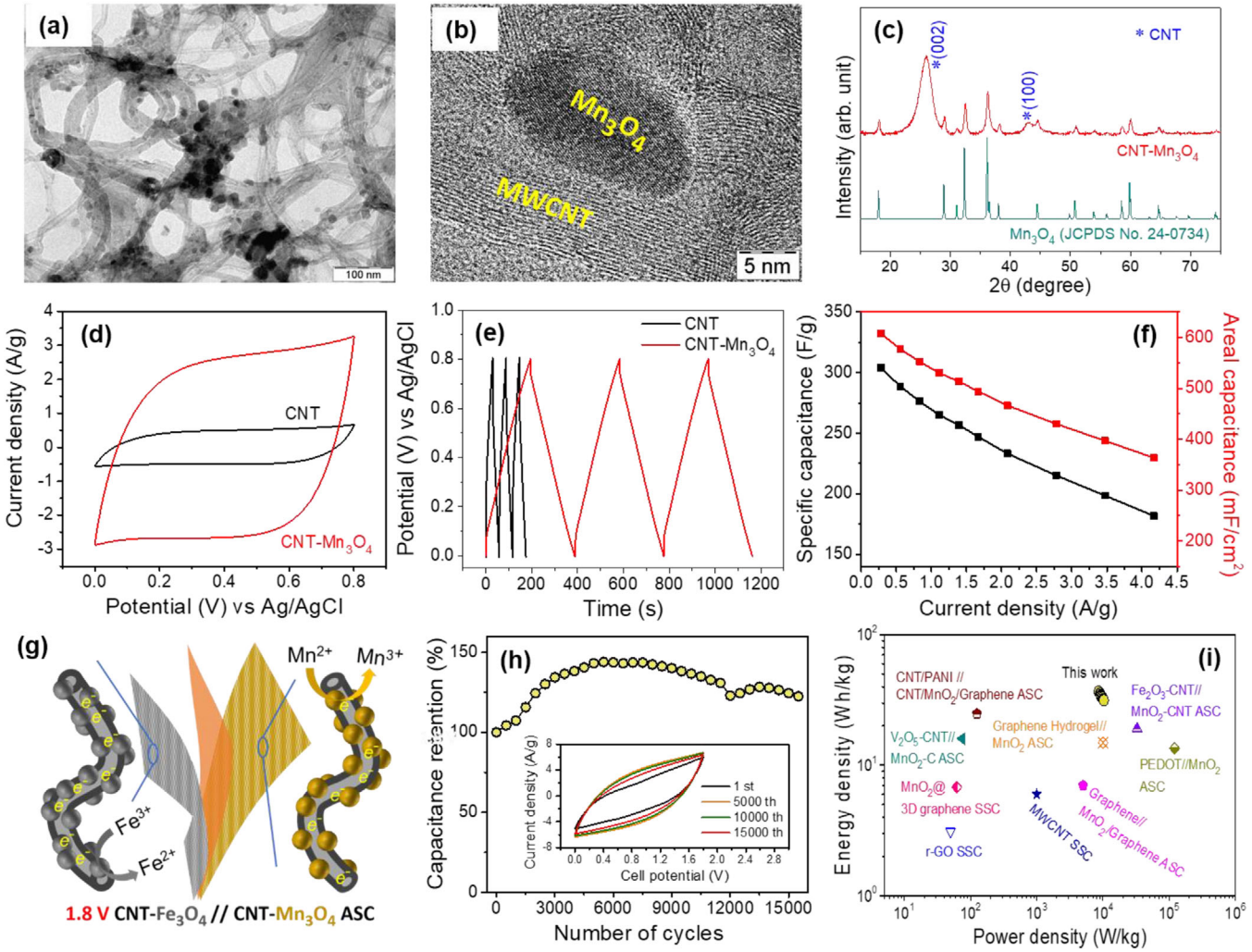

FIGURE 9 (a) TEM, (b) HRTEM and (c) XRD patterns of CNT-Mn_3O_4 nanocomposite; comparison of (d) CVs (at 10 mV/s), (e) GCD curves (at 1.12 A/g), and (f) specific capacitances of CNT and CNT-Mn_3O_4 in 1 M Na_2SO_4 electrolyte; (g) schematic illustration of CNT-Fe_3O_4//CNT-Mn_3O_4 ASC cell, its (h) cycling performance, and (i) Ragone plot comparing its performance with other ASCs reported in the literature. (Reproduced with permission from Ref. [125], 2018, ACS)

1 M Na_2SO_4 electrolyte. The composite electrode exhibited a capacitance of 453 F/g at 10 mV/s which is much higher than the pristine CNT electrode. Excellent improvement in the electrochemical performance of CNT-Mn_3O_4 composite as compared to pristine CNT can be explained by the synergistic effects from pseudocapacitive Mn_3O_4 and high electronically conducting CNT. Redox reaction involved in charge storage can be explained from Equation (15).[126,127]

$$MnO_x(OH)_y + \delta Na^+ + \delta e^- \leftrightarrow Na_\delta MnO_x(OH)_y \quad (15)$$

CNT-Mn_3O_4 composite electrode showed excellent electrochemical stability over 16,000 cycles and retained ~100% capacitance during the process. When combined with CNT- Fe_3O_4, the ASC showed a capacitance of 135.2 F/g at 10 mV/s within the potential window of 0.0–1.8 V in neutral 1 M Na_2SO_4 electrolyte. moreover, the ASC device exhibited excellent cycling stability by retaining 100% capacitance even after 15,000 CV cycles. Recently, Zhang et al. used triethanolamine (TEA) as a complexing agent in the synthesis of MnO_2 by complex induced chemical precipitation method to optimize the engineering of Mn atoms in MnO_2.[128] Engineering of Mn atoms increases electronic conductivity and generates oxygen defects, while electron dislocation creates built-in electric potential and results in fast electrolyte ion diffusion. MnO_2-TEA exhibited a capacitance of 417.5 F/g at a current density of 1 A/g. The ASC assembled with MoO_{3-x} anode delivered a high energy density of 57.4 Wh/kg at a power density of 450 W/kg. Heydari et al. synthesized a ternary composite of PANI/MoS_2-MnO_2 by hydrothermal method followed by electrochemical polymerization.[129] Initially, a few layers of MoS_2 are exfoliated with specific solvent followed by hydrothermal growth of MnO_2 over

those MoS_2 sheets, and finally, PANI is polymerized electrochemically over MoS_2-MnO_2 composite. MoS_2 provides sub-layer support to the structure, MnO_2 gives a good electrochemical performance, and PANI provides electronic conductivity to composite. Ternary composite PANI/MoS_2-MnO_2 delivered a capacitance of 479 F/g that is better than binary composite MoS_2-MnO_2 with a capacitance of 358 F/g at 5 mV/s. The SSC exhibited a capacitance of 259 F/g at a current density of 1 A/g, delivered an energy density of 35.97 Wh/kg at a power density of 500 W/kg, and retained 94.1% of initial capacitance after 4000 cycles at a current density of 16 A/g. Since, Fe-based oxides also suffer from low electronic conductivity, low charge storage, poor rate performance, and stability issues, various efforts have been made to overcome these issues.[130] Dai et al. prepared porous core-shell Fe_2O_3@Fe_3C@C nanochains and used them for electrochemical supercapacitors.[131] Fe_2O_3@Fe_3C@C showed 611 C/g capacity at a current density of 1 A/g with good rate capability. The ASC NiCo-CHH (carbonate hydroxide hybridized)//Fe_2O_3@Fe_3C@C delivered an energy density of 95.2 Wh/kg at a power density of 1767.3 W/kg with moderate cycling stability of 84.2% after 10,000 cycles at a current density of 10 A/g. The composite showed a BET surface area of 150 m^2/g and porous structure with pore size within 3–15 nm, that leads to abundant charge storage and better cycling stability. The synergic effect between porous nanostructure of pseudocapacitive Fe_3C and Fe_2O_3, and highly conductive carbon gives rise to an enhanced performance of the composite. Raut et al. deposited MWCNTs on stainless steel (SS) substrate by dip and fry method followed by the deposition of Fe_2O_3 nanoparticles by successive ionic layer adsorption and reaction (SILAR) method.[89] The solid-state symmetric supercapacitor (SSS) assembled with MWCNTs/Fe_2O_3 in polyvinyl alcohol (PVA) LiCl gel electrolyte showed capacitance of 70.2 F/g at a current density of 0.57 A/g and delivered an energy density of 9.74 Wh/kg (equivalent to 24.36 mWh/cm^3) at a power density of 487 W/kg (equivalent to 1218 mW/cm^3). Moreover, the SSS demonstrated a good cycling stability with 75% capacitance retention after 1500 cycles. It has been demonstrated that Fe_3O_4 composites with conducting polymer reduce the degradation of material during electrochemical reaction. For example, Fe_3O_4-PANI composite prevents decaying of the electroactive materials as well as increases the capacity.[132] PANI is a non-toxic and low-cost conducting polymer. In the composite, it acts as a shell to active material preventing degradation and hence increasing the cycling stability as well as capacity.[133–135] Recently, Javed fabricated Fe_3O_4 nanoparticles decorated on PANI by low-temperature hydrothermal method.[136] Fe_3O_4 nanoparticle showed capacitance of 1351.13 F/g at a current density of 1 A/g that is further improved in Fe_3O_4/PANI composite with a capacitance of 1669.18 F/g at similar current densities. Moreover, the capacitance retention increased from 92% to 96.5% during 25,000 GCD cycles at 15 A/g after the PANI modification. Enhanced performance can be attributed to enhanced electron conductivity and mesoporous network of Fe_3O_4/PANI composite. PANI increases the conductivity of Fe_3O_4/PANI composite because it forms a covalent bond with Fe_3O_4 nanoparticles responsible for pseudocapacitive charge storage.[137] Other than oxides of ruthenium, manganese, and iron, cobalt-based oxides are also explored widely because of their high theoretical specific capacitance of 3560 F/g.[138] Recently, Rashti et al. used zeolitic imidazolate framework-67 (ZIF-67) for designing porous nanostructure of Co_3O_4/$NiCo_2O_4$ composite.[139] The composite has shown a capacitance of 770 F/g at 1 A/g current density with 80% rate capability when the current density is increased to 20 A/g, and a 70% capacitance retention after 10,000 cycles. The assembled Co_3O_4/$NiCo_2O_4$//AC ASC delivered an energy density of 38.8 Wh/kg at a power density of 10 kW/kg. Also, NiO/Ni/CNT composites have demonstrated a capacitance of 777.5 F/g at a current density of 1 A/g [140] and NiO-rGO composite could deliver a capacitance of 171.3 F/g at 0.5 A/g.[141] Samuel et al. prepared ZnO/MnO_x nanoflowers for supercapacitor electrodes.[142] First, ZnO nanoflowers were prepared over Ni nanocubes then MnO_x was deposited over ZnO nanoflower petals. A capacitance of 556 F/g at 1 A/g could be achieved for the ZnO/MnO_x nanocomposite along with 96% cycling stability after 10,000 cycles in Na_2SO_4 electrolyte. Charge storage reaction for ZnO-based electrodes involves the intercalation/deintercalation of Na^+ ions into ZnO structure according to the following Equation (16).

$$ZnO + Na^+ + e^- \leftrightarrow ZnO - Na \quad (16)$$

The flower-like morphology and intermediate voids allow easy electrolyte wetting and fast-ion movement for better charge storage. Moreover, the reversibility of reactions is enhanced with the help of pseudocapacitive MnO_x, which helps in better absorption of electrolytic ions.[5] The SSC operated within the potential window of 0–0.9 V, delivered energy and power densities of 16 Wh/kg and 225 W/kg, respectively. Wang et al. reported the synthesis of highly ordered NiO/ZnO *p-n* heterojunction using a soft template and facile hydrothermal methods.[64] The bimetallic oxide composite has shown a capacity of 1394 C/g at 1 A/g and can retain a capacity of 560 C/g at 20 A/g. The *p-n* junction formed at the interface of NiO and ZnO facilitates charge transfer, whereas a highly porous 3D structure delivers enhanced storage performance. Yang et al. prepared β-Bi_2O_3 nanoparticles decorated on rGO nanosheets using the hydrothermal method.[143] The composite has

Review
doi.org/10.1002/elsa.202100187
Chemistry Europe
European Chemical Societies Publishing

achieved a capacitance of 196 F/g at 1 A/g in 1 M KOH electrolyte with cycling stability well above 99% after 3000 cycles. Sun et al. deposited V_2O_5 particles over vertically aligned CNTs to form V_2O_5/VACNTs composite. The composite has delivered an energy density of 32.3 Wh/kg with a power density of 118 W/kg and 76% capacitance retention after 5000 cycles.[144] In recent years, spinel metal oxide nanoparticles have emerged as promising materials for energy storage applications.[145] Also, carbon-doped with heteroatoms have shown improved performance because of the change in electron arrangements and enhancement in the electron donor properties. Furthermore, dual heteroatom doping leads to superior performance due to synergistic effects. Inspired by these facts, Li et al. synthesized sulfur and nitrogen co-doped activated $CoFe_2O_4$@C nanotubes.[146] The synergistic effect between spinel metal oxide, heteroatom doping, and sp^2 hybridized carbon leads to a superior capacitance (1053.60 F/g at 1 A/g) in KOH electrolyte, high energy and power combination as well as good capacitance retention (93.15% at 30 A/g after 5000 cycles). Mijailović et al. reported core-shell carbon fibre@$Co_{1.5}Mn_{1.5}O_4$ composite electrode consisting of redox-active shell ($Co_{1.5}Mn_{1.5}O_4$) and conductive core (carbon fiber).[147] Benefitted by the synergies between component materials, the core-shell structured electrode exhibited a capacitance of 384 F/g at 0.28 A/g in half-cell configuration, along with a good cycling stability, similar 3D spinel-based composite electrodes like VCFs@$MnCo_2O_4$,[148] have shown improved specific capacity of 48.4 mAh/g at 2 A/g as compared to pristine $MnCo_2O_4$, indicating effectiveness of the process of composite formation to get the benefit from individual component materials.

4.2 | 2D TMO-based materials for supercapacitors

2D materials have shown significant potential in electrochemical energy storage devices due to the following merits:

- Ion diffusion pathways are minimized significantly due to ultrathin thickness (one atomic layer thick for graphene) and large lateral size in a 2D layered porous structure.
- Surface atoms are exposed from both the sides of 2D sheets that leads to a very high specific surface area and provides abundant active sites for electrochemical reactions. The 2D structure also results in a large interface between electrode and electrolyte and hence the ionic resistance is minimized.
- In-plane defects in 2D materials act as active sites to enhance the charge storage capacity, and thus lead to higher specific capacitance and energy-power densities.
- The 2D hierarchical porous structure facilitates long cycling stability because volume changes during charge/discharge cycles can be greatly buffered by the free space between interlayers.[24,149]

Hence, the 2D TMOs have huge potential to be exploited as electrodes for high-performance supercapacitors. In the following subsections, we will discuss the design and electrochemical performance of various 2D pristine TMOs and their composites.

4.2.1 | Pristine 2D TMOs

So far TMO based electrodes have demonstrated electrochemical performance far below their theoretical limits that can be attributed to their intrinsic low-conductivity, short carrier-diffusion lengths, and so on, and hence their limited applications in practical devices. However, researchers have come up with possible solutions with (a) surface kinetics modification,[150,151] (b) binder-free composite fabrication using conducting substrate such as graphene,[152] carbon,[151,153] and metal porous foams[154–156]; and (c) synthesis of 2D nanostructures with high porosity and surface area.[157,158] In this regard, Zhao et al. has grown oxygen-deficient ultra-thin nanosheets of MnO_2 on Ni foam substrate by hydrothermal method followed by vacuum annealing.[159] Vacuum annealing changes some Mn^{4+} to Mn^{3+}. Maximum specific capacitance is obtained at a current density of 1 A/g is 522.5 F/g in 1 M Na_2SO_4 electrolyte. When MnO_2 ultra-thin nanosheets cathode is assembled in an ASC with activated carbon anode, it worked in a wide potential window of 0–2.0 V in aqueous 1 M Na_2SO_4. Also, the ASC exhibited an energy density of 18.6 Wh/kg at a specific power density of 1 kW/kg. A cycling stability test is also performed over 5000 cycles, during which the ASC retains 95.3% of its initial capacitance value. Defect engineering can change the electronic and internal structure of MnO_2. In this case, oxygen deficiency increases the electronic mobility of MnO_2 as well as generates more surface-active sites responsible for superior performance. Similarly, Samal et al. synthesized 2D layered δ-MnO_2 by microwave irradiation method and then oxygen vacancies were created with UV/O_3 treatment.[88] Oxygen deficient δ-MnO_2 (δ-MnO_2-UVT) have more surface area, electronic conductivity, and electroactive sites. δ-MnO_2-UVT and pristine δ-MnO_2 have shown capacitances of 609.6 F/g and 411.1 F/g, respectively, in KOH electrolyte at a current density of 8 A/g. The assembled δ-MnO_2-UVT//F-MWCNT ASC displayed a potential window of 0–1.5 V and exhibited a capacitance of 125 F/g at 0.5 A/g, an energy density of 39 Wh/kg at a power

doi.org/10.1002/elsa.202100187

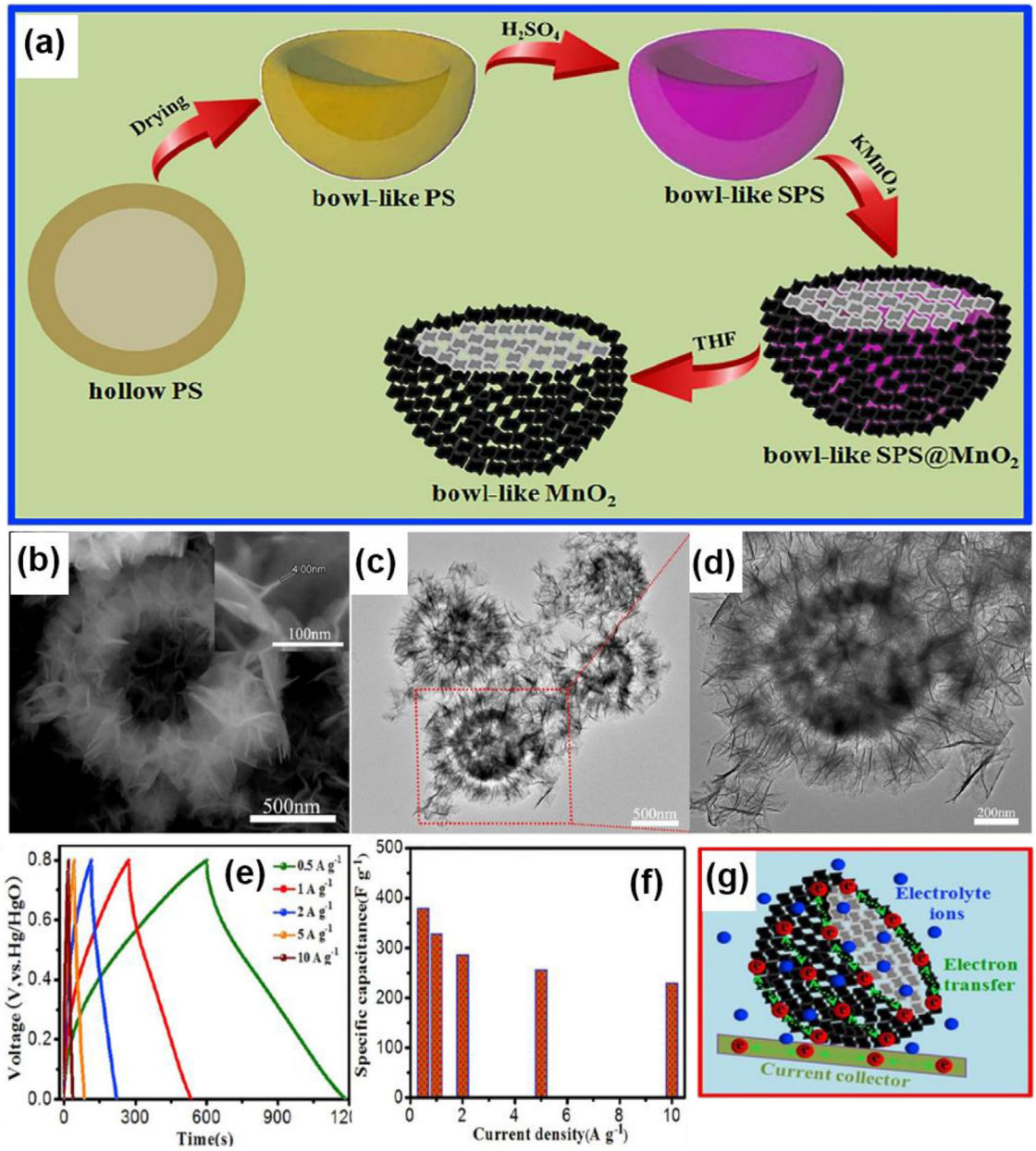

FIGURE 10 (a) Scheme of bowl-like MnO_2 nanosheets fabrication; (b-d) FESEM images of bowl-like MnO_2 nanosheets; (e) GCD and (f) specific capacitance of bowl-like MnO_2 nanosheets at different current densities in 1 M Na_2SO_4 electrolyte and its (g) charge transfer mechanism illustration. (Reproduced with permission from Ref. [161], 2018, Elsevier)

density of 468.7 W/kg, and a cycling stability of 84.7% after 5000 cycles. Several other TMOs with 2D nanostructured morphologies of manganese oxide such as Mn_2O_3 nanowalls thin film,[160] bowl-like MnO_2 nanosheets,[161] MnO_2 nanosheets,[162] and so on, have also been designed and fabricated which have exhibited high specific capacitance as well as energy-power density values. Liu et al. fabricated bowl-like MnO_2 nanosheets by template-assisted hydrothermal method as shown in Figure 10.[161] In the half-cell system, it displayed 379 F/g at 0.5 A/g current density and retained 87.3% capacitance after 5000 cycles. The excellent performance is due to a unique nanostructure with several benefits such as high surface area, higher electroactive sites for redox reactions, and short channels for diffusion.

Further, hierarchical porous ultrathin nanosheets of Co_3O_4 are deposited on Ni foam (NF) with the help of PVP as directing agent by Kang and co-workers.[163] The P-Co_3O_4-NS@NF achieved a capacity of 1196.5 mC/cm^2 at a current density of 5 mA/cm^2, with a capacity retention of 105% after 5000 cycles. In full-cell configuration, the P-Co_3O_4-NS@NF//AC ASC showed a capacitance of 141.6 F/g at 1 A/g and could deliver an energy density of 51.7 Wh/kg at a power density of 1125 W/kg along

with 91.8% capacitance retention ability after 15,000 cycles. The porous structure and ultrathin nanosheets (4 nm in thickness) promoted deep diffusion of ions inside the active material leading to enhanced performance. Similarly, Co_3O_4 nanosheets are also fabricated by Umar et al. using the hydrothermal synthesis route.[61] The prepared electrode has shown enhanced specific capacitance of 1455.64 F/g at 1 A/g current density in 3 M KOH electrolyte. The assembled SSC has shown an energy density of 22.51 Wh/kg and maximum power density of 311.68 W/kg at 1 A/g with capacitance retention of 82.52% after 2000 cycles. The ASC also exhibited good electrochemical stability with 94.1% capacitance retention after 2000 cycles. Likewise, ultrathin nanosheets of Co_3O_4 on nickel foam prepared by Zhou et al. using a hydrothermal route, exhibited a high specific capacity of 882 C/g at 2 A/g, and the assembled ASC has demonstrated an excellent energy density of 66.6 Wh/kg at a power density of 2250 W/kg.[164] Sethi et al. designed and synthesized NiO nanoflakes using mixed solvent solvothermal method at low temperature.[65] NiO nanoflakes showed a specific capacitance of 305 F/g at 5 mV/s scan rate in 2 M KOH electrolyte with high-rate capability and cycling stability. However, the assembled SSC could only deliver an energy density of 5.3 Wh/kg at a power density of 225 W/kg with a cycling stability 84% after 5000 cycles measured at 8 A/g.

2D nanostructures of spinel-based TMOs are fascinating from energy storage perspective and $ZnCo_2O_4$ is particularly attractive due to its natural abundance, low toxicity, and multiple compositions. However, poor efficiency of material utilization and low electronic conductivity are some of the challenges that need to be addressed. To overcome these obstacles, researchers combined $ZnCo_2O_4$ nanostructures with carbon-based materials and conducting metals, and also introduced oxygen vacancies to enhance conductivity. This idea was implemented by Xiang et al. as they synthesized $ZnCo_2O_4$ nanosheets with oxygen vacancies using a hydrothermal method and $NaBH_4$ reduction treatment.[165] The prepared supercapacitor electrode exhibited excellent specific capacitance as high as 2110.6 F/g at 1 A/g. Electrochemical results revealed improved electronic conductivity and rich active sites of the prepared oxygen-deficient electrode material. Interestingly, the assembled ASC delivered a high energy density of 34.6 Wh/kg at a power density of 160 W/kg. Similarly, Sahoo et al. prepared Fe-Ni-Co ternary oxide nanoflake arrays on nickel foam substrate.[166] The prepared electrode displayed a specific capacitance of 867 F/g and retained 92.3% of capacitance after 10,000 cycles. The assembled ASC delivered an admirable energy density of 40 Wh/kg and retained 87.4% of its initial capacitance value after 5000 cycles. The electrochemical performance of iron oxide-based electrodes is enhanced by combining it with highly conductive metallic nickel and high-capacity Co.[166] Also, a 2D Cu-Ni-Co ternary metal oxide nanoflake array was synthesized by Hussain et al. using hydrothermal route[167] that exhibited superior specific capacitance of 2615 F/g at 1 A/g. Similarly, Zn-Ni-Co oxide on Ni foam,[168] and $CuCo_2O_4$ nanosheets on Ni foam[169] have displayed excellent specific capacitances of 1837 F/g and 1595 F/g, respectively, at a current density of 1 A/g. From the foregoing, it can be surmised that 2D mixed structures grown on Ni foam are appealing as supercapacitor electrodes.

4.2.2 | 2D TMO-based composites

Electrochemical performance of 2D electrode materials can be improved further by composite formation with other electroactive materials. This results in a further increase in the electrochemically active sites, facilitation of electron and ion movements owing to the synergies between different component materials in the composite structure. Recently, for the first time, Mao et al. prepared Ag_2O intercalated hollow MnO_2 (Ag_2O-HMMnO_2) by a facile in-situ growth and self-sacrificing template method as shown in Figure 11.[170] Hollow inner space acts as the channel for fast-ion transportation whereas the vast space between neighboring MnO_2 nanosheets acts as a reservoir for the diffusion/storage of ions. Benefitted by such an interesting structure, the Ag_2O-HMMnO_2 electrode exhibited a capacitance value of 374 F/g (5.4 F/cm^2) at a high mass loading of 14.52 mg/cm^2. When assembled in an ASC, the Ag_2O-HMMnO_2//PANF@α-FeOOH ASC could deliver a high volumetric energy density of 7.33 mWh/cm^3 at a power density of 1.93 W/cm^3 that is around six times higher than the performance exhibited by the ASC assembled with pristine MnO_2. The ASC has shown excellent cycling performance, with 95.25% retention of initial capacitance after 12000 cycles. Improved performance of Ag_2O-HMMnO_2 can be attributed to its hierarchical porous structure which prevents buffer solution variation, accommodate internal strain, prevents structure collapse and MnO_2 aggregation.

Also, the heterostructure of $CuCo_2O_4$ and MnO_2 is synthesized by Chanda et al.[171] First copper cobaltite ($CuCo_2O_4$) is grown on carbon fabric by simple hydrothermal method followed by hydrothermal deposition of MnO_2 nanosheets. The nanocomposites have shown excellent electrochemical performance owing to the morphology-controlled nanoforms and high electronic conductivity of the carbon fabric. As a result, the nanocomposite displayed a capacitance of 1458 F/g at a current density of 0.5 A/g and a good cycling stability with 93% capacitance retention after 5000 cycles. The assembled

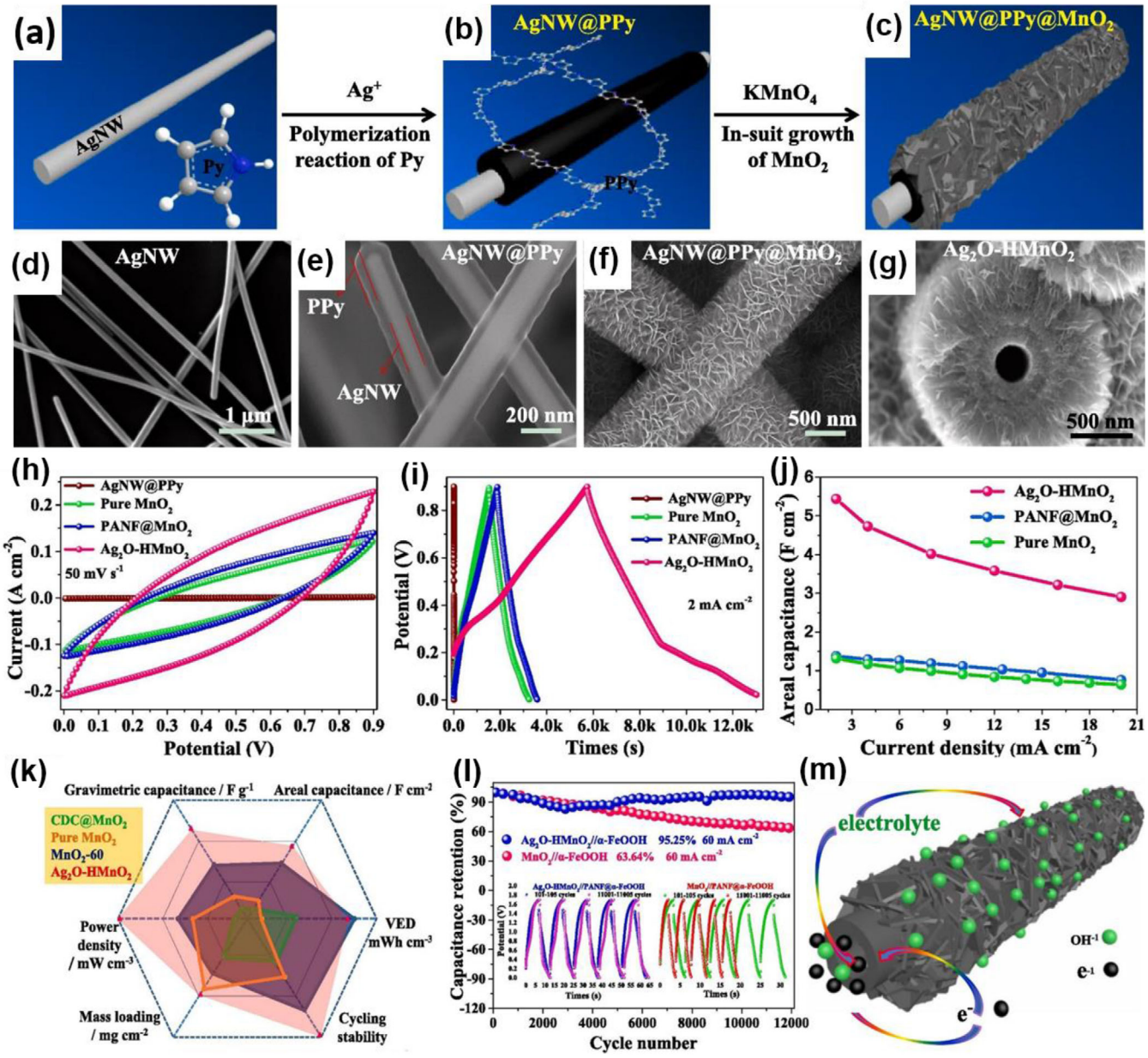

FIGURE 11 (a-c) Schematic synthesis of Ag_2O-$HMnO_2$ electrode; SEM images of (d) Ag nanowire (NW), (e) AgNW@Ppy, (f) AgNW@Ppy@MnO_2 and (g) $Ag_2O/HMnO_2$ electrodes; comparison of (h) CV (at 50 mV/s), (i) GCD (at 2 mA/cm^2), and (j) areal capacitance (at different current densities) profiles of different materials in half-cell configuration with 1 M Na_2SO_4 solution. (k) Radar chart with different electrochemical parameters of $Ag_2O/HMnO_2$//a-PANF@α-FeOOH asymmetric cell and its (l) cycling studies and (m) charge-discharge mechanism illustration. (Reproduced with permission from Ref. [170], 2018, Elsevier)

SSC device delivered an energy density of 64.1 Wh/kg and a power density of 1.5 kW/kg. Huang et al. synthesized Mn_3O_4 nanoflakes/reduced graphene oxide composites with moderate pore size and (O =)C-O-Mn bonds.[85] Chemical precipitation method was used to grow Mn_3O_4 nanoflakes on the graphene oxide surface. Structural stability of electrode is due to the (O =)C-O-Mn bonds between Mn_3O_4 and graphene as a result of annealing. The 5–10 nm pore size of Mn_3O_4 leads to improved electrolyte ion diffusion and enhanced charge storage capacity. The composite exhibited remarkable electrochemical performance with a specific capacitance of 351 F/g at 0.5 A/g and 80.1% capacitance retention after 10,000 cycles. The assembled Mn_3O_4/rGO(+)//AC(−) ASC delivered 36.76 Wh/kg energy density with 93.5% capacitance retention after 5000 cycles. Oxygen deficient Co_3O_4 also exhibited enhanced performance[172] due to improved ionic and electronic conductivity, more electroactive sites, increased carrier concentration,[173] and also change in chemical properties owing to structural modification with-

out sacrificing structural stability.[174] Oxygen vacancy also generates a built-in electric field inside the material at the nano-level.[175] Zhang et al. used an effective $NaBH_4$-assisted cyanogen hydrolysis method for the synthesis of oxygen-deficient ultrathin Co_3O_4 nanosheets (NSs) on CNT surface and named it as Co_3O_4-NSs/CNT. The Co_3O_4-NSs/CNT nanocomposite with 5 wt.% CNT achieved a capacitance of 1280.4 F/g at a current density of 1 A/g and demonstrated an excellent cycling stability with 112.5% capacitance retention after 10,000 cycles. Moreover, the Co_3O_4-NSs/CNT//rGO ASC has delivered an energy density as high as 37.2 Wh/kg at a power density of 160.2 W/kg. Oxygen deficiency, the high surface area of ultrathin nanosheets, and synergy between conducting CNT and pseudocapacitive Co_3O_4 NSs result in enhanced electrochemical performance. In general, nanocomposite morphology provides enough adsorption/desorption sites for ions, better electronic conductivity, and fully exposed surface-active sites for electrochemical reactions.[176] Co_3O_4-NSs/CC treated with $NaBH_4$ delivers a capacitance of 920 F/g at a current density of 1 A/g.[177] Similarly, Hu et al. prepared Co_3O_4@$NiMoO_4$ core@shell hierarchical nanosheets arrays decorated on Ni-foam via facile two-step method followed by heat treatment.[178] Co_3O_4 nanosheets as "core" derived from MOF provide higher active surface area, high ionic conductivity, and abundant active chemical sites for further growth of $NiMoO_4$ nanosheets as "shell." The core@shell composite exhibited areal capacitance as high as 2.3 F/cm^2 at a current density of 1 mA/cm^2, and could retain 73% capacitance at a high current density of 20 mA/cm^2, which is better than pristine Co_3O_4. The charge storage mechanism in such core@shell structure could be summarized as follows.

$$Co_3O_4 + OH^- \leftrightarrow 3CoOOH + e^- \quad (17)$$

$$CoOOH + OH^- \leftrightarrow CoO_2 + H_2O + e^- \quad (18)$$

$$NiMoO_4 + OH^- \leftrightarrow NiMoO_4OH + e^- \quad (19)$$

When assembled with AC anode, the Co_3O_4@$NiMoO_4$//AC ASC delivered an energy density of 0.249 mWh/cm^2 at a power density of 1.6 mW/cm^2 along with 80.7% capacitance retention after 4000 GCD cycles at a current density of 10 mA/cm^2. To meet the demand for future electrochemical energy storage devices, rational fabrication of electrode materials with hierarchical structure and diverse components is the promising way forward. Stimulated by the idea, Yin et al., for the first time, used a network of hafnium carbide nanowires (HfCNWs) as a frame on carbon cloth to support porous $NiCo_2O_4$ nanosheets.[72] The hafnium carbide nanowires act as a conductive framework with high surface area and excellent physical/chemical stability. The core-shell $NiCo_2O_4$NSs@HfCNWs/CC displayed superior specific capacitance of 2102 F/g at 1 A/g current density with remarkable rate capability (capacitance retention of 85% at a high current density of 20 A/g) and an excellent cycling stability (capacitance retention of 98% after 5000 cycles at 10 A/g) due to the intrinsic structural merits. Further, the assembled $NiCo_2O_4$NSs@HfCNWs/CC//AC/CC ASC exhibited an outstanding energy density of 53 Wh/kg at a power density of 800 W/kg. Also, Zhao et al. have grown hierarchical $NiCo_2O_4$@$Ni_{4.5}Co_{4.5}S_8$ composite on nickel foam substrate using electrodeposition process followed by annealing.[71] The vertically grown $NiCo_2O_4$ nanosheet arrays act as a frame for the subsequent growth of $Ni_{4.5}Co_{4.5}S_8$ nanosheets that result in enhanced active sites for redox reactions. The electrode material displayed a high discharge capacity of 369 mAh/g. Similarly, heterostructure arrays of $NiMoO_4$ nanoflake on N-doped graphene,[179] and $CoWO_4$/$CoMn_2O_4$ nanoflake composite on nickel foam substrate[180] have shown excellent capacitance values of 1913 F/g at 1 A/g and 2259.6 F/g at 1 A/g, respectively. These studies put forward the idea of rational design and construction of 2D TMO-based hierarchical composites for high-performance energy storage devices.

4.2.3 | 1D TMO-based materials for supercapacitors

1D structures including nanowires, nanotubes, nanorods, nanofibres, and so on, are the most widely explored structures for supercapacitor electrodes.[181] The essence of using 1D nanostructures for electrodes in supercapacitors is that the linear channel in 1D provides direct path for fast movement of electrons, promoting transmission of electrons as compared to the electrodes made of nanoparticles where the scattering events give rise to a high internal resistance. Also, in the case of nanotubes, the added advantage comes from the hollow structure which serves as a buffer tank for the electrolyte leading to higher active contact sites due to the large accessible surface area than nanowires/nanofibres.[149] Thus, 1D electrode structures play a vital role in improving the overall performance of supercapacitors. The detailed charge storage mechanisms and electrochemical performance of 1D TMOs and their composites are explained in the following subsections.

4.2.4 | Pristine 1D TMOs

As discussed earlier, nanostructured materials that have a high surface area and low diffusion path length are

promising for supercapacitor electrodes. 1D nanostructures are advantageous because they provide efficient ways for the flow of electrons to the current collector, short ion-diffusion pathways for fast-ion migration, exhibit good reversibility, mechanical stability, and hence, good cycling stability.

Susanti et al. reported the synthesis of anhydrous RuO_2 nanorods encased in hydrous RuO_2 through chemical vapor deposition followed by electrodeposition.[182] A densely packed nanorod structure provides connecting backbone for easy electron migration during redox reactions, whereas abundant void spaces between nanorods facilitate infiltration of electrolytic ions. Thermally reduced nanorods encased in hydrous RuO_2 showed a capacitance of 520 F/g at 5 mV/s, which is higher than 260 F/g observed for the hydrous RuO_2 coated as-grown nanorods. Hu et al. demonstrated the synthesis of hydrous RuO_2 nanotubes using a membrane-template assisted route.[183] Nanotubes are electrodeposited inside the pores of AAO-coated graphite substrate followed by annealing at 200°C for 2 h. The total specific capacitance of hydrous RuO_2 nanotubes was enhanced from 740 to 1300 F/g when they were annealed in air. Moreover, the nanotubes have shown stable electrochemical behavior within a potential range of 0–0.8 V delivering energy and power densities of 7.5 Wh/kg and 4320 kW/kg, respectively, at an applied frequency of 4 kHz, and delivering the perfect performance for an advanced supercapacitor.

Pristine MnO_2 based 1D nanostructures have been widely investigated as supercapacitor electrodes. Yang et al. designed a low-cost solid-state ASC with MnO_2 nanowires as cathode material grown on flexible carbon cloth substrate using a facile hydrothermal method.[184] The densely packed MnO_2 nanowires have demonstrated an areal capacitance of 150 mF/cm^2 (equivalent to a specific capacitance of 197.4 F/g) at a discharge current density of 1 mA/cm^2 (equivalent to 1.4 A/g). Even at a high current density of 10 mA/cm^2, the nanowires could retain 73.6% of its initial capacitance, indicating excellent rate capability that can be owed to the outstanding conductivity of carbon cloth substrate. Maiti et al. reported a cocoon-like morphology with interconnected MnO_2 nanowires as a supercapacitor electrode.[185] Increased surface area, coexistence of micropores and mesopores, and enhanced electron transport in these interconnected nanowire networks result in a capacitance of 775 F/g at a scan rate of 2 mV/s in 3 M aqueous KOH solution and within a potential window of −1 to +1 V. The assembled SSC delivered an enormous energy density of 344 Wh/kg at a current density of 0.2 A/g in 3 M KOH solution, however, it could retain only 1.7 Wh/kg as the current density was increased to 5 A/g, along with delivering a power density of ∼6 kW/kg. During cycling analysis, pristine nanowires showed only 13% capacitance retention in 3 M KOH after 1000 cycles. However, the cycling performance measured in 3 M KOH + 0.1 M $K_4Fe(CN)_6$ electrolyte demonstrated more than 100% capacitance retention after 3000 cycles, which can be owed to the $Fe(CN)_6^{4-}/Fe(CN)_6^{3-}$ redox system that acts as electron buffer source preventing capacitance fade once the equilibrium is established. Xu et al. synthesized interconnected nanowires of MnO_2 with weed-like morphology grown on carbon cloth substrate by a hydrothermal method.[186] The unique structure has a large interface surface area, and allows rapid electrolyte diffusion through its hollow/open framework and fast electron transfer through the carbon skeleton. The electrode exhibited a high specific capacitance of 1174.3 F/g at the moderate current density of 2 A/g, excellent rate capability with ∼79% capacitance retention as the current density was increased to 40 A/g, and an excellent cycling stability with a negligible 0.1% decay in specific capacitances after 10,000 cycles. Further, Chou et al. reported electrochemical deposition of MnO_2 nanowires on carbon nanotube paper to be used as a free-standing, flexible supercapacitor electrode.[187] The as-synthesized electrode delivered a specific capacitance of 167.5 F/g at a current density of 77 mA/g within the potential window of 0.1–0.8 V, along with 60% capacitance retention even when the current density was increased by 10 times. The composite paper could retain more than 88% of initial capacitance after 3000 cycles measured at a current density of 770 mA/g in 0.1 M Na_2SO_4 solution.

In-situ growth of MnO_2 nanorod forest is reported by Shah et al.[188] The binder-free self-supported nanorod forest network achieved a capacitance of 961 F/g at 1 mA/cm^2 in 1 mol/L Na_2SO_4 electrolyte. The nanorod network also retained 92% of its initial capacitance after 5000 cycles measured at a current density of 5 mA/cm^2. Jayachandran et al. synthesized MnO_2 nanorods by simple hydrothermal method.[63] α-MnO_2 nanorods have tunnel-like structure, so it can store charge in tunnels by insertion and de-insertion of electrolyte ions, also by the adsorption of ions at the surface of active material. α-MnO_2 nanorods showed a capacitance of 570 F/g at a current density of 1 A/g in 1 M Na_2SO_4 + 0.5 M KOH electrolyte solution, and could retain 80 % of its initial capacitance as the current density increased to 10 A/g. Cycling stability was 80% after 10,000 cycles. Here, the Na^+ ions are mainly adsorbed at the surface because of their larger size, and the smaller sized K^+ ions could easily intercalate inside the tunnels followed by redox reactions. Yousefi et al. synthesized 1D α-MnO_2 nanorods using cathodic electrodeposition followed by heat treatment.[189] The nanorod exhibited BET surface area 93 m^2/g and a specific capacitance of 338 F/g at a scan rate of 10 mV/s.

As nanotubes offer additional surface area for redox reactions due to their hollow interior, tubular electrode

doi.org/10.1002/elsa.202100187

structure is far more suitable for high-performance storage system as compared to solid nanowires or nanorods. Xiao et al. demonstrated the growth of single crystalline α-MnO_2 nanotubes by hydrothermal method without the assistance of template, surfactant, or heat treatment methods.[190] As supercapacitor electrode, the nanotubes showed specific capacitance values of 220, 213, 196, 175, 152, and 136 F/g at scan rates of 5, 10, 20, 50, 100, and 200 mV/s, respectively, within a potential window of 0–0.9 V. Excellent pseudocapacitive properties are attributed to a nanotubular microstructure and a large tunnel cavity in the α-MnO_2 crystal structure. Further, tubular structure of MnO_2 is synthesized by Zhu et al. by simple hydrothermal method using carbon nanofibres as a sacrificial template.[191] The morphology was altered by changing the reaction time as well as the annealing process, polycrystalline MnO_2 nanotubes were formed with less reaction time whereas longer time favors hierarchical tubular MnO_2 nanostructures. Supercapacitor with tubular MnO_2 electrode demonstrated energy density of 21.1 Wh/kg at a power density of 13.33 kW/kg with long cycle life.

Apart from RuO_2 and MnO_2, significant research efforts have been expended to develop 1D nanostructures of iron, cobalt, and nickel-based oxides too. Lu et al. demonstrated the synthesis of oxygen-deficient hematite (α-Fe_2O_3) using a simple hydrothermal method followed by annealing in an inert atmosphere.[193] The process develops densely packed α-Fe_2O_3 nanorods on flexible carbon cloth substrate. Post synthetic annealing in inert atmosphere results in the formation of abundant oxygen vacancies into α-Fe_2O_3 matrix that further increases electronic conductivity of the nanorods. Benefitted from improved conductivity, the α-Fe_2O_3 nanords exhibited a high areal capacitance of 382.7 mF/cm^2 (equivalent to 89 F/g and 9.5 F/cm^3) at a current density of 0.5 mA/cm^2 with a good rate capability and excellent stability (95.2% capacitance loss after 10,000 cycles). When assembled with a MnO_2 positive electrode, the MnO_2//Fe_2O_3 ASC delivered a high energy density of 0.41 mWh/cm^3 at a current density of 0.5 mA/cm^2 and a high-power density of 0.1 W/cm^3 at a current density of 6 mA/cm^2. The long-term cycling stability of the ASC device was tested at a scan rate of 200 mV/s that showed a capacitance retention of 81.6% after 6000 cycles, revealing its good cycling stability. A similar hydrothermal method was also employed by Zhang et al. to prepare α-Fe_2O_3 nanorods on carbon cloth substrate.[112] The electrode showed an areal capacitance of 500 mF/cm^2 at 4 mA/cm^2. At high current densities of 6, 8, 10, and 12 mA/cm^2, the nanorods still possessed areal capacitances of 412, 300, 137, and 75 mF/cm^2, respectively. At 12 mA/cm^2, the α-Fe_2O_3 nanorods retained 92.1% of the initial capacitance after 3000 GCD cycles. Moreover, the NiO//α-Fe_2O_3 solid-state ASC device delivered a capacitance of 57.2 F/g (equivalent to ~229 mF/cm^2) at 4 mA/cm^2 within a working voltage of 1.25 V. The device achieved an energy density of 12.4 Wh/kg, a maximum power density of 951 W/kg, and 85% capacitance retention after 10,000 cycles. Yang et al. also synthesized α-Fe_2O_3 nanotubes on the carbon cloth substrate using a sacrificial template-assisted hydrolysis method.[194] Previously grown ZnO nanowires on carbon fabric were used as template that was then immersed in a solution containing Fe^{3+} ions for the hydrolysis method. During electrochemical analysis, the α-Fe_2O_3 nanotubes achieved an areal capacitance of 180.4 mF/cm^2 (equivalent to a specific capacitance of 257.8 F/g) at a discharge current density of 1 mA/cm^2 (equivalent to 1.4 A/g). Even at a high current density of 10 mA/cm^2, the nanowires could retain 66.5% of its initial capacitance, indicating good rate capability.

Ali et al. synthesized cobalt oxide nanowires and evaluated the electrochemical performance in 3 M KOH electrolyte, as shown in Figure 12.[192] The electrode has displayed a specific capacitance of 1140 F/g at 1 A/g and retained 93.3 % capacitance value after 5000 cycles. The assembled Co_3O_4 //AC ASC has shown a capacitance of 95 F/g at 1 A/g with a capacitance retention of 58.26 F/g at 15 A/g, which revealed a good rate capability. Further, the ASC have demonstrated a maximum energy-power densities of 18.20 Wh/kg and 11.80 kW/kg, respectively. The enhanced performance can be attributed to the fast diffusion of ions within the nanowire architecture, and rapid electron transfer at the Co_3O_4 nanowire electrode/electrolyte interfaces. Rakhi et al. have demonstrated remarkable pseudocapacitive performance of mesoporous Co_3O_4 nanowires grown hydrothermally on carbon paper substrate.[195] Here, substrate dependent self-organization of Co_3O_4 nanowires is reported. Brush-like morphology with Co_3O_4 nanowires completely surrounding the carbon fibers was observed when carbon fiber paper was used as substrate, whereas Co_3O_4 nanowires were found to self-organize in flower-like morphology on planar graphitized carbon paper substrate. In half-cell configuration, brush-like and flower-like morphologies exhibited specific capacitance values of 1525 and 1199 F/g, respectively, at a current density of 1 A/g. In SSC configuration, the Co_3O_4 nanowires with brush-like and flower-like morphologies achieved maximum energy/power densities of 55 Wh/kg/71 kW/kg and 55 Wh/kg/37 kW/kg, respectively. Both electrode designs exhibited excellent cycling stability by retaining ~91-94% of their maximum capacitance after 5000 cycles of continuous charge-discharge. Similarly, Kunhikrishnan et al. fabricated Co_3O_4 nanorods using PVA-assisted hydrothermal route and post calcination process.[196] It exhibited excellent electrochemical performance with a specific capacitance value of 1022 F/g value obtained from

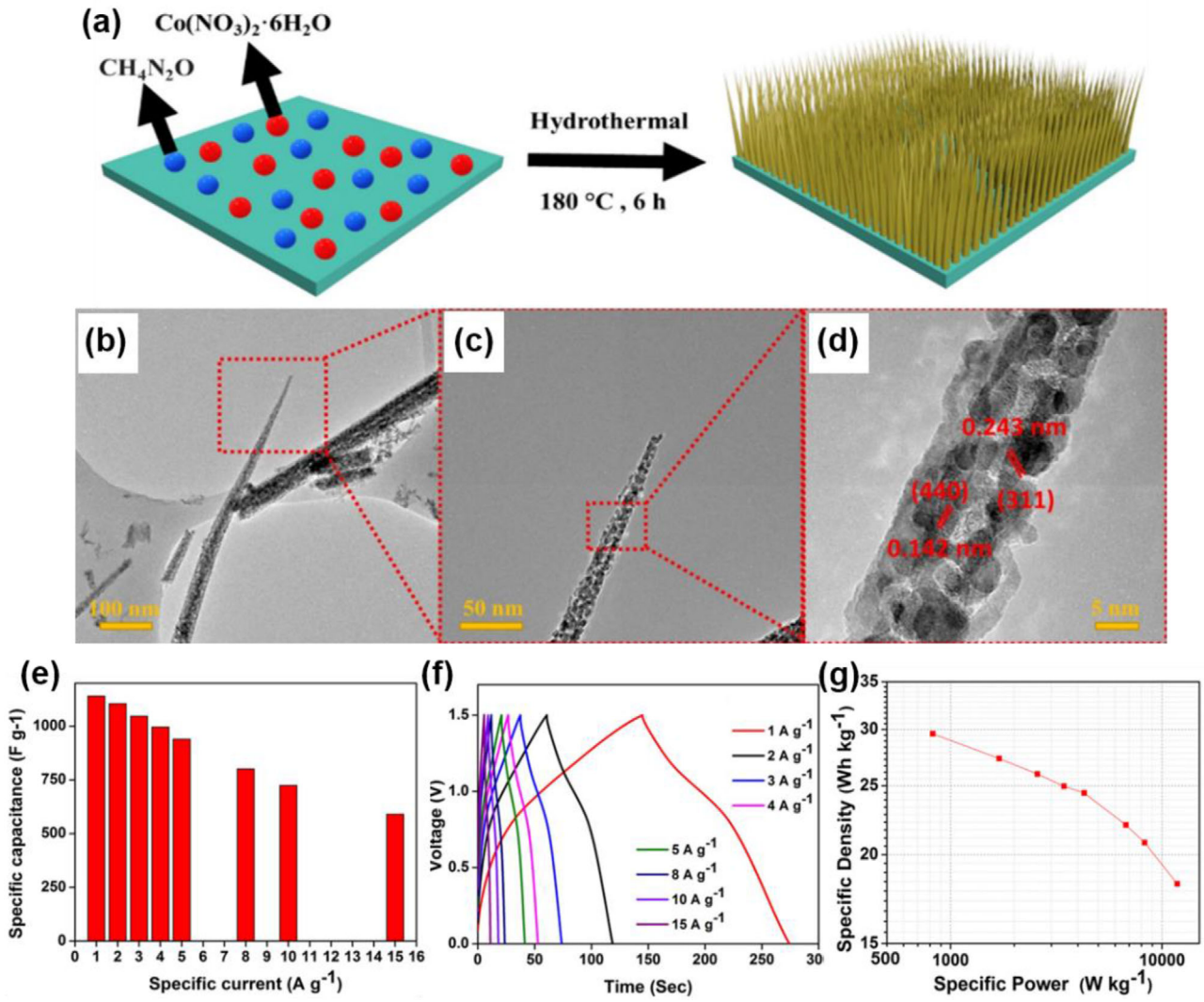

FIGURE 12 (a) Schematic representation of the synthesis of Co_3O_4 nanowires and their (b, c) TEM and (d) HRTEM images; (e) variation of specific capacitance with current density for Co_3O_4 nanowires, (f) GCD profiles at different current densities for Co_3O_4//AC ASC cell within the potential window of 0–1.5 V, and (g) Ragone plot for the Co_3O_4//AC ASC cell. (Reproduced with permission from Ref. [192], 2018, IOP)

the cyclic voltammograms at a scan rate of 5 mV/s and 88% capacitance retention after 2000 cycles measured at 100 mV/s scan rate. The electrode exhibited a capacitance of 954 F/g calculated using GCD profile at a current density of 1 A/g. Paravannoor et al. synthesized porous thin film NiO nanowires using cost-effective hydrothermal method.[60] The electrochemical studies revealed a high capacitance of 750 F/g and 88% capacitance retention after 1000 cycles. Also, Fe_2O_3 nanowire,[162] coaxial cable-like Mn_2O_3 nanofiber,[197] α-Fe_2O_3 nanorods,[112] and 1D Co_3O_4 nanostructures[198] have also been investigated and these structures have demonstrated good electrochemical performance.

Recently, Kumar et al. synthesized Zn-Ni-Co-O ($Zn_{1-x}Ni_xCo_2O_4$; $0.2 \leq x \leq 0.8$) nanorods using solvothermal method.[199] With the increase in nickel content, the size of the rods was found to decrease whereas capacity was enhanced from 266 C/g to 463 C/g at 3.12 A/g. The assembled hybrid aqueous SC exhibited energy density values of 26.4-7.0 Wh/kg at power densities ranging from 787 to 2035 W/kg. Bai et al. fabricated comb-like $NiCo_2O_4$ nanoneedles on nickel foam substrate by pulsed laser ablation method.[87] The prepared electrode displayed superior electrochemical performance due to the large surface area (261.4 m^2/g), porous structure, and conductive nature of scaffold. It exhibited a capacitance of 1650 F/g at 1 A/g current density and retained 91.78% capacitance after 12,000 cycles at 10 A/g. The assembled ASC displayed a capacitance of 126.9 F/g at 1 A/g current density with an energy density of 56.7 Wh/kg at 756 W/kg power density. Other than these, spinel cobaltite MCo_2O_4 (M = Ni, Co, and Mn),[200] $NiCoFeO_4$ nanorods,[201]

and $CoMn_2O_4$ nanofibres[81] have been synthesized and found to demonstrate good electrochemical performance suitable for next-generation supercapacitors.

4.2.5 | 1D TMO-based composites

To further enhance the electrochemical performance of 1D TMO-based electrode materials, various composites of nanostructured TMOs with other high surface areas, high electronically conductive materials have been designed and developed by researchers. For instance, Jeon et al. synthesized carbon nanofibers (CNFs) by electrospun method followed by the growth of RuO_2 nanorods over CNFs by precipitation and recrystallization method at varying temperatures.[202] Composites formed after heat treatment at 220°C have shown the optimal performance. RuO_2-CNFs composite exhibited maximum capacitance of 188 F/g at 1 mA/cm^2 current density in 1 M KOH electrolyte. Composite can retain 93% capacitance of the first cycle capacitance even after 3000 charge/discharge cycles at a current density of 1 mA/cm^2. Moreover, fabricated device delivered an energy density of 22 Wh/kg at power density of 400 W/kg, and it could retain an energy density of 15 Wh/kg when power density increased by 10 times. Such performance is attributed to the mesoporous structure with high surface area and a large number of active sites available in RuO_2-CNFs composite. Mesoporous network further provides better diffusion pathways for the electrolytic ions to move inside the material which enables the electrode to store a higher amount of charge. Due to the presence of diverse oxidation states of metal oxides and an excellent electronic conductivity of 2D MXene's, their composites demonstrate good electrochemical performance with high energy-power densities, good rate capability, and excellent cycling stability. Restacking issues with MXene layers and poor electrical conductivity of TMOs are key barriers to their efficient electrochemical performance when these materials are used separately. However, to address these challenges, unique manganese oxide/MXene (MnO_2/MXene) composite material was proposed by Mahmood et al.[203] In between MXene layers, 50 nm thick MnO_2 nanowires were grown to prevent restacking at the same time increasing the surface area of the composite electrode material. Unique control over the thickness of nanowires not only allows them to be adjusted inside the MXene layers but also provides a large surface area. In comparison to individual MXene and MnO_2, electrochemical investigations reveal that the MnO_2/MXene composite acts as an excellent electrode material for hybrid SCs. The maximum specific capacitances of MXene, MnO_2 nanowires, and MnO_2/MXene composite were found to be around 527.8, 337.5, and 611.5 F/g, respectively, with the MnO_2/MXene composite showing 96% of capacitance retention after 1000 cycles. Recently, Allado et al. fabricated binder-free bimetallic oxide composite.[204] δ-MnO_2/Co_3O_4 metal oxide composites were deposited on super-aligned electrospun carbon nanofibers (SA-ECNFs) by low-current slow electrodeposition method. δ-MnO_2/Co_3O_4@SA-ECNFs exhibited a specific capacitance of 728 F/g whereas δ-MnO_2@ SA-ECNFs could achieve only 622 F/g at a scan rate of 5 mV/s in 6 M KOH electrolyte. δ-MnO_2/Co_3O_4@SA-ECNFs delivered an energy density of 64.5 Wh/kg and a power density of 1276 W/kg measured at 2 A/g. Cycling test was performed at 2 A/g for 11000 cycles during which the device retained 71.8% of initial charge. Co_3O_4 and MnO_2 wrapped around carbon nanofibers provide more electron conduction pathways as well as enhanced surface area for improved performance. Sarkar et al. fabricated nanoheterostructured array of α-Fe_2O_3/MnO_2 nanowires via electrodeposition followed by wet chemical deposition methods.[68] The idea was to make core-shell nanowire electrode in which the MnO_2 "shell" stores charge through redox reactions while the higher conductive α-Fe_2O_3 "core" would transfer electrons to the current collector. The α-Fe_2O_3/MnO_2 heterostructure electrode displayed an excellent specific capacitance value of 838 F/g at 2 mV/s scan rate in 1 M KOH electrolyte. Also, it exhibited an energy density of 17 Wh/kg with 30.6 kW/kg power density at 50 A/g current density and an excellent cycling stability with only 1.5% capacitance fading after 1000 cycles. The outstanding electrochemical performance is due to the unique geometry of 1D heterostructure with a high surface area that facilitates fast redox reactions and easy diffusion of ions enabled by porous surfaces. To augment the idea further, α-Fe_2O_3/MnO_x core-shell nanorod electrode was also fabricated on carbon cloth substrate as shown in Figure 13.[205] The α-Fe_2O_3/MnO_x core-shell nanorod electrode exhibited an areal capacitance of ~217.8 mF/cm^2 (equivalent to a specific capacitance of 322.6 F/g) at a scan rate of 10 mV/s which is much higher than 176 mF/cm^2 (equivalent to specific capacitance of 251.4 F/g) obtained with the MnO_x electrode at similar scan rate. Moreover, the assembled α-Fe_2O_3/C//α-Fe_2O_3/MnO_x core-shell nanorod ASC demonstrated a volumetric capacitance of ~1.28 F/cm^3 at a scan rate of 10 mV/s with nearly 78% capacitance retention at the scan rate of 400 mV/s within a potential window of 0–2 V in 1 M Na_2SO_4. The ASC also delivered energy and power density values of ~0.64 mWh/cm^3 and 155 mW/cm^3, respectively.

Similarly, Lu et al. reported H-TiO_2@MnO_2 core@shell nanowires as supercapacitive electrode to avail the higher electronic conductivity of H-TiO_2 nanowires.[206] The H-TiO_2@MnO_2 nanowires delivered the highest specific capacitance of 449.6 F/g at the scan rate of 10 mV/s, which

Review
doi.org/10.1002/elsa.202100187
Chemistry Europe
European Chemical Societies Publishing

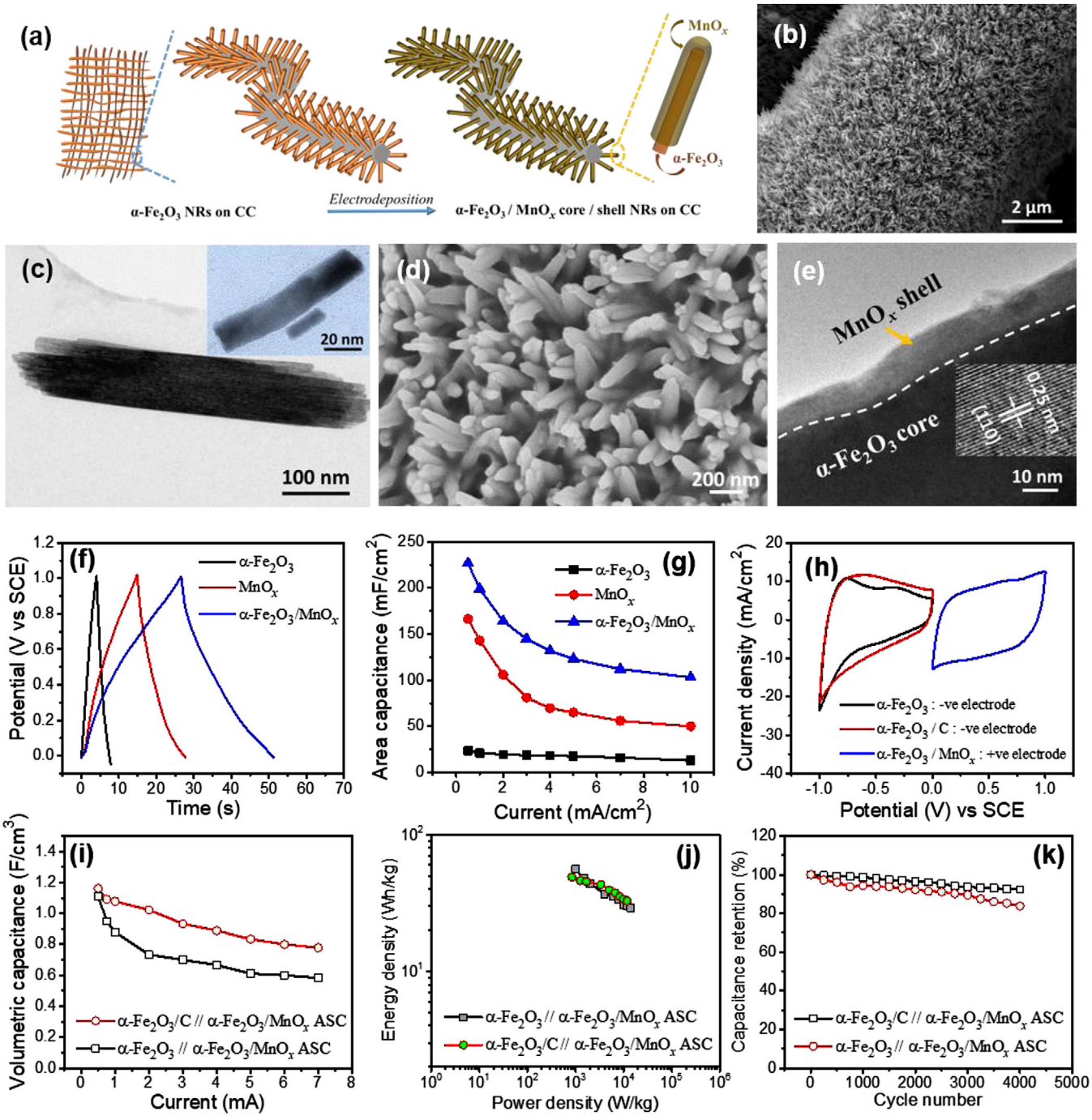

FIGURE 13 (a) Scheme of α-Fe_2O_3/MnO_x core-shell nanorod fabrication; (b) SEM and (c) TEM images of α-Fe_2O_3 nanorods; (d) SEM and (e) TEM images of α-Fe_2O_3/MnO_x core-shell nanorods; comparison of (f) GCD plots (at 5 mA/cm^2) measured in 1 M Na_2SO_4 electrolyte and (g) areal capacitances (at different currents) of α-Fe_2O_3, MnO_x, and α-Fe_2O_3/MnO_x; (h) comparison of CVs of positive and negative electrode materials for the assembled ASCs; comparison of (i) volumetric capacitances at different currents, (j) energy-power densities, and (k) cycling stabilities of the fabricated ASCs with α-Fe_2O_3/MnO_x as positive electrode material (Reproduced with permission from Ref. [205], 2017, IOP)

is higher than 325.8 and 359.7 F/g observed for the MnO_2 and TiO_2@MnO_2 electrodes, within a potential window of 0–0.8 V in 5 M LiCl electrolyte. When assembled in a device, the solid-state H-TiO_2@MnO_2//H-TiO_2@C ASC achieved a maximum volumetric and specific capacitance of 0.70 F/cm^3 and 139.6 F/g at 0.5 mA/cm^2 (~1.1 A/g) within an operating voltage window of 0–1.8 V, yielding an excellent stability with 91.2% retention of the initial capacitance after 5000 CV cycles measure at 100 mV/s. Zilong et al. synthesized MnO_2/ZnO core-shell nanorods which

doi.org/10.1002/elsa.202100187

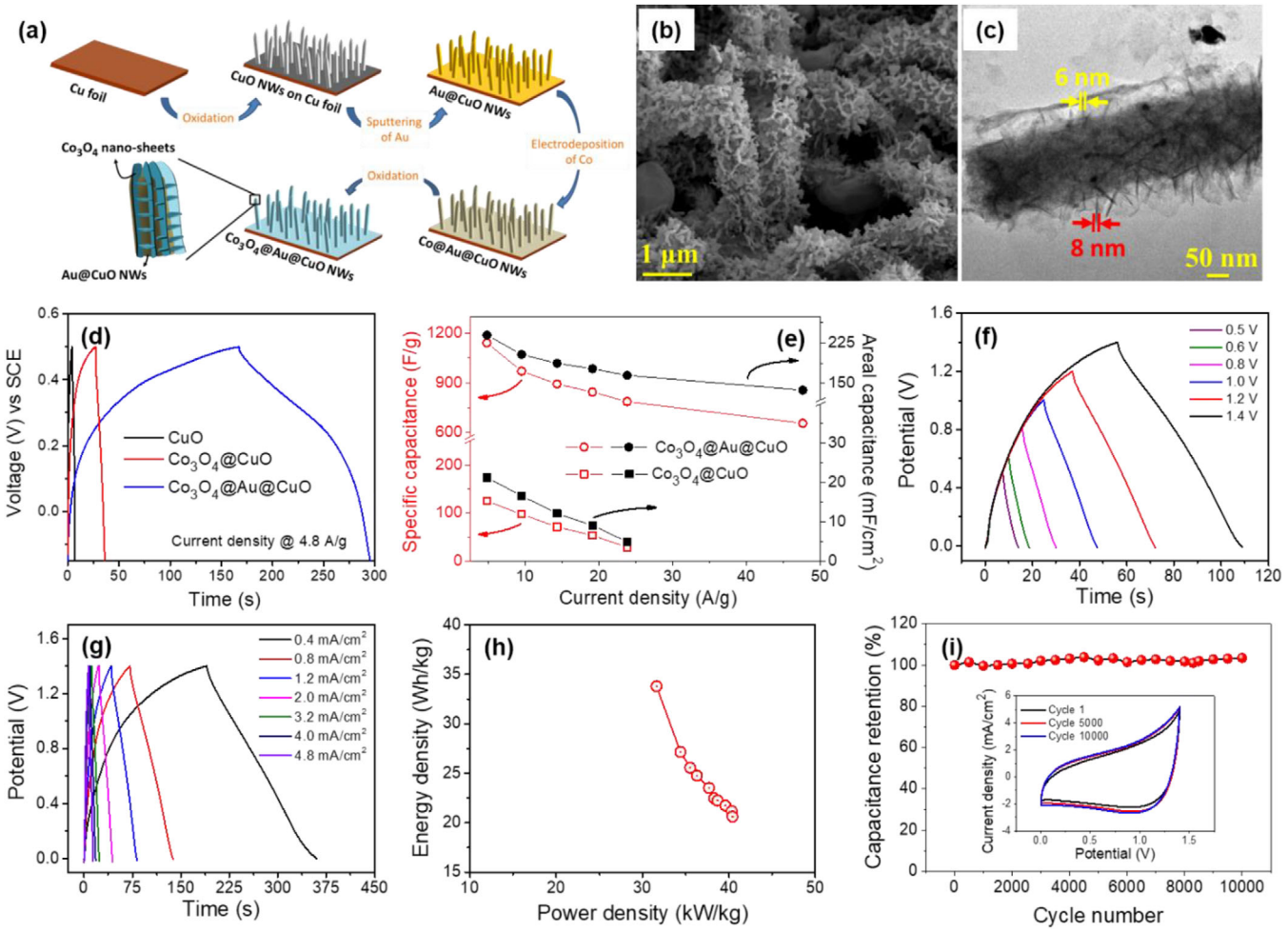

FIGURE 14 (a) Scheme of Co_3O_4@Au@CuO core-shell nanowires; (b) FESEM and (c) TEM images of Co_3O_4@Au@CuO core-shell nanostructures; comparison of (d) GCD profiles (at 4.8 A/g) and (e) specific capacitances at different current densities for different electrodes in half-cell configuration using 1 M Na_2SO_4 as electrolyte; for Co_3O_4@Au@CuO//α-Fe_2O_3 ASC: GCD profiles (f) within different potential windows and (g) at different current densities measured within the potential window of 0–1.4 V, (h) Ragone plot comparing energy-power densities of the ASC with other reported state-of-t, and (i) cyclic stability (inset to figure shows a few CV collected during cycling test) (Reproduced with permission from Ref. [208], 2017, RSC)

exhibited a specific capacitance of 230 mF/cm at a scan rate of 10 mV/s and 54.6% retention when the scan rate was increased to 200 mV/s.[207] The MnO_2/ZnO core-shell nanorods//r-GO ASC delivered volumetric energy and power density of 0.234 mWh/cm^3 and 0.133 W/cm^3 within a potential window of 0–1.8 V, and also demonstrated an excellent cycling stability with only 1.5% capacity fade after 5000 cycles. Singh et al. demonstrated a facile approach to design Co_3O_4@Au@CuO core-shell nanowire arrays for supercapacitors, as shown in Figure 14.[208] Ultra-thin interconnected nano-sheets of Co_3O_4 were deposited over Au@CuO nanowires, formed via Au sputtering on CuO nanowires directly grown on Cu foil. The unique structure provides abundant surface area for redox reactions together with the Au interlayer serving as the current accumulator as exhibited by enhanced capacitance and rate capability of Co_3O_4@Au@CuO as compared to Co_3O_4@CuO. Moreover, the α-Fe_2O_3// Co_3O_4@Au@CuO ASC exhibited an impressive volumetric energy density of 0.23 mWh/cm^3 (equivalent to 33.8 Wh/kg) with a high-power density of 270 mW/cm^3 (equivalent to 40.4 kW/kg) and a remarkable capacitance retention of ~100% over 10,000 CV cycles.

Binary TMOs are preferred over single TMOs due to various reasons like, binary TMO has more available oxidation states, two metal ions gave enhanced electronic conductivity and rate capability,[209,210] better cycling stability, and charge storage capability.[211] Morphology of active material decides its performance toward charge storage. Various morphologies of binary TMOs have been used for energy storage applications like nanoflowers, nanostructures, nanofibers, and so on.[82] Nanofibers have a 1D structure that provides a more accessible electrolyte/electrode contact area, creates more electron path-

doi.org/10.1002/elsa.202100187

ways and decreases diffusion path length, gives better ion conduction, cycling, and mechanical stability.[82,212–214] Recently, binary composite of Fe_2O_3@Na_2WO_4 is synthesized to enhance capacitance, rate capability, and cycling performance.[215] α-Fe_2O_3@Na_2WO_4 nanofiber was synthesized by a single-step coaxial syringe electrospinning of PVP-Na_2WO_4 and PVP-$Fe(NO_3)_3$ followed by calcination. Fe_2O_3@Na_2WO_4 nanocomposite exhibited a capacitance of 265.54 F/g at a current density of 6 mA/g. Calculations have revealed that the composite can store 75.6% of its total charge through capacitive processes, the rest is stored through ion diffusion mechanism. Symmetric coin cell (SCC) provided a potential window of 0–1.6 V with a capacitance of 160 F/g in 3 M Na_2SO_4 electrolyte. The SCC could deliver an energy density of 50 Wh/kg at a power density of 514.28 W/kg with 93% cycling stability after 200 charge–discharge cycles.[215]

TMO composites with conducting polymers facilitate electron conduction and enhancement of overall performance. Recently, Wang synthesized Fe_2O_3 nanotubes covered in conducting polypyrrole (Ppy) polymer on CC by a combination of sacrificial template followed by electrodeposition method.[73] Fe_2O_3 nanotubes@Ppy/CC could store 237 mF/cm^2 capacitance at 1 mA/cm^2 current density in 1 M Na_2SO_4 electrolyte, and cycling stability was 80% after 10,000 cycles measured at a current density of 10 mA/cm^2. Morphology of composite allowed more electrolyte ion storage at the Fe_2O_3-Ppy interface that further leads to enhanced stability, increased ionic conductivity, and higher capacitance values. The Fe_2O_3 nanotubes@Ppy/CC//MnO_2 ASC delivered an energy density of 24.2 Wh/kg at a power density of 408.2 W/kg within 0–2 V potential window. Ppy decorated on Fe_2O_3 nanotubes increased active material stability. Structural stability and ion transport is enhanced because Ppy works as a physical buffer that is able to absorb volume change effects in Fe_2O_3 nanotubes during charge/discharge cycles.[216,217] Similarly, α-Fe_2O_3@ polyaniline (PANI) core-shell nanowire arrays were synthesized by Lu et al. by a simple and cost-effective electrodeposition method that showed improved capacitance and rate performance.[218] α-Fe_2O_3@PANI electrode delivered a maximum capacitance of 103 mF/cm^2, which is twice of that obtained for pure α-Fe_2O_3 (33.93 mF/cm^2). The improvement of capacitance can be attributed to the coating of PANI, which is highly conductive and thus enhances the electrical conductivity of the overall electrode. After 2500 CV cycles at 100 mV/s, the capacitance retention is 100 % for α-Fe_2O_3@PANI, whereas it was ~93% for pure α-Fe_2O_3. The α-Fe_2O_3@PANI//PANI nanorods ASC device has delivered a volumetric capacitance of 2.02 F/cm^3 at 5 mV/s within a potential window of 0–1.5 V, a maximum energy density of 0.35 mWh/cm^3 at a power density of 120.51 mW/cm^3, and an excellent (~95.8%) cycling stability after 10,000 CV cycles. Yang et al. developed an electrically and ionically conducting framework consisting of α-Fe_2O_3 nanorods, multi-walled carbon nanotubes (CNTs), and PANI hydrogel for supercapacitor electrode.[219] The electrode delivered a high areal capacitance of 2434.7 mF/cm^2 and a capacitance retention of 96.3% after 10,000 cycles. The 1D hydrogenated Ni/NiO core-shell nanoheterostructured array was synthesized by Singh et al.,[70] first the Ni nanowires are grown via template-assisted electrochemical deposition that was followed by oxidation at high temperature and subsequent hydrogenation of NiO thin layer deposited over Ni wires. 1D Ni/NiO core-shell nanoheterostructured array displayed 717 F/g specific capacitance value at a scan rate of 2 mV/s, that was increased to 1635 F/g after hydrogenation. Also, it exhibited good rate capability, and good cycling stability with 57% capacitance retention after 1200 cycles. Enhanced performance is due to the hydroxyl groups present on NiO surface that leads to the improved electrochemical activity. Similar nanoheterostructures including TiO_2/$BiFeO_3$ nanoheterostructure,[220] NiO@Co_3O_4 nanotubes,[221] CeO_2 nanoparticle modified porous MnO_2 nanorods,[222] 1D Co-Ni/Co_3O_4-NiO core/shell nano-heterostructures,[223] ZnO/α-Fe_2O_3 core shell nanorods,[224] WO_3/MnO_2 core-shell nanorods,[225] Co_3O_4-MnO_2-NiO ternary hybrid 1D nanotube array,[226] and so on, have been explored as electrode materials for supercapacitor applications and these materials have displayed intriguing electrochemical performance.

Since the design and fabrication of multi-component electrode materials result in enhanced performance as supercapacitors, Jayasubramaniyan et al. synthesized $CuCo_2O_4$/rGO composite via microwave hydrothermal method.[227] The prepared material displayed a specific capacity of 677 C/g at a current density of 1 A/g and 97.4% capacitance retention after 2000 GCD cycles at 10 A/g. Excellent performance can be attributed to the porosity of $CuCo_2O_4$ which provides more redox-active sites and promotes deep penetration of electrolyte ions inside the electrode material. Moreover, the conductive network for the facile movement of electrons during cycling is due to the incorporated rGO. Similarly, Xu et al. fabricated $CuCo_2O_4$ nanowire arrays wrapped in metal oxides nanosheets (NiO, Co_3O_4, and MnO_2).[228] Among these composites, electrodes of $CuCo_2O_4$@NiO displayed the best electrochemical behavior with an areal capacitance of 2.3 F/cm^2 at 2 mA/cm^2. The assembled ASC exhibited a capacitance of 124.6 F/g at 1 A/g with an energy density of 38.9 Wh/kg at a power density of 750 W/kg. A capacitance retention of 81.3% was also achieved after 6000 cycles. Similarly, rGO/$NiCo_2O_4$ heterostructure,[229] $FeCo_2O_4$/PANI,[230] and $CuCo_2O_4$@Ni-Co-S core-shell arrays[231] have dis-

played an areal capacitance of 4.37 F/cm^2 at 2 mA/cm^2, the specific capacity of 940 C/g at 1 A/g, and areal capacitance of 12.10 F/cm^2 at 20 mA/cm^2, respectively. These studies highlight their potential for application in future energy storage devices.

4.2.6 | 0D TMO-based materials

Apart from 3D, 2D, and 1D nanostructures of TMOs as well as their composites with promising electrochemical performance as supercapacitor electrodes, 0D materials such as quantum dots (QDs) also hold significant potential owing to their high specific surface area, good electrical conductivity, and good ion mobility as generated by nanoscale effects.[24] Therefore, 0D TMOs and their composites may be used to enhance the overall electrochemical performance of electrodes. In this regard, Siwatch et al. synthesized $NiCo_2O_4$ quantum dots (NCO-QDs) as supercapacitor electrode.[232] Firstly, nickel-cobalt oxide ($NiCo_2O_4$) flower like 3D nanostructures were prepared by hydrothermal route and then subsequent annealing at different temperatures. NCO-QDs were formed at the calcination temperature of 300°C. The NCO-QDs displayed a capacitance of 362 F/g at a current density of 0.5 A/g. The assembled NCO-QDs//rGO ASC demonstrated a capacitance of 81 F/g at a scan rate of 5 mV/s with 86% capacitance retention after 1000 cycles. The ASC delivered energy density and power density of 69.5 Wh/kg and 2.22 kW/kg at 1.5 A/g current density within the potential window of 2.5 V. Moreover, composites of metal oxides quantum dots are also widely explored for supercapacitor electrodes. Su et al. fabricated a composite of $MnFe_2O_4$ QDs and nitrogen-doped graphene (NG) by solvothermal method, in which $MnFe_2O_4$ QDs were uniformly sprinkled over the surface of NG.[67] The powdery $MnFe_2O_4$ QDs@NG worked in a negative potential window (−1 to 0 V) in an aqueous solution of KOH and exhibited capacitance of 517 F/g, which was increased further to 905 F/g when the potential window was extended to −1.2 V. Encapsulation of carbon on QDs leads to an improved rate capability with a capacitance retention of 150 F/g at 200 A/g as well as an outstanding cycling stability up to 65,000 cycles.

Wang et al. prepared electrode material that involves 3–6 nm sized CoO QDs decorated on 3D graphene hydrogels using solvothermal process.[66] The 3D CoO QDs/graphene hydrogels displayed specific capacitance values of 889.7 to 822 F/g at current densities of 2 to 50 A/g with 92.4% capacitance retention. The hybrid QDs/graphene hydrogel//pure graphene hydrogel ASC delivered energy density values of 28.7 and 23.0 Wh/kg at power densities of 1600 and 12000 W/kg with no capacitance loss even after 5000 cycles. Enhanced electrochemical performance is due to the rational designing of electrode material by taking advantage of the high surface area of nanosized QDs, better electronic conductivity of graphene, and overall 3D microstructures. Xia et al. reported the electrochemical performance of Fe_2O_3 QD decorated functionalized graphene sheets (FGS).[234] The Fe_2O_3 QDs/FGS composites demonstrated a large specific capacitance of 347 F/g at 10 mV/s within a potential window between −1 and 0 V (versus Ag/AgCl) in 1 M Na_2SO_4 electrolyte. When coupled with MnO_2/FGS cathode, the Fe_2O_3QDs/FGS//MnO_2/FGS ASC delivered a capacitance of 73.2 F/g at 10 mV/s within 0–2 V voltage window. Noticeably, the ASC could deliver an energy density of 50.7 Wh/kg at a power density of 100 W/kg along with 95% capacitance retention after 5000 GCD cycles at a current density of 0.5 A/g. Similarly, Yang et al. developed Fe_2O_3 quantum dots (Fe_2O_3-QDs) and G-Fe_2O_3-QDs (G stands for graphene).[235] The composite electrode demonstrated capacitance of 1216 C/g (1105 F/g) at 2 A/g, which is far higher than that of pure Fe_2O_3-QDs (314 C/g), along with 55.4% capacitance retention at 50 A/g. The assembled G-$NiMoO_4$//G-Fe_2O_3-QDs ASC delivered a superior energy density of 130 Wh/kg, which is maintained to 56 Wh/kg even at a power density of 33.6 kW/kg. It possessed excellent cycling stability with 113% capacitance retention after 40,000 cycles. Liu et al. developed an advanced electrode material incorporating Nb_2O_5 QDs in nitrogen-doped porous carbon derived from ZIF-8 dodecahedrons (NQD-NC)[236] and assembled NQD-NC//AC HIC with organic electrolyte. The HIC delivered an energy density of 76.9 Wh/kg and a power density of 11250 W/kg with 85% capacity retention at 5 A/g after 4500 cycles within the potential window of 0.5-3.0 V. Y. Zhang et al. prepared two different materials, ZnO QDs/carbon/CNTs and porous N-doped carbon/CNTs from a single ZIF-8/CNTs template as illustrated in Figure 15.[233] The ZnO QDs/carbon/CNTs and porous N-doped carbon/CNTs displayed specific capacitances of 185 F/g at 0.5 A/g and 250 F/g at 1 A/g, respectively. The assembled ZnO QDs/carbon/CNTs//N-doped carbon/CNTs ASC worked within the potential window of 0–1.7 V and delivered an energy density of 23.6 Wh/kg with a power density of 16.9 kW/kg. Lian et al. prepared anode material for lithium-ion capacitor by coating Nb_2O_5 QDs of 4 nm in size over heteroatom-rich biomass-derived carbon.[237] The biomass-derived carbon enhances the electrical conductivity as well as stability of electrode by maintaining the stable solid-liquid interface. The composite electrode retained 82.1% capacity even after 3000 cycles. The results thus revealed the competitiveness of TMO-based QDs with other nanostructured TMOs in supercapacitor applications, and may therefore facilitate the progress of QD-based electrodes for next-generation electrochemical energy storage applications.

Review
doi.org/10.1002/elsa.202100187
Chemistry Europe
European Chemical Societies Publishing

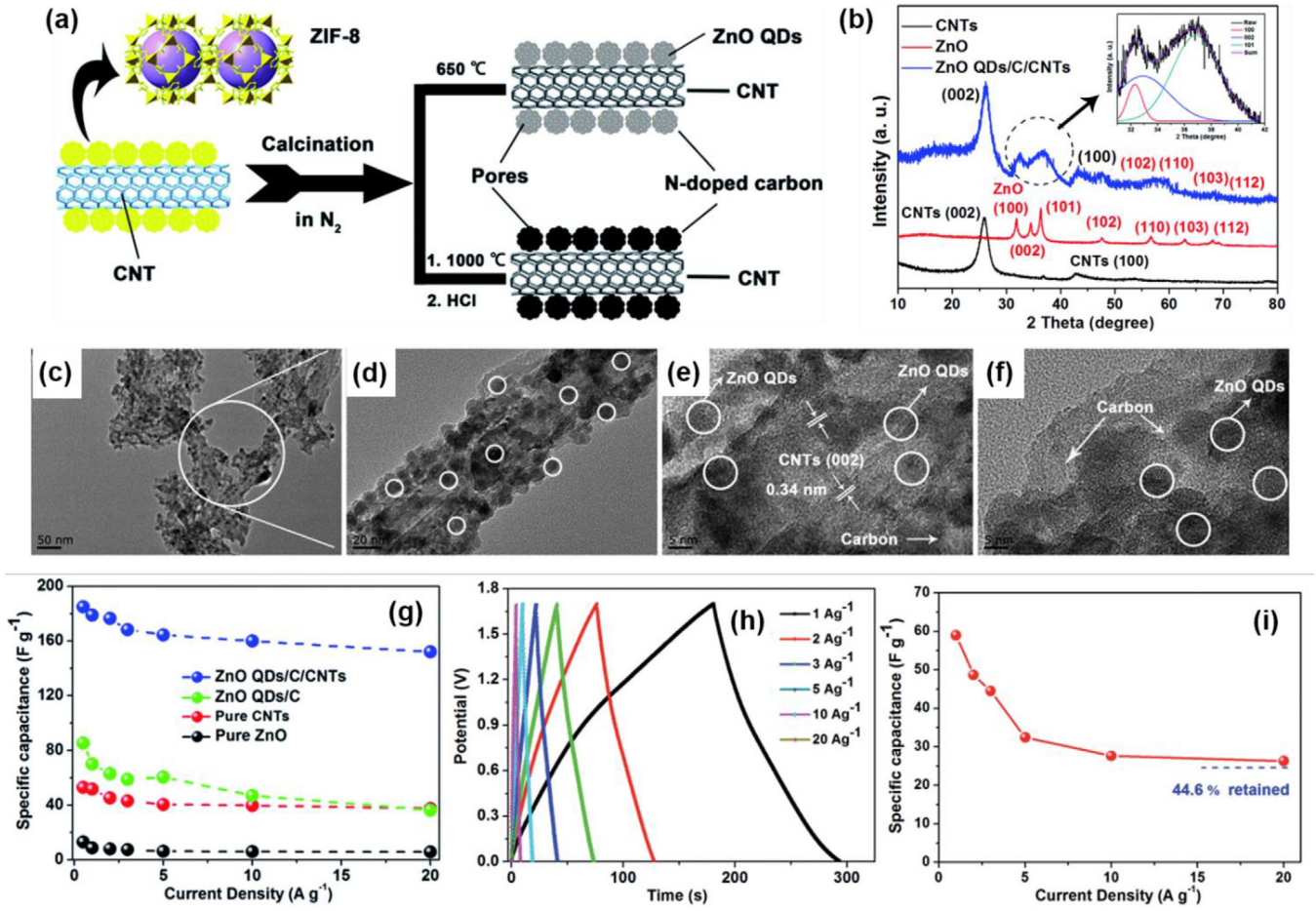

FIGURE 15 (a) Schematic illustration of the synthesis process of ZnO QDs/carbon/CNTs and N-doped carbon-CNTs; (b) XRD, (c, d) TEM, (e, f) HRTEM images of ZnO QDs/carbon/CNTs; (g) specific capacitances versus current for different electrode materials measured in half-cell configuration; (h) GCD curves at different current densities, and (i) corresponding specific capacitances for QDs/carbon/CNTs//N-doped carbon-CNTs ASC cell with a working potential of 0–1.7 V in PVA-$NaNO_3$ gel polymer electrolyte (Reproduced with permission from Ref. [233], 2013, RSC)

5 | SUMMARY AND PROGNOSIS

Pseudocapacitive materials are interesting because of their redox-based charge storage mechanism providing higher energy density as compared to EDLCs, fast power delivery capability, however, suffer from poor rate capability and cycling stability issues. The main motive in this direction is to comprehensively enhance the performance of pseudocapacitors in terms of capacitance, energy-power density, rate capability, and cycling stability. The key to achieve these goals is by designing nanostructured electrode materials which could significantly enhance the capacitance values by providing high specific surface area and provide high-rate capability by minimizing diffusion path length for fast movement of electrolytic ions. Accordingly, the review begins with a brief description of the charge storage mechanism in pseudocapacitors and the importance of designing nanostructured electrodes of pseudocapacitive materials for realizing high-performance supercapacitors. Next, we focused our attention on TMOs as potential pseudocapacitive materials because of their multiple advantageous traits including high theoretical specific capacitance, good energy density, low cost, etc., and also highlighted the challenges associated with TMOs like, low electronic conductivity, poor rate capability, low power density, and cyclability issues. This further signifies the importance of nanostructured electrode design as well as the necessity of fabricating composites of TMOs with highly conductive and electrochemically active materials. Subsequently, we summarize different well-established synthesis strategies used for the synthesis of various nanostructures of pristine TMOs and their composites having dimensions including 3D, 2D, 1D, and 0D (QDs). Next, the electrochemical performance of such pristine and hybrid nanostructured electrodes is compared and analyzed comprehensively both in three-electrode (half-cell) and two-electrode (full-cell) configurations, as summarized in Table 1. Emphasis is given to the observed specific capacitance values, energy

TABLE 1 Summary of the electrochemical performances reported in some key literatures on pristine TMOs and their composites for supercapacitor applications

			Half-Cell Measurements			Full-Cell Measurements				
Sl. No.	Electrode material	Synthesis Methods	Electrolyte	Capacitance	Full-Cell (+)//(−)	Electrolyte	Capacitance	Energy Density @ Power Density	Cycle stability	Ref
1	3D-MnO_2 film network	Electro-deposition	0.1 M $Mn(CH_3COO)_2$ + 0.1 M Na_2SO_4	2790 mF/cm^2 at 2 mA/cm^2	MnO_2//AC	1 M Na_2SO_4	67 F/g at 2.5 mA/cm^2	37.22 Wh/Kg at 178 W/kg	80% after 1000 cycles	[69]
2	3D-β-MnO_2 nanospheres	Chemical bath deposition	1 M Na_2SO_4	994 F/g at 5 mV/s	β-MnO_2//O-SnS	PVA-$LiClO_4$	122 F/g at 5 mV/s	29.8 Wh/Kg at 1.25 kW/kg	95.3% after 5000	[74]
3	3D-Fe_2O_3 nanoparticles	Hydrothermal processes	1 M $LiNO_3$	1472 mF/cm^2 at 2 mA/cm^2	$Mn(OH)_2$//Fe_2O_3	1 M $LiNO_3$	698.3 mF/cm at 1 mA/cm^2	5.12 mWh/cm^3 at 14.24 mW/cm^3	97.1% after 8000 cycles	[59]
4	3D-NiO nanostructure	Hydrothermal processes	1 M KOH	1.33 F/cm^2 at 4 mA/cm^2	NiO//α-Fe_2O_3	PVA/KOH	57.2 F/g (228.8 mF/cm^2) at 4 mA/cm^2	12.4 Wh/kg at 312 W/kg	85% after 10000 cycles	[112]
5	3D-NiO nanoparticles	MOF-based calcination process	2 M KOH	1863 F/g at 0.5 A/g	NiO//AC	2 M KOH	108 F/g at 0.5 A/g	38.4 Wh/Kg at 400 W/kg	82% after 5000 cycles	[113]
6	3D-V_2O_5 network	Hydrothermal process	0.5 M K_2SO_4	1098 F/g at 5 mV/s	V_2O_5//V_2O_5	LiCl/PVA gel	135.91 F/g at 5 A/g	48.32 Wh/kg at 0.49 kW/kg	92% after 10000 cycles	[114]
7	3D-Mn_2O_3 nanospheres	Hydrothermal process	1 M $LiNO_3$	345 F/g at 0.2 A/g	MnO_3//rGO	PVA-$LiNO_3$ gel	147 F/g at 0.2 A/g	46 Wh/Kg at 247 W/Kg	95% after 5000 cycles	[115]
8	3D hierarchical RuO_2	Hydrothermal process	1 M KOH	1342 F/g at 5 mV/s	RuO_2//AC	1 M KOH	79 F/g at 0.2 A/g	13 Wh/Kg at 110 W/kg	94% after 4000 cycles	[116]
9	3D Hierarchical $CuCo_2O_4$ nanourchin	Hydrothermal process	3 M KOH	1569.9 F/g at 0.6 A/g	$CuCo_2O_4$ // AC	3 M KOH	87.8 F/g at 0.85 A/g	23.9 Wh/Kg at 593.2 W/kg	91.5% after 2000 cycles	[62]
10	3D-$NiMn_2O_4$ nanoparticles	Sol-gel process	1 M Na_2SO_4	875 F/g at 2.0 mV/s	$NiMn_2O_4$//AC	1 M Na^2SO_4	166.7 F/g at 1 A/g	75 Wh/kg at 2250.9 W/kg	97.6% after 2000 cycles	[79]
11	3D-V-MnO_2	Hydrothermal process	1 M Li_2SO_4	414 F/g at 5 mV/s	V-MnO_2// $Ti_3C_2T_x$	1 M Li_2SO_4	76 F/g at 5 mV/s	36 Wh/kg at 3.2 kW/kg	88.6% after 10000 cycles	[124]
12	3D-MnO_2/CC	Hydrothermal process	1 M KOH	1092 mF/cm^2 at 3 mA/cm^2	MnO_2/CC//AC	1 M Na_2SO_4	67.8 F/g at 1 A/g	18.4 Wh/Kg at 699.5 W/kg	97.3% after 2000 cycles	[101]
13	3D-Mn_3O_4/CNT	Decomposition of Mn-hexacyanoferrate complex on CNT	1 M Na_2SO_4	453 F/g at 10 mV/s	Mn_3O_4/CNT// Fe_3O_4/CNT	1 M Na_2SO_4	135.2 F/g at 10 mV/s	31.4 Wh/kg at 10.3 kW/kg	100% after 15000 cycles	[125]
14	3D-Fe_2O_3/rGO	Hydrothermal process	4 M KOH	520 F/g at 1 A/g	$NiCo_2S_4$// Fe_2O_3/rGO	4 M KOH	130 F/g at 1 A/g	61.7 Wh/Kg at 22 kW/kg	91.5% after 1000 cycles	[130]

(Continues)

TABLE 1 (Continued)

Sl. No.	Electrode material	Synthesis Methods	Half-Cell Measurements			Full-Cell Measurements				Ref
			Electrolyte	Capacitance	Full-Cell (+)//(−)	Electrolyte	Capacitance	Energy Density @ Power Density	Cycle stability	
15	3D-Co_3O_4/$NiCo_2O_4$	MOF-based process	6 M KOH	770 F/g at 1 A/g	Co_3O_4/$NiCo_2O_4$//AC	6 M KOH	144 F/g at 1 A/g	38.8 Wh/Kg at 10 kW/kg	-	[139]
16	2D-MnO_2 nanosheets	Hydrothermal process	1 M Na_2SO_4	522 F/g at 1 A/g	MnO_2//AC	1 M Na_2SO_4	-	8.06 Wh/kg at 1000 W/kg	96.77% after 5000 cycles	[159]
17	2D-Co_3O_4 nanosheets	Hydrothermal process	3 M KOH	1196.5 mC/cm^2 at 5 mA/cm^2	Co_3O_4//AC	3 M KOH	145.5 F/g at 0.5 A/g	51.7 Wh/Kg at 1125 W/kg	91.8% after 15000 cycles	[163]
18	2D-$ZnCo_2O_4$ nanosheets	Hydrothermal approach	6 M KOH	2110.6 F/g at 1 A/g	$ZnCo_2O_4$//AC	6 M KOH	97.4 F/g at 0.2 A/g	34.6 Wh/Kg at 160 W/kg	93% after 3000 cycles	[165]
19	2D-Ag_2O-$HMnO_2$	Self-sacrificing template method	1 M Na_2SO_4	374 F/g at 1.5 mA/cm^2	Ag_2O-$HMnO_2$//PANF@α-FeOOH	Na_2SO_4/PVA	-	7.33 mWh/cm^3 at 1.93 W/cm^3	92.25% after 12000 cycles	[170]
20	2D-MnO_2/$CuCo_2O_4$	Hydrothermal process	1 M KOH	1458 F/g at 0.5 A/g	MnO_2/$CuCo_2O_4$//MnO_2/$CuCo_2O_4$	KOH/PVA	181.3 F/g at 0.5 A/g	64.1 Wh/kg at 1.5 kW/kg	80% after 5000 cycles	[171]
21	1D-Co_3O_4 nanowires	Hydrothermal process	3 M KOH	1140 F/g at 1 A/g	Co_3O_4//AC	3 M KOH	95 F/g at 1 A/g	18.20 Wh/kg at 11.80 kW/kg	93% after 5000 cycles	[192]
22	1D-$Zn_{1-x}Ni_xCo_2O_4$ nanorods	Solvothermal process	6 M KOH	266 C/g at 3.13 A/g	AC//$Zn_{1-x}Ni_xCo_2O_4$	6 M KOH	155 C/g at 0.78 A/g	26.4 W/kg at 787 W/kg	130% after 10000 cycles	[199]
23	1D-$NiCo_2O_4$ nanoneedles	Pulsed laser ablation method	3 M KOH	1650 F/g at 1 A/g	$NiCo_2O_4$//AC	3 M KOH	126.9 F/g at 1 A/g	45.6 Wh/Kg at 9120 W/kg	90.27% after 12000 cycles	[87]
24	1D-α-MnO_2/h-MoO_3	Chemical precipitation method	1 M Na_2SO_4	412 F/g at 1 A/g	α-MnO_2/h-MoO_3//α-MnO_2/h-MoO_3	1 M Na_2SO_4	89.5 F/g at 1 A/g	50 Wh/Kg at 1 kW/kg	95% after 10000 cycles	[209]
25	1D-Mn_2O_3@MnO_2	Electrospinning method	1 M Na_2SO_4	225.0 F/g at 0.2 A/g	Mn_2O_3 @ MnO_2//AC	1 M Na_2SO_4	60 F/g at 0.1 A/g	27.0 Wh/Kg at 9000 W/kg	84% after 5000 cycles	[213]
26	0D-$NiCo_2O_4$ QDs	Hydrothermal approach	1 M Na_2SO_4	362 F/g at 0.5 A/g	$NiCo_2O_4$// Graphene	1 M Na_2SO_4	81 F/g at 5 mVs	69.5 Wh/kg at 2.22 kW/kg	86% after 1000 cycles	[232]
27	0D-$MnFe_2O_4$ QDs/Graphene	Solvothermal approach	2 M KOH	517 F/g at 1 A/g	$MnFe_2O_4$/graphene// $MnFe_2O_4$/graphene	2 M KOH	110 F/g at 1 A/g	-	83% after 65000	[67]
28	0D-ZnO QD/Carbon/CNT	MOF based process	1 M Na_2SO_4	185 F/g at 0.5 A/g	ZnO QDs/carbon/CNTs//Carbon/CNTs	Na_2SO_4/PVA	59 F/g at 1 A/g	23.6 Wh/kg at 16.9 kW/kg	90% after 3000 cycles	[233]

(Continues)

TABLE 1 (Continued)

Sl. No.	Electrode material	Synthesis Methods	Half-Cell Measurements		Full-Cell Measurements					
			Electrolyte	Capacitance	Full-Cell (+)//(−)	Electrolyte	Capacitance	Energy Density @ Power Density	Cycle stability	Ref
29	0D-CoO QD/Graphene hydrogel	Solvothermal process	2 M KOH	889.7 F/g at 2 A/g	CoO/Graphene hydrogel//Graphene hydrogel	2 M KOH	81 F/g at 2 A/g	28.7 Wh/kg at 1600 W/kg	~100% after 5000 cycles	[66]
30	0D-Nb_2O_5 QDs/porous carbon	MOF based process	1.0 M $LiPF_6$ in EC/DMC	198 mAh/g at 0.2 A/g	Nb_2O_5 QDs/porous carbon//AC	1.0 M $LiPF_6$ in EC/DMC	-	76.9 Wh/kg at 450 W/kg	~85% after 4500	[236]

density, power density, rate capability, and cycling stability because these are important performance metrics for characterizing energy storage devices. Along with this, we have presented detailed discussions on how different traits of nanostructured design strategy and pseudocapacitive TMOs have synergized to offer much better performance necessary for next-generation supercapacitors. In brief, 3D microstructure with interconnected pores provides a larger surface area for electrolyte diffusion, shortened diffusion path lengths, and facile pathways for charge movement that results in good electrical contact. The diffusion of electrolyte ions throughout the electrode surface and accessibility of electrode surface to electrolyte ions are important in determining the performance of electrode, and the aforesaid advantages can be realized using 2D materials. The linear channel in 1D structures provides a direct path for the flow of charges, promoting the transmission of charges that leads to the enhanced rate capability for 1D electrodes. By reducing all the dimensions to nanoscale, specific surface area, ion mobility, and electronic conductivity can be further enhanced. Thus, using 0D materials such as QDs may be advantageous as electrode materials for high-performance supercapacitors. Further, composites of TMOs with other conducting materials like CNTs, graphene, Mxenes, polymers, and so on, and other pseudocapacitive materials for achieving enhanced performance are elaborated. Although tremendous progress has been made with TMO-based materials of different dimensions in the field of electrochemical energy storage in recent years, there are still some challenges that need to be addressed as summarized below.

1. Although researchers have widely explored various synthesis routes for pristine and hybrid TMOs, still the synthesis methods need to be optimized further before being considered for large-scale production of the aforementioned materials at low cost and in an environment friendly manner. Therefore, selection of electrode materials, design of optimized electrode structure, and optimization of various experimental parameters using state-of-the-art simulation techniques must be explored.
2. Though TMOs exhibit high theoretical capacitance values in three-electrode configuration, their performance in full-cell or two-electrode configuration is not satisfactory. This is because of the capacitance achieved with TMO-based nanostructures is far less than their theoretical values. It is necessary to find a suitable counter electrode to match the electrochemical performance (similar capacitance, working potential window, etc.) of TMO- based working electrodes to achieve maximum output from the ASC. Further understanding to effectively control the morphology and structure of TMO-

based electrode materials as well as to find out the suitable combinations of positive and negative electrodes is thus highly coveted.

3. Researchers have so far synthesized various TMO-based composite nanostructures by combining TMOs with other materials with complementary characteristics to improve their capacitive performance. For instance, hierarchical heterostructure composite is one of the promising electrode materials that enhances the redox-active sites as well as leads to improved cycling stability of the energy storage process. Nevertheless, a deep understanding of the synergistic mechanism is still unknown and comprehensive studies for exploring the structure-property correlation are highly desired for a better choice of materials for heterostructure formation. Besides, facile and green fabrication technologies must be explored as the existing technologies are still in the laboratory stage due to their complexity.
4. Structure-property correlation of TMO-based electrode materials through in-situ and in-operando spectroscopic studies is scanty because of the unavailability and complexity of required technologies. However, such studies are highly useful for a complete understanding of the charge storage mechanism in electrode materials by probing the changes at the electrode-electrolyte interface, and monitoring the charge transfer and changes in the coordination environment around metal sites during electrochemical redox reactions.
5. Theoretical simulations through DFT calculations could also help in understanding different traits of a particular electrode material, and in identifying an optimized structure of that material that would provide better electrochemical performance. Such studies are required for optimum usage of materials with high theoretical specific capacitances but having high cost due to scarcity and toxic nature.
6. To enhance the energy-power densities of supercapacitors, the idea of hybrid ion capacitors (HICs) has been introduced recently, which is the key to minimize the gap between high-energy batteries and high-power supercapacitors. HICs combine a battery-type anode material, a capacitor-type cathode material and an organic electrolyte for allowing a stable operational potential as high as 4 V. As the energy density varies with the square of the operating potential, HICs can provide significantly higher energy density than aqueous based supercapacitors. However, the progress in this direction is still in the primary stage, and charge storage mechanisms in such HICs are not clearly understood, and hence, a comprehensive understanding is required.

In the light of the foregoing and considering the ever-growing demand for high-performance supercapacitors for a variety of civil and military applications, cumulative efforts are required for developing state-of-the-art synthesis methods for supercapacitor materials, understanding intricate electrochemical mechanisms, designing optimized device configurations, and, finally, for their large-scale manufacture at low-cost.

ACKNOWLEDGMENTS

We gratefully acknowledge the efforts of the scientists cited in this review article. H.K.R. acknowledges Council of Scientific and Industrial Research (CSIR), Government of India, for the Research Fellowship (File no. 09/964(0032)/2020-EMR-I). D.S. acknowledges support from the Science and Engineering Research Board (SERB), Government of India, through the project SRG/2019/001211. Financial support from UKRI Global Challenge Research Fund project SUNRISE (EP/P032591/1), DST-MECSP, New Delhi, and Indian Institute of Science, Bengaluru, is gratefully acknowledged.

CONFLICT OF INTEREST

The authors declare no conflict of interest.

DATA AVAILABILITY STATEMENT

Not Applicable.

REFERENCES

1. Y. Shao, M. F. El-Kady, J. Sun, Y. Li, Q. Zhang, M. Zhu, H. Wang, B. Dunn, R. B. Kaner, *Chem. Rev.* **2018**, *118*, 9233.
2. A. Burke, T. Murphy, D. Goughtly, B. Vyas, T. Takamura, J. R. H., *Materials for Electrochemical Energy Storage and Conversion-Batteries, Capacitors and Fuel Cells*, vol. *393*, Pa, Pittsburgh: Materials Research Society **1995**, pp. 375.
3. A. Noori, M. F. El-Kady, M. S. Rahmanifar, R. B. Kaner, M. F. Mousavi, *Chem. Soc. Rev.* **2019**, *48*, 1272.
4. P. Simon, Y. Gogotsi, *Nat. Mater.* **2020**, *19*, 1151.
5. P. Simon, Y. Gogotsi, *Nat. Mater.* **2008**, *7*, 845.
6. G. Wang, L. Zhang, J. Zhang, *Chem. Soc. Rev.* **2012**, *41*, 797.
7. A. González, E. Goikolea, J. A. Barrena, R. Mysyk, *Renew. Sust. Energ. Rev.* **2016**, *58*, 1189.
8. A. Muzaffar, M. B. Ahamed, K. Deshmukh, J. Thirumalai, *Renew. Sust. Energ. Rev.* **2019**, *101*, 123.
9. D. Sarkar, D. Das, S. Das, A. Kumar, S. Patil, K. K. Nanda, D. D. Sarma, A. Shukla, *ACS Energy Lett.* **2019**, *4*, 1602.
10. A. Borenstein, O. Hanna, R. Attias, S. Luski, T. Brousse, D. Aurbach, *J. Mater. Chem. A* **2017**, *5*, 12653.
11. Y. Wang, L. Zhang, H. Hou, W. Xu, G. Duan, S. He, K. Liu, S. Jiang, *J. Mater. Sci.* **2021**, *56*, 173.
12. L. L. Zhang, X. S. Zhao, *Chem. Soc. Rev.* **2009**, *38*, 2520.
13. K. H. An, W. S. Kim, Y. S. Park, Y. C. Choi, S. M. Lee, D. C. Chung, D. J. Bae, S. C. Lim, Y. H. Lee, *Adv. Mater.* **2001**, *13*, 497.
14. Z. Yang, J. Tian, Z. Yin, C. Cui, W. Qian, F. Wei, *Carbon* **2019**, *141*, 467.

15. C. Liu, Z. Yu, D. Neff, A. Zhamu, B. Z. Jang, *Nano Lett.* **2010**, *10*, 4863.
16. Y. B. Tan, J. M. Lee, *J. Mater. Chem. A* **2013**, *1*, 14814.
17. Y. Wang, Z. Shi, Y. Huang, Y. Ma, C. Wang, M. Chen, Y. Chen, *J. Phys. Chem. C* **2009**, *113*, 13103.
18. Y. Gao, Y. S. Zhou, M. Qian, X. N. He, J. Redepenning, P. Goodman, H. M. Li, L. Jiang, Y. F. Lu, *Carbon* **2013**, *51*, 52.
19. D. Pech, M. Brunet, H. Durou, P. Huang, V. Mochalin, Y. Gogotsi, P.-L. Taberna, P. Simon, *Nat. Nanotechnol.* **2010**, *5*, 651.
20. M. E. Plonska-Brzezinska, L. Echegoyen, *J. Mater. Chem. A* **2013**, *1*, 13703.
21. C. Largeot, C. Portet, J. Chmiola, P.-L. Taberna, Y. Gogotsi, P. Simon, *J. Am. Chem. Soc.* **2008**, *130*, 2730.
22. S. Fleischmann, J. B. Mitchell, R. Wang, C. Zhan, D. Jiang, V. Presser, V. Augustyn, *Chem. Rev.* **2020**, *120*, 6738.
23. T. Wang, H. C. Chen, F. Yu, X. S. Zhao, H. Wang, *Energy Storage Mater.* **2019**, *16*, 545.
24. S. Kumar, G. Saeed, L. Zhu, K. N. Hui, N. H. Kim, J. H. Lee, *Chem. Eng. J.* **2021**, *403*, 126352.
25. D. Zhang, X. Zhang, Y. Chen, P. Yu, C. Wang, Y. Ma, *J. Power Sources* **2011**, *196*, 5990.
26. R. Liu, A. Zhou, X. Zhang, J. Mu, H. Che, Y. Wang, T. T. Wang, Z. Zhang, Z. Kou, *Chem. Eng. J.* **2021**, *412*, 128611.
27. B. De, S. Banerjee, K. Verma, T. Pal, P. Manna, K. Kar, *Handbook of Nanocomposite Supercapacitor Materials II Performance: Performance* (Ed.: K. Kar), Springer, **2020**, pp. 89–111.
28. B. E. Conway, *Electrochemical Supercapacitors: Scientific Fundamentals and Technological Applications*, Springer Science & Business Media, **2013**, pp. 259–297.
29. S. Trasatti, G. Buzzanca, *J. Electroanal. Chem. Interfacial Electrochem.* **1971**, *29*, A1-A5.
30. C. C. Hu, K. H. Chang, M. C. Lin, Y. T. Wu, *Nano Lett.* **2006**, *6*, 2690.
31. Q. Jia, S. Song, X. Wu, J. Cho, S. Foltyn, A. Findikoglu, J. Smith, *Appl. Phys. Lett.* **1996**, *68*, 1069.
32. I.-H. Kim, K.-B. Kim, *J. Electrochem. Soc.* **2006**, *153*, A383.
33. H. Lee, M. S. Cho, I. H. Kim, J. D. Nam, Y. Lee, *Synth. Met.* **2010**, *160*, 1055.
34. K. Sakiyama, S. Onishi, K. Ishihara, K. Orita, T. Kajiyama, N. Hosoda, T. Hara, *J. Electrochem. Soc.* **1993**, *140*, 834.
35. T. Hepel, F. H. Pollak, W. E. O'Grady, *J. Electrochem. Soc.* **1984**, *131*, 2094.
36. J. P. Zheng, T. R. Jow, Q. X. Jia, X. D. Wu, *J. Electrochem. Soc.* **1996**, *143*, 1068.
37. L. M. Doubova, S. Daolio, A. De Battisti, *J. Electroanal. Chem.* **2002**, *532*, 25.
38. H. Over, *Electrochim. Acta* **2013**, *93*, 314.
39. R. Fu, Z. Ma, J. P. Zheng, *J. Phys. Chem. B* **2002**, *106*, 3592.
40. D. R. Rolison, J. W. Long, J. C. Lytle, A. E. Fischer, C. P. Rhodes, T. M. McEvoy, M. E. Bourg, A. M. Lubers, *Chem. Soc. Rev.* **2009**, *38*, 226.
41. X. Liu, P. G. Pickup, *J. Power Sources* **2008**, *176*, 410.
42. J. W. Long, K. E. Swider, C. I. Merzbacher, D. R. Rolison, *Langmuir* **1999**, *15*, 780.
43. W. Deng, X. Ji, Q. Chen, C. E. Banks, *RSC Adv.* **2011**, *1*, 1171.
44. K. Chaitra, P. Sivaraman, R. T. Vinny, U. M. Bhatta, N. Nagaraju, N. Kathyayini, *J. Energy Chem.* **2016**, *25*, 627.
45. T. M. Dinh, A. Achour, S. Vizireanu, G. Dinescu, L. Nistor, K. Armstrong, D. Guay, D. Pech, *Nano Energy* **2014**, *10*, 288.
46. H. Kim, B. N. Popov, *J. Power Sources* **2002**, *104*, 52.
47. J. Li, X. Wang, Q. Huang, C. Dai, S. Gamboa, P. J. Sebastian, *J. Appl. Electrochem.* **2007**, *37*, 1129.
48. S. Oke, M. Yamamoto, K. Shinohara, H. Takikawa, H. Xiaojun, S. Itoh, T. Yamaura, K. Miura, K. Yoshikawa, T. Okawa, N. Aoyagi, *Chem. Eng. J.* **2009**, *146*, 434.
49. V. Panić, T. Vidaković, S. Gojković, A. Dekanski, S. Milonjić, B. Nikolić, *Electrochim. Acta* **2003**, *48*, 3805.
50. J. H. Park, O. O. Park, *J. Power Sources* **2002**, *109*, 121.
51. C. Zhang, T. Higgins, S. Park, S. O'brien, D. Long, J. Coleman, V. Nicolosi, *Nano Energy* **2016**, *28*, 495.
52. M. K. Song, S. Cheng, H. Chen, W. Qin, K. W. Nam, S. Xu, X. Q. Yang, A. Bongiorno, J. Lee, J. Bai, T. A. Tyson, J. Cho, M. Liu, *Nano Lett.* **2012**, *12*, 3483.
53. R. Wang, X. Yan, J. Lang, Z. Zheng, P. Zhang, *J. Mater. Chem. A* **2014**, *2*, 12724.
54. C. Yuan, X. Zhang, L. Su, B. Gao, L. Shen, *J. Mater. Chem.* **2009**, *19*, 5772.
55. M. Zhi, C. Xiang, J. Li, M. Li, N. Wu, *Nanoscale* **2013**, *5*, 72.
56. T. Lu, S. Dong, C. Zhang, L. Zhang, G. Cui, *Coord. Chem. Rev.* **2017**, *332*, 75.
57. J. Shi, B. Jiang, C. Li, F. Yan, D. Wang, C. Yang, J. Wan, *Mater. Chem. Phys.* **2020**, *245*, 122533.
58. D. Yan, Z. Guo, G. Zhu, Z. Yu, H. Xu, A. Yu, *J. Power Sources* **2012**, *199*, 409.
59. J. Li, S. Luo, B. Zhang, J. Lu, W. Liu, Q. Zeng, J. Wan, X. Han, C. Hu, *Nano Energy* **2021**, *79*, 105410.
60. A. Paravannoor, R. Ranjusha, A. M. Asha, R. Vani, S. Kalluri, K. R. V. Subramanian, N. Sivakumar, T. N. Kim, S. V. Nair, A. Balakrishnan, *Chem. Eng. J.* **2013**, *220*, 360.
61. A. Umar, S. D. Raut, A. A. Ibrahim, H. Algadi, H. Albargi, M. A. Alsaiari, M. S. Akhtar, M. Qamar, S. Baskoutas, *Electrochim. Acta* **2021**, *389*, 138661.
62. W. Liu, Y. Feng, L. Sun, Y. Zhang, G. Wang, L. Zhao, M. Meng, J. Li, K. Liu, *J. Alloys Compd.* **2018**, *756*, 68.
63. M. Jayachandran, A. Rose, T. Maiyalagan, N. Poongodi, T. Vijayakumar, *Electrochim. Acta* **2021**, *366*, 137412.
64. T. Wang, J. Liu, Y. Ma, S. Han, C. Gu, J. Lian, *Electrochim. Acta* **2021**, *392*, 138976.
65. M. Sethi, U. S. Shenoy, D. K. Bhat, *Physica B Condens. Matter* **2021**, *611*, 412959.
66. R. Wang, M. Han, Q. Zhao, Z. Ren, C. Xu, N. Hu, H. Ning, S. Song, J.-M. Lee, *Electrochim. Acta* **2017**, *243*, 152.
67. L. Su, S. Lei, L. Liu, L. Liu, Y. Zhang, S. Shi, X. Yan, *J. Mater. Chem. A* **2018**, *6*, 9997.
68. D. Sarkar, G. G. Khan, A. K. Singh, K. Mandal, *J. Phys. Chem. C* **2013**, *117*, 15523.
69. J. Yang, L. Lian, H. Ruan, F. Xie, M. Wei, *Electrochim. Acta* **2014**, *136*, 189.
70. A. K. Singh, D. Sarkar, G. G. Khan, K. Mandal, *J. Mater. Chem. A* **2013**, *1*, 12759.
71. N. Zhao, H. Fan, J. Ma, M. Zhang, C. Wang, H. Li, X. Jiang, X. Cao, *J. Power Sources* **2019**, *439*, 227097.
72. X. Yin, H. Li, Y. Fu, R. Yuan, J. Lu, *Chem. Eng. J.* **2020**, *392*, 124820.
73. Y. Wang, Z. Du, J. Xiao, W. Cen, S. Yuan, *Electrochim. Acta* **2021**, *386*, 138486.
74. A. M. Patil, V. C. Lokhande, U. M. Patil, P. A. Shinde, C. D. Lokhande, *ACS Sustainable Chem. Eng.* **2018**, *6*, 787.

75. Y. Tian, Z. Liu, R. Xue, L. Huang, *J. Alloys Compd.* **2016**, *671*, 312.
76. D. Sarkar, A. Shukla, D. D. Sarma, *ACS Energy Lett.* **2016**, *1*, 82.
77. K. Tian, J.-t. Wang, L. Xing, Z.-y. Li, B.-b. Kuang, Y.-a. Sun, *Solid State Ion.* **2021**, *371*, 115756.
78. P. Palmero, in *Encyclopedia of Materials: Technical Ceramics and Glasses* (Ed.: M. Pomeroy), Elsevier, Oxford **2021**, pp. 27–39.
79. A. Ray, A. Roy, M. Ghosh, J. Alberto Ramos-Ramón, S. Saha, U. Pal, S. K. Bhattacharya, S. Das, *Appl. Surf. Sci.* **2019**, *463*, 513.
80. S. Maitra, R. Mitra, T. K. Nath, *J. Alloys Compd.* **2021**, *858*, 157679.
81. J. Bhagwan, B. V. Krishna, J. S. Yu, *Int. J. Energy Res.* **2021**, *45*, 19413.
82. G. Zhang, X. Xiao, B. Li, P. Gu, H. Xue, H. Pang, *J. Mater. Chem. A* **2017**, *5*, 8155.
83. A. Zhang, R. Gao, L. Hu, X. Zang, R. Yang, S. Wang, S. Yao, Z. Yang, H. Hao, Y.-M. Yan, *Chem. Eng. J.* **2021**, *417*, 129186.
84. E. Elanthamilan, S. Rajkumar, J. P. Merlin, D. S. Jona, K. Monisha, B. C. Meena, *Electrochim. Acta* **2020**, *359*, 136953.
85. Z. Huang, S. Li, Z. Li, J. Li, G. Zhang, L. Cao, H. Liu, *J. Alloys Compd.* **2020**, *830*, 154637.
86. Y. Lu, Y. Liu, J. Mo, B. Deng, J. Wang, Y. Zhu, X. Xiao, G. Xu, *J. Alloys Compd.* **2021**, *853*, 157271.
87. R. Bai, X. Luo, D. Zhen, C. Ci, J. Zhang, D. Wu, M. Cao, Y. Liu, *Int. J. Hydrog. Energy* **2020**, *45*, 32343.
88. R. Samal, M. Kandasamy, B. Chakraborty, C. S. Rout, *Int. J. Hydrog. Energy* **2021**, *46*, 28028.
89. S. S. Raut, L. K. Bommineedi, S. Pande, B. R. Sankapal, *Synth. Met.* **2021**, *271*, 116629.
90. S. Park, D. Shin, T. Yeo, B. Seo, H. Hwang, J. Lee, W. Choi, *Chem. Eng. J.* **2020**, *384*, 123269.
91. M. J. Huang, W. H. Chen, C. Cheng, S. R. Chen, J. Y. Lin, C. R. Yang, *J. Alloys Compd.* **2021**, *869*, 159300.
92. Y. Huang, S. Bao, J. Lu, *J. Alloys Compd.* **2020**, *845*, 156192.
93. J. Noh, C.-M. Yoon, Y. K. Kim, J. Jang, *Carbon* **2017**, *116*, 470.
94. S. D. Raut, H. R. Mane, N. M. Shinde, D. Lee, S. F. Shaikh, K. H. Kim, H. J. Kim, A. M. Al-Enizi, R. S. Mane, *New J. Chem.* **2020**, *44*, 17864.
95. D. A. Kitchaev, S. T. Dacek, W. Sun, G. Ceder, *J. Am. Chem. Soc.* **2017**, *139*, 2672.
96. S. C. Hung, Y. R. Chou, C. D. Dong, K. C. Tsai, W. D. Yang, *Nanomaterials* **2020**, *10*, 1933.
97. Z. Hu, X. Xiao, C. Chen, T. Li, L. Huang, C. Zhang, J. Su, L. Miao, J. Jiang, Y. Zhang, J. Zhou, *Nano Energy* **2015**, *11*, 226.
98. H. Y. Lee, J. B. Goodenough, *J. Solid State Chem.* **1999**, *144*, 220.
99. S. C. Pang, M. A. Anderson, T. W. Chapman, *J. Electrochem. Soc.* **2000**, *147*, 444.
100. H. Shah, F. Wang, S. Muhammad, M. S. Javed, M. A. Ahmad, M. Saleem, J. Zhan, Z. H. Khan, L. Yan, *J. Energy Storage* **2018**, *17*, 318.
101. J. Miao, C. Zhou, X. Yan, H. Jiang, M. You, Y. Zhu, Y. Li, W. Zhou, X. Cheng, *Energy Fuels* **2021**, *35*, 2766.
102. K. W. Nam, K. H. Kim, E. S. Lee, W. S. Yoon, X. Q. Yang, K. B. Kim, *J. Power Sources* **2008**, *182*, 642.
103. Y. Ouyang, R. Huang, X. Xia, H. Ye, X. Jiao, L. Wang, W. Lei, Q. Hao, *Chem. Eng. J.* **2019**, *355*, 416.
104. M. M. Sk, C. Y. Yue, K. Ghosh, R. K. Jena, *J. Power Sources* **2016**, *308*, 121.
105. J. Zhao, Y. Tian, A. Liu, L. Song, Z. Zhao, *Mater. Sci. Semicond. Process.* **2019**, *96*, 78.
106. J. H. Lee, J. Y. Lim, C. S. Lee, J. T. Park, J. H. Kim, *Appl. Surf. Sci.* **2017**, *420*, 849.
107. M. C. Liu, L. B. Kong, C. Lu, X. M. Li, Y. C. Luo, L. Kang, *ACS Appl. Mater. Interfaces* **2012**, *4*, 4631.
108. X. Yang, C. Xiang, Y. Zou, J. Liang, H. Zhang, E. Yan, F. Xu, X. Hu, Q. Cheng, L. Sun, *J. Mater. Sci. Technol.* **2020**, *55*, 223.
109. Y. Ouyang, X. Xia, H. Ye, L. Wang, X. Jiao, W. Lei, Q. Hao, *ACS Appl. Mater. Interfaces* **2018**, *10*, 3549.
110. C. Sun, J. Yang, Z. Dai, X. Wang, Y. Zhang, L. Li, P. Chen, W. Huang, X. Dong, *Nano Res.* **2016**, *9*, 1300.
111. Y. Zhang, B. Lin, Y. Sun, P. Han, J. Wang, X. Ding, X. Zhang, H. Yang, *Electrochim. Acta* **2016**, *188*, 490.
112. S. Zhang, B. Yin, Z. Wang, F. Peter, *Chem. Eng. J.* **2016**, *306*, 193.
113. X. X. Meng, J. Y. Li, B. L. Yang, Z. X. Li, *Appl. Surf. Sci.* **2020**, *507*, 145077.
114. K. Panigrahi, P. Howli, K. K. Chattopadhyay, *Electrochim. Acta* **2020**, *337*, 135701.
115. S. Alagar, R. Madhuvilakku, R. Mariappan, S. Piraman, *J. Power Sources* **2019**, *441*, 227181.
116. Z. Peng, X. Liu, H. Meng, Z. Li, B. Li, Z. Liu, S. Liu, *ACS Appl. Mater. Interfaces* **2017**, *9*, 4577.
117. C. Wu, Y. Zhu, M. Ding, C. Jia, K. Zhang, *Electrochim. Acta* **2018**, *291*, 249.
118. A. K. Das, N. H. Kim, S. H. Lee, Y. Sohn, J. H. Lee, *Compos. B. Eng.* **2018**, *150*, 269.
119. Y. Shang, T. Xie, Y. Gai, L. Su, L. Gong, H. Lv, F. Dong, *Electrochim. Acta* **2017**, *253*, 281.
120. D. Ghosh, A. Pal, D. K. Singha, S. Ghosh, O. I. Lebedev, M. M. Seikh, P. Mahata, *ACS Appl. Nano Mater.* **2020**, *3*, 10105.
121. M. Y. Chung, C. T. Lo, *Electrochim. Acta* **2020**, *364*, 137324.
122. Lichchhavi, H. Lee, Y. Ohshita, A. K. Singh, P. M. Shirage, *Langmuir* **2021**, *37*, 1141.
123. C. W. Kuo, J. C. Chang, B. W. Wu, T. Y. Wu, *Int. J. Hydrog. Energy* **2020**, *45*, 22223.
124. J. Wu, Q. Li, C. E. Shuck, K. Maleski, H. N. Alshareef, J. Zhou, Y. Gogotsi, L. Huang, *Nano Res.* **2021**, 1.
125. A. Kumar, D. Sarkar, S. Mukherjee, S. Patil, D. D. Sarma, A. Shukla, *ACS Appl. Mater. Interfaces* **2018**, *10*, 42484.
126. C. C. Hu, T. W. Tsou, *J. Power Sources* **2003**, *115*, 179.
127. T. Xiong, W. S. V. Lee, X. Huang, J. M. Xue, *J. Mater. Chem. A* **2017**, *5*, 12762.
128. A. Zhang, R. Zhao, L. Hu, R. Yang, S. Yao, S. Wang, Z. Yang, Y. M. Yan, *Adv. Energy Mater.* **2021**, *11*, 2101412.
129. H. Heydari, M. Abdouss, S. Mazinani, A. M. Bazargan, F. Fatemi, *J. Energy Storage* **2021**, *40*, 102738.
130. Y. Wang, Z. Chen, T. Lei, Y. Ai, Z. Peng, X. Yan, H. Li, J. Zhang, Z. M. Wang, Y. L. Chueh, *Adv. Energy Mater.* **2018**, *8*, 1703453.
131. S. Dai, Y. Bai, W. Shen, S. Zhang, H. Hu, J. Fu, X. Wang, C. Hu, M. Liu, *J. Power Sources* **2021**, *482*, 228915.
132. C. Peng, J. Yu, S. Chen, L. Wang, *Chin. Chem. Lett.* **2019**, *30*, 1137.
133. M. S. Javed, Z. Jiang, C. Zhang, L. Chen, C. Hu, X. Gu, *Electrochim. Acta* **2016**, *219*, 742.
134. J. M. Jeong, B. G. Choi, S. C. Lee, K. G. Lee, S. J. Chang, Y. K. Han, Y. B. Lee, H. U. Lee, S. Kwon, G. Lee, C. S. Lee, Y. S. Huh, *Adv. Mater.* **2013**, *25*, 6250.

135. W. Tian, X. Wang, C. Zhi, T. Zhai, D. Liu, C. Zhang, D. Golberg, Y. Bando, *Nano Energy* **2013**, *2*, 754.
136. M. S. Javed, A. J. Khan, M. Hanif, M. T. Nazir, S. Hussain, M. Saleem, R. Raza, S. Yun, Z. Liu, *Int. J. Hydrog. Energy* **2021**, *46*, 9976.
137. H. Fan, R. Niu, J. Duan, W. Liu, W. Shen, *ACS Appl. Mater. Interfaces* **2016**, *8*, 19475.
138. R. P. Raj, P. Ragupathy, S. Mohan, *J. Mater. Chem. A* **2015**, *3*, 24338.
139. A. Rashti, X. Lu, A. Dobson, E. Hassani, F. Feyzbar-Khalkhali-Nejad, K. He, T.-S. Oh, *ACS Appl. Energy Mater.* **2021**, *4*, 1537.
140. L. Wang, Y. Jiao, S. Yao, P. Li, R. Wang, G. Chen, *Inorg. Chem. Front.* **2019**, *6*, 1553.
141. J. Xu, L. Wu, Y. Liu, J. Zhang, J. Liu, S. Shu, X. Kang, Q. Song, D. Liu, F. Huang, Y. Hu, *Surf. Interfaces* **2020**, *18*, 100420.
142. E. Samuel, B. Joshi, Y.-i. Kim, A. Aldalbahi, M. Rahaman, S. S. Yoon, *ACS Sustainable Chem. Eng.* **2020**, *8*, 3697.
143. W. D. Yang, Y. J. Lin, *Int. J. Electrochem. Sci.* **2020**, *15*, 1915.
144. G. Sun, H. Ren, Z. Shi, L. Zhang, Z. Wang, K. Zhan, Y. Yan, J. Yang, B. Zhao, *J. Colloid Interface Sci.* **2021**, *588*, 847.
145. X. Zhao, L. Mao, Q. Cheng, J. Li, F. Liao, G. Yang, L. Xie, C. Zhao, L. Chen, *Chem. Eng. J.* **2020**, *387*, 124081.
146. Y. Li, C. Song, J. Chen, X. Shang, J. Chen, Y. Li, M. Huang, F. Meng, *Carbon* **2020**, *162*, 124.
147. D. M. Mijailović, V. V. Radmilović, U. Č. Lačnjevac, D. B. Stojanović, V. D. Jović, V. R. Radmilović, P. S. Uskoković, *Appl. Surf. Sci.* **2020**, *534*, 147678.
148. M. Nagaraju, S. Chandra Sekhar, S. Junied Arbaz, J. Su Yu, *Appl. Surf. Sci.* **2021**, *563*, 150223.
149. Z. Bi, Q. Kong, Y. Cao, G. Sun, F. Su, X. Wei, X. Li, A. Ahmad, L. Xie, C. M. Chen, *J. Mater. Chem. A* **2019**, *7*, 16028.
150. W. Qiu, H. Xiao, M. Yu, Y. Li, X. Lu, *Chem. Eng. J.* **2018**, *352*, 996.
151. T. Zhai, L. Wan, S. Sun, Q. Chen, J. Sun, Q. Xia, H. Xia, *Adv. Mater.* **2017**, *29*, 1604167.
152. C. Yuan, L. Yang, L. Hou, J. Li, Y. Sun, X. Zhang, L. Shen, X. Lu, S. Xiong, X. W. Lou, *Adv. Funct. Mater.* **2012**, *22*, 2560.
153. C. Xiang, Y. Liu, Y. Yin, P. Huang, Y. Zou, M. Fehse, Z. She, F. Xu, D. Banerjee, D. H. Merino, A. Longo, H. B. Kraatz, D. F. Brougham, B. Wu, L. Sun, *ACS Appl. Energy Mater.* **2019**, *2*, 3389.
154. K. Qiu, M. Lu, Y. Luo, X. Du, *J. Mater. Chem. A* **2017**, *5*, 5820.
155. J. Wang, X. Zhang, Q. Wei, H. Lv, Y. Tian, Z. Tong, X. Liu, J. Hao, H. Qu, J. Zhao, Y. Li, L. Mai, *Nano Energy* **2016**, *19*, 222.
156. C. Yuan, L. Yang, L. Hou, L. Shen, X. Zhang, X. W. Lou, *Energy Environ. Sci.* **2012**, *5*, 7883.
157. C. Feng, J. Zhang, Y. He, C. Zhong, W. Hu, L. Liu, Y. Deng, *ACS Nano* **2015**, *9*, 1730.
158. S. Gao, Y. Sun, F. Lei, L. Liang, J. Liu, W. Bi, B. Pan, Y. Xie, *Angew. Chem., Int. Ed.* **2014**, *53*, 12789.
159. J. Zhao, B. Zhu, G. Yang, Y. Fu, Y. Lin, J. Li, *J. Phys. Chem. Solids* **2021**, *150*, 109856.
160. Z. Y. Li, M. Shaheer Akhtar, P. T. M. Bui, O. B. Yang, *Chem. Eng. J.* **2017**, *330*, 1240.
161. P. Liu, Y. Zhu, X. Gao, Y. Huang, Y. Wang, S. Qin, Y. Zhang, *Chem. Eng. J.* **2018**, *350*, 79.
162. W. Liu, M. Zhu, J. Liu, X. Li, J. Liu, *Chin. Chem. Lett.* **2019**, *30*, 750.
163. M. Kang, H. Zhou, P. Wen, N. Zhao, *ACS Appl. Energy Mater.* **2021**, *4*, 1619.
164. H. Zhou, M. Kang, B. Xie, P. Wen, N. Zhao, *J. Alloys Compd.* **2021**, *874*, 160030.
165. K. Xiang, D. Wu, Y. Fan, W. You, D. Zhang, J.-L. Luo, X.-Z. Fu, *Chem. Eng. J.* **2021**, *425*, 130583.
166. S. Sahoo, T. T. Nguyen, J.-J. Shim, *J. Ind. Eng. Chem.* **2018**, *63*, 181.
167. I. Hussain, D. Mohapatra, G. Dhakal, C. Lamiel, S. G. Mohamed, M. S. Sayed, Y. R. Lee, J. Lee, M. Lee, J.-J. Shim, *J. Energy Storage* **2020**, *32*, 101871.
168. A. Ali, I. Hameed, M. Ammar, R. Mujahid, S. Mirza, *J. Energy Storage* **2021**, *37*, 102472.
169. Z. Wang, W. Qian, Y. Ran, P. Hong, X. Xiao, Y. Wang, *J. Energy Storage* **2020**, *32*, 101865.
170. Y. Mao, J. Xie, C. Guo, H. Liu, H. Xiao, W. Hu, *Chem. Eng. J.* **2021**, *426*, 131188.
171. K. Chanda, S. Maiti, S. Sarkar, P. Bairi, S. Thakur, K. Sardar, N. Besra, N. S. Das, K. K. Chattopadhyay, *ACS Appl. Nano Mater.* **2021**, *4*, 1420.
172. G. Wang, Y. Yang, D. Han, Y. Li, *Nano Today* **2017**, *13*, 23.
173. Y. Wang, T. Zhou, K. Jiang, P. Da, Z. Peng, J. Tang, B. Kong, W. B. Cai, Z. Yang, G. Zheng, *Adv. Energy Mater.* **2014**, *4*, 1400696.
174. Y. Xu, M. Zhou, C. Zhang, C. Wang, L. Liang, Y. Fang, M. Wu, L. Cheng, Y. Lei, *Nano Energy* **2017**, *38*, 304.
175. L. Xu, Q. Jiang, Z. Xiao, X. Li, J. Huo, S. Wang, L. Dai, *Angew. Chem.* **2016**, *128*, 5363.
176. X. Zhang, G. Ma, L. Shui, G. Zhou, X. Wang, *ACS Appl. Mater. Interfaces* **2021**, *13*, 4419.
177. S. Dai, F. Han, J. Tang, W. Tang, *Electrochim. Acta* **2019**, *328*, 135103.
178. Q. Hu, C. Kang, S. Cao, C. Zhou, Q. Liu, *J. Alloys Compd.* **2021**, *883*, 160867.
179. X. Feng, J. Ning, D. Wang, J. Zhang, M. Xia, Y. Wang, Y. Hao, *J. Alloys Compd.* **2020**, *816*, 152625.
180. T. Anitha, A. E. Reddy, R. Vinodh, H.-J. Kim, Y.-R. Cho, *J. Energy Storage* **2020**, *30*, 101483.
181. J. Sun, L. Guo, X. Sun, J. Zhang, L. Hou, L. Li, S. Yang, C. Yuan, *Batter. Supercaps* **2019**, *2*, 820.
182. D. Susanti, D. S. Tsai, Y. S. Huang, A. Korotcov, W. H. Chung, *J. Phys. Chem. C* **2007**, *111*, 9530.
183. C. C. Hu, K. H. Chang, M. C. Lin, Y. T. Wu, *Nano Lett.* **2006**, *6*, 2690.
184. P. Yang, Y. Ding, Z. Lin, Z. Chen, Y. Li, P. Qiang, M. Ebrahimi, W. Mai, C. P. Wong, Z. L. Wang, *Nano Lett.* **2014**, *14*, 731.
185. S. Maiti, A. Pramanik, S. Mahanty, *ACS Appl. Mater. Interfaces* **2014**, *6*, 10754.
186. Z. Xu, S. Sun, W. Cui, J. Lv, Y. Geng, H. Li, J. Deng, *Electrochim. Acta* **2018**, *268*, 340.
187. S.-L. Chou, J.-Z. Wang, S.-Y. Chew, H.-K. Liu, S.-X. Dou, *Electrochem. Commun.* **2008**, *10*, 1724.
188. H. U. Shah, F. Wang, M. S. Javed, M. A. Ahmad, M. Saleem, J. Zhan, Z. U. H. Khan, Y. Li, *J. Energy Storage* **2018**, *17*, 318.
189. T. Yousefi, A. N. Golikand, M. Hossein Mashhadizadeh, M. Aghazadeh, *J. Solid State Chem.* **2012**, *190*, 202.
190. W. Xiao, H. Xia, J. Y. H. Fuh, L. Lu, *J. Power Sources* **2009**, *193*, 935.
191. J. Zhu, W. Shi, N. Xiao, X. Rui, H. Tan, X. Lu, H. H. Hng, J. Ma, Q. Yan, *ACS Appl. Mater. Interfaces* **2012**, *4*, 2769.

192. A. Ali, M. Ammar, I. Hameed, M. Ali, M. Tayyab, R. Mujahid, I. Ali, M. Zia-ul-Haq, M. Ashraf, *J. Electrochem. Soc.* **2020**, *167*, 100509.
193. X. Lu, Y. Zeng, M. Yu, T. Zhai, C. Liang, S. Xie, M. S. Balogun, Y. Tong, *Adv. Mater.* **2014**, *26*, 3148.
194. P. Yang, Y. Ding, Z. Lin, Z. Chen, Y. Li, P. Qiang, M. Ebrahimi, W. Mai, C. P. Wong, Z. L. Wang, *Nano Lett.* **2014**, *14*, 731.
195. R. B. Rakhi, W. Chen, D. Cha, H. N. Alshareef, *Nano Lett.* **2012**, *12*, 2559.
196. L. Kunhikrishnan, R. Shanmugham, *Mater. Charact.* **2021**, *177*, 111160.
197. J. Liang, L.-T. Bu, W.-G. Cao, T. Chen, Y.-C. Cao, *J. Taiwan Inst. Chem. Eng.* **2016**, *65*, 584.
198. W. Guo, X. Lian, Y. Tian, T. Yang, S. Wang, *J. Energy Storage* **2021**, *38*, 102586.
199. V. Kumar, V. Gajraj, K. I. Gnanasekar, S. Dsoke, S. Indris, H. Ehrenberg, B. Roling, C. R. Mariappan, *J. Alloys Compd.* **2021**, *882*, 160712.
200. X. Yin, H. Li, R. Yuan, Y. Jiao, J. Lu, *J. Materiomics* **2021**, *7*, 858.
201. A. Y. Faid, H. Ismail, *Mater. Today Energy* **2019**, *13*, 285.
202. S. Jeon, J. H. Jeong, H. Yoo, H. K. Yu, B.-H. Kim, M. H. Kim, *ACS Appl. Nano Mater.* **2020**, *3*, 3847.
203. M. Mahmood, A. Rasheed, I. Ayman, T. Rasheed, S. Munir, S. Ajmal, P. O. Agboola, M. F. Warsi, M. Shahid, *Energy Fuels* **2021**, *35*, 3469.
204. K. Allado, M. Liu, A. Jayapalan, D. Arvapalli, K. Nowlin, J. Wei, *Energy Fuels* **2021**, *35*, 8396.
205. D. Sarkar, S. Pal, S. Mandal, A. Shukla, D. D. Sarma, *J. Electrochem. Soc.* **2017**, *164*, A2707.
206. X. Lu, M. Yu, G. Wang, T. Zhai, S. Xie, Y. Ling, Y. Tong, Y. Li, *Adv. Mater.* **2013**, *25*, 267.
207. W. Zilong, Z. Zhu, J. Qiu, S. Yang, *J. Mater. Chem. C* **2014**, *2*, 1331.
208. A. K. Singh, D. Sarkar, *J. Mater. Chem. A* **2017**, *5*, 21715.
209. P. M. Shafi, R. Dhanabal, A. Chithambararaj, S. Velmathi, A. C. Bose, *ACS Sustainable Chem. Eng.* **2017**, *5*, 4757.
210. C. Young, J. Wang, J. Kim, Y. Sugahara, J. Henzie, Y. Yamauchi, *Chem. Mater.* **2018**, *30*, 3379.
211. A. Biswal, P. K. Panda, A. N. Acharya, S. Mohapatra, N. Swain, B. C. Tripathy, Z. T. Jiang, M. M. Sundaram, *ACS Omega* **2020**, *5*, 3405.
212. S. A. Beknalkar, A. M. Teli, N. S. Harale, D. S. Patil, S. A. Pawar, J. C. Shin, P. S. Patil, *Appl. Surf. Sci.* **2021**, *546*, 149102.
213. W. Lu, Y. Li, M. Yang, X. Jiang, Y. Zhang, Y. Xing, *ACS Appl. Energy Mater.* **2020**, *3*, 8190.
214. T. Mukhiya, G. P. Ojha, B. Dahal, T. Kim, K. Chhetri, M. Lee, S.-H. Chae, A. Muthurasu, A. P. Tiwari, H. Y. Kim, *ACS Appl. Energy Mater.* **2020**, *3*, 3435.
215. N. Nourani, K. Dashtian, M. Ghaedi, S. Shahbazi, S. Hajati, *Energy Fuels* **2021**, *35*, 11551.
216. P. Y. Tang, L. J. Han, A. Genç, Y. M. He, X. Zhang, L. Zhang, J. R. Galán-Mascarós, J. R. Morante, J. Arbiol, *Nano Energy* **2016**, *22*, 189.
217. L. Yuan, B. Yao, B. Hu, K. Huo, W. Chen, J. Zhou, *Energy Environ. Sci.* **2013**, *6*, 470.
218. X. F. Lu, X. Y. Chen, W. Zhou, Y. X. Tong, G. R. Li, *ACS Appl. Mater. Interfaces* **2015**, *7*, 14843.
219. Z. Yang, A. Qiu, J. Ma, M. Chen, *Compos. Sci. Technol.* **2018**, *156*, 231.
220. A. Sarkar, A. K. Singh, D. Sarkar, G. G. Khan, K. Mandal, *ACS Sustainable Chem. Eng.* **2015**, *3*, 2254.
221. F. Chen, Y. Chi, H. Zhang, F. Ma, F. Qin, *J. Alloys Compd.* **2021**, *888*, 161463.
222. S. Arunpandiyan, S. Vinoth, A. Pandikumar, A. Raja, A. Arivarasan, *J. Alloys Compd.* **2021**, *861*, 158456.
223. A. K. Singh, D. Sarkar, G. G. Khan, K. Mandal, *Appl. Phys. Lett.* **2014**, *104*, 133904.
224. D. Sarkar, S. Das, G. Sharada, B. Pal, H. Rensmo, A. Shukla, D. D. Sarma, *J. Electrochem. Soc.* **2017**, *164*, A987.
225. D. Sarkar, S. Mukherjee, S. Pal, D. Sarma, A. Shukla, *J. Electrochem. Soc.* **2018**, *165*, A2108.
226. A. K. Singh, D. Sarkar, K. Karmakar, K. Mandal, G. G. Khan, *ACS Appl. Mater. Interfaces* **2016**, *8*, 20786.
227. S. Jayasubramaniyan, S. Balasundari, S. J. Yeom, N. Naresh, T. Rani, E. V. Rapaka, N. Satyanarayana, H. W. Lee, P. Muralidharan, *Electrochim. Acta* **2021**, *390*, 138865.
228. K. Xu, S. Ma, Y. Shen, Q. Ren, J. Yang, X. Chen, J. Hu, *Chem. Eng. J.* **2019**, *369*, 363.
229. C. Zhang, C. Lei, C. Cen, S. Tang, M. Deng, Y. Li, Y. Du, *Electrochim. Acta* **2018**, *260*, 814.
230. S. Rajkumar, E. Elanthamilan, J. Princy Merlin, A. Sathiyan, *J. Alloys Compd.* **2021**, *874*, 159876.
231. P. Zhang, H. He, Q. Li, *Int. J. Hydrog. Energy* **2020**, *45*, 4784.
232. P. Siwatch, K. Sharma, S. K. Tripathi, *Electrochim. Acta* **2020**, *329*, 135084.
233. Y. Zhang, B. Lin, J. Wang, J. Tian, Y. Sun, X. Zhang, H. Yang, *J. Mater. Chem. A* **2016**, *4*, 10282.
234. H. Xia, C. Hong, B. Li, B. Zhao, Z. Lin, M. Zheng, S. V. Savilov, S. M. J. A. F. M. Aldoshin, **2015**, *25*, 627.
235. J. Yang, W. Liu, H. Niu, K. Cheng, K. Ye, K. Zhu, G. Wang, D. Cao, J. Yan, *Nano Res.* **2018**, *11*, 4744.
236. S. Liu, J. Zhou, Z. Cai, G. Fang, Y. Cai, A. Pan, S. Liang, *J. Mater. Chem. A* **2016**, *4*, 17838.
237. Y. Lian, Z. Xu, D. Wang, Y. Bai, C. Ban, J. Zhao, H. Zhang, *J. Alloys Compd.* **2021**, *850*, 156808.

AUTHOR BIOGRAPHIES

Mr. Ankit Kumar received his B. Sc. (H) chemistry degree from University of Delhi, India, in the year 2014. Currently, he is pursuing his Ph.D degree at Indian Institute of Science, Bengaluru, India, under the supervision of Prof. Satish Patil and Prof. Ashok Shukla. His work is mainly focused on electrochemical capacitors based on metal oxide, metal chalcogenides, and carbon electrodes. He is interested in earth abundant materials which can be used for the purpose of electrochemical energy storage. He is also interested in electric mobility.

Ms. Hem Kanwar Rathore received her master's degree in Physics from Central University of Rajasthan, India, in the year 2019. She is currently pursuing her Ph.D degree under the supervision of Dr. Debasish Sarkar in the Department of Physics at Malaviya National Institute of Technology Jaipur, India. Her current research centers on the synthesis and characterization of nanomaterials for energy harvesting and storage applications, with emphasis on the exploration of novel nanostructured electrode materials for high- voltage hybrid ion supercapacitors. She is also interested in photo-rechargeable energy storage systems.

Dr. Debasish Sarkar received his Ph.D degree from S N Bose National Centre for Basic Sciences, India, in the year 2014. He carried out his post-doctoral research work as INSPIRE Faculty Fellow at Indian Institute of Science, India, and as Research Associate at Clarkson University, New York, USA. Currently, he is serving as an Assistant Professor in the Department of Physics at Malaviya National Institute of Technology Jaipur, India. His research activities are focused on the development of novel nanostructured electrode materials for electrochemical energy (H_2) generation through water splitting and energy storage through metal-ion batteries and supercapacitors. He has filed three patents and published more than thirty-five research articles in peer-reviewed journals of international repute.

Prof. Ashok Shukla is presently an Emeritus Professor at Indian Institute of Science, Bengaluru, India. He has made extensive fundamental and applied contributions to the fields of storage batteries, fuel cells and supercapacitors. He is a fellow of *Indian National Science Academy*, *Indian National Academy of Engineering*, *National Academy of Sciences India*, *Indian Academy of Sciences*, *The Electrochemical Society* (US) and *The International Society of Electrochemistry*.

How to cite this article: A. Kumar, H. K. Rathore, D. Sarkar, A. Shukla, Nanoarchitectured transition metal oxides and their composites for supercapacitors. *Electrochem Sci Adv*. **2022**, *2,* e2100187. https://doi.org/10.1002/elsa.202100187